Research & Development

2011

Mechanical Engineering Letters, Szent István University

TRANS–TRIO SCIENCES
Gent • Gödöllő • Baia Mare

Preface

The first officially announced GGB Trans-Trio-Sciences Workshop held in Szent István University, Gödöllő, was organized as a parallel session of „*Synergy and Technical Development*" international conferences in agricultural engineering, 2009, Gödöllő. The selected and reviewed scientific content of the workshop was published in the "Mechanical Engineering Letters".

<div align="center">

„GGB Trans-Trio Sciences"
Gent – **G**ödöllő – **B**aia Mare

</div>

The further scientific co-operation of the partners in the field of tribology related engineering and design led to second workshop also escorting the „*Synergy and Technical Development*" international conference, 2011.

This release of "Mechanical Engineering Letters" vol.5. contains reviewed articles selected from the second GGB Trans-Trio-Sciences Workshop concerning tribology from the points of materials, construction, computational and experimental modelling, friction and wear process control, maintenance of worn parts.

Prof. Gábor KALÁCSKA	Prof. Patrick DE BAETS	Prof. Radu COTETIU
Szent István University, Gödöllő Hungary	University Gent Belgium	North University, Baia Mare Romania

Contens

Friction torque, temperature and roughness in roll-slip phenomenon for polymer –steel contacts

[1]Jacob SUKUMARAN, [2]Mátyás ANDÓ, [1]Vanessa RODRIGUEZ,
[1]Patrick DE BAETS, [3]Patric Daniel NEIS

[1]Department of Mechanical Construction and Production, Laboratory Soete, Ghent University
[2]Institute for Mechanical Engineering Technology,
Faculty of Mechanical Engineering, Szent István University
[3]Universidade Federal do Rio Grande do Sul, – UFRGS, Rua Sarmento Leite, Brazil

Abstract

The current study gives an insight of the roll-slip phenomenon of polymer-metal pair where priority is given to measurement techniques, test duration and the behavior of the polymer. A systematic tribological measurement was used to identify the friction torque from polymer –metal pairs where the friction torque from contact is obtained by subtracting the base torque of the test rig to exploit the absolute results. Base torque of the machine is almost constant, the changing can describe with linear trend line which is less than 0,5% per ten minutes. Measurements made for 3 hours shows that the friction force between the polyamide 6 (NaPA6) and structural steel (S33J2) has a polynomial of degree two with a function ($F_f = -1.5549 \cdot T^2 + 9.4031 \cdot T + 13{,}126$). Micrographs from the contact surface revealed the damage of roughness peaks during the course of testing. The involved wear mechanisms was investigated with roughness measurements and microscopy. The roughness plots also correlates with the micrograph where the rate of decrease in Ra in the initial stage is higher followed by a linear increase in the later stage. This can describe using polynomial function of degree as ($Ra = 0.029 \cdot T^2 + 0.3695 \cdot T + 2.4967$).

Keywords

Roll/slip, compensation friction torque, roughness.

1. Introduction

In polymer tribology the commonly investigated phenomenon is sliding, and a significant amount of research has also been conducted for rolling [1-5]. However a limited research was done for the phenomenon with a rolling to sliding ratio [6-8]. Roll-slip phenomenon still needs a lot more investigation from the measurements perspective for polymer metal pairs. Roll-slip is the

commonly occurring mechanisms in the engineering components like gears cams rollers etc. This phenomenon exhibits in small scale applications like gears in fax machines to the large scale levels like bearings for roller mills and in agricultural engineering applications. Earlier researches on rolling resistance have been interpreted from the view point of traction where both the specimen and the countermaterial deform [5]. Nevertheless, in those models both the specimen and the countermaterial deforms. But in the case of polymer metal pair the mating material is rigid to undergo a deformation. Thus the mechanisms involved in the contact surface are vital to dictate the friction behaviour.

Inaccuracies behind every scientific research might have the appropriate reasoning from experiments perspective. Careful consideration of the whole system can avoid the errors. A developed connection between the mechanism and the system can serve as a starting point for updating and corrections. These inaccuracies can be attributed to specific sector tribology: where 92 % mean deviation confirms to the corrections of the result. Most of the researches perfomed calculates the combine friction force/friction torque of the system and the contact [6-8]. In polymers metal contacts where the friction is relatively low this combined value might affect the precission of the measurement. Thus friction torque from the machine itself is an important factor on maintaining the accuracy and the repeatability of the experiments. Attempts have been made by researchers to by using a elastic contacts for identifying the friction force in rolling /sliding contacts [5] where the validation might be more realistic on subtracting the friction of the stem from the contact. Reserch using PA 46 on twin-disc with the slip ratio of 2% has been performed earlier where the rate of change of coefficient of friction during the test period was 0.25 to 0.35 [6]. Images and roughness acquired from time to time could also serve as an vital evidenceon identifyin the involved wear mechanisms. Xiao et al in his study on roll-slip phenomenon of steel on steel pairs has found high friction coefficient increases with increasing roughness [9], nevertheless, more data are required for the polymer metal roll-slip . Polymer which has greater importance due to its embedding ability and the visco elastic behaviour can be correlated with the change in surface topography. The changes in roughness during in the course of wear like damage of peaks and valleys also dictate the course of wear. Besides the roughness of the countermaterial influences the tribological properties and the correlation between the roughness of the polymer and the friction is mostly governed by the modulus of elasticity of the polymer.

2. Materials and methods

In order to investigate the roll-slip and its relation to the friction force a twin-disc setup was used. The slip ratio used in the testing is defined as the rolling to sliding ration and given in equation (1) where d_1 is the diameter of the steel disc and d_2 is the diameter of the polymer disc.

$$s = \frac{d_2 - d_1}{d_1} \qquad (1)$$

Test Materials

The examined materials were from Quattroplast Kft. (Hungary). The used thermoplastic polymer was Sodium catalyzed cast polyamide 6 – NaPA6 and commercially available structural steel (S355J2) was used as the counter material. The material properties of the test materials are tabulated below in Table 1.

Properties	S355J2	NaPA6
Yield strength [MPa]	355	80
Elongation at break [%]	16 - 18	>40
Young's modulus [GPa]	510 - 680	3.3
Hardness	160 HB	83 Shore D
Moisture absorption at 23˚C and 50 ReH [%]	–	2.5
Thermal conductivity (20˚C) [W/(m·K)]	60	0.23
Maximum allowable service temp. [˚C]	–	110

Test setup

The equipment used for testing roll-slip is the modified FZG (Forschungsstelle fur Zahnrader und Getriebebau) setup. This equipment was used to model a rolling to sliding contact with a specific slip ratio. Since both the saft carrying counter material and test specimen rotate at the same rpm, the required slip ratio is obtained by the difference in diameter of the specimen.
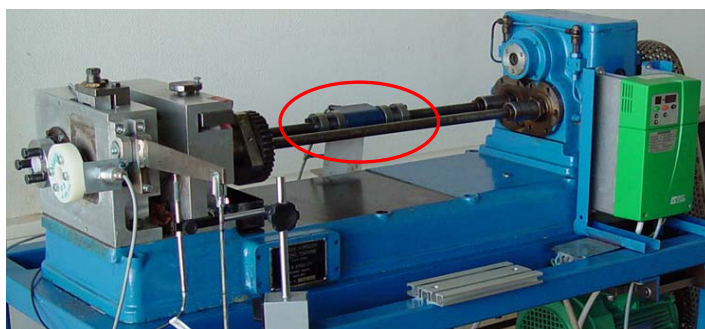

Figure 1. Modified FZG where the twin-disc tests were conducted.

A torque meter (Lorenz Messtechnik DR-20-type) is used to record the exhibited torque. Fig. 1. shows the used twin-disc setup with the circle mark on the torque meter which was connected to the shaft of the counter material disc.

The temperature of the contact surface is measured on the polymer material using an contactless infra-red sensor. The temperature sensor is placed 50 mm perpendicularly away from the contact surface. The load is given through the pivoted arm engaged to the movable shaft where the polymer disc is fixed. All the measurements are recorded online using a data acquisition system. The roughness was measured at regular intervals using a cut-off value of 0.8 and a traverse distance of 4 mm was used.

Test Parameters

Roll-slip testing tends to have complex measurements where the results have to be corrected to find the absolute value. The test parameters were carefully chosen to investigate the three different purposes. Initially the torque from the machine (base torque) is identified by running the machine at no load condition without contact for 30 minutes at a speed of 250rpm. The initial measurement was done in order to validate the base. Furthermore, a test with duration of 3 hours is conducted to identify the rate of change in friction force as a function of time. The second test was conducted at a speed of 200 rpm with a normal force of 130N. Before and after the test the base torque of the machine was measured on no load condition for a period of 15 minutes. The dimensions of both the polymer and steel disc are Ø89.9 and Ø 74.95 respectively; the dimensional specifications of the discs are selected to match the slip ratio of 20% which is considered to be close to the practical application.

The final test is to identify the change in microstructure of the specimen. The test was repeated with stop-over for measuring the influence of roughness of the specimen at an interval of 15 minutes for 225 minutes. After every 15 minutes the test was stopped and the image of the specimen was acquired using an optical microscope connected to a 10 bit CCD, simultaneously the roughness at that instant was also measured using a Hommel tester.

3. Results

In scientific investigation it is important to know the consistency of the measured parameters from the equipment. Precise measurements adds value to the whole research especially in place of tribological measurements it could lead to energy saving and indirectly help on material selection. In normal flat on flat testing the friction measurements are directly obtained from the load cell however in testing roll-slip the measurements made from the torque sensor serves as a reference to calculate the co-efficient of the friction. In such places the torque sensor measures the combined friction torque from the contact and the machine. Thus the components of the test rig also aids to the inaccuracies (e.g. seals and bearing resistance).

Base torque

The first measurement aims to identify the resistance of the test-rig. Fig. 2. show the plot for the base torque as a function of time.
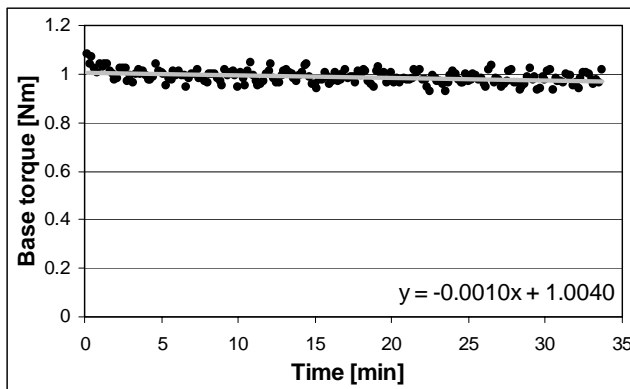
Figure 2. 30 minutes base torque measurement.

As clearly seen on the Fig 2. the base torque is almost constant along the time. At the first 5 minutes there is a decrease in base torque which probably belongs to lubrication effect. After 5 minutes the oil fill all the places (bearings) and follows without any change and hence the curve is linear. The base torque relatively having small rate of change where the variation every 10 minutes is less than 1%. But on using the second part of the measurement (15-30 minutes) the variation is 0,5% per 10 minutes. Base on this phenomenon in further investigation it will be appropriate to measure the base torque before and after the test, and correcting the nominal torque with a linear base torque function.

3 hours friction measurement
For a specific condition (20 % slip, 200 rpm, 130 N normal force) the friction force between sodium catalyzed PA6 and S355J2 structural steel was measured. The plot with the friction force as a function of rolling-sliding time is shown in Fig. 3.
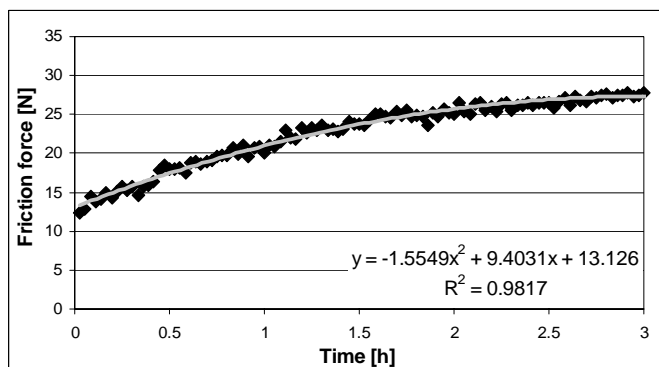
Figure 3. The friction force as a function of time
with the fitted curve.

The tendency of the friction force can described with a polynomial function of degree 2. The equation for the calculated curve is given in (2), which is valid from 0-180 minutes.

$$F_f = -1.5549 \cdot T^2 + 9.4031 \cdot T + 13{,}126 \text{ , } R^2 = 0.9817 \tag{2}$$

This tendency refers that the half of the changes occurs in the first 30% time of testing. Moreover, to study the effects of temperature a curve was plotted with temperature as a function of rolling-sliding time (Fig. 4.).
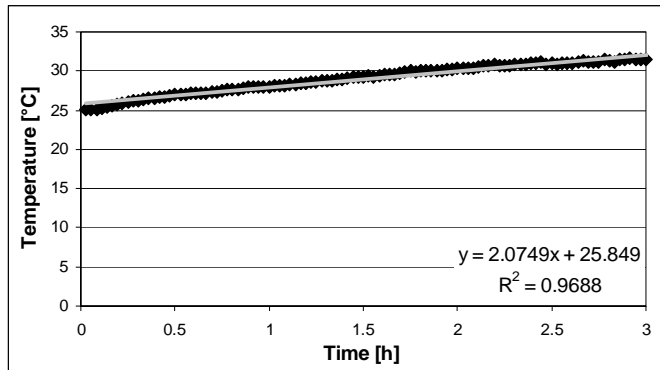
Figure 4. The temperature as a function of time with the fitted curve.

It is clearly seen on the fig. 4 that the change in temperature almost linear. The equation for the calculated curve is (3), which valid from 0-180 minutes.

$$t = 2.0749 \cdot T + 25.849 \text{ , } R^2 = 0.9688 \tag{3}$$

The change in temperature after 3 hours testing is less than 7°C. This value is relatively low, which does not change significantly the mechanical and tribologyical properties.

Microstructure changing
All the images were acquired using a 20X objective which has a calculated total magnification of 335 times, the field of view is about 1,4×1 mm polymer surface (Fig. 5.). The measured roughnesses are also shown in the micrograph where it is evident that the roughness decreases as a function of time. Considering the image as a function of time the damage of the peaks from the machining is very much visible leading to the change in the roughness value. Moreover, the peaks after considerable running time have been worn down to the level of the valley and are connected by the valley. The difference of 1µm was observed for the initial and the final value of the Ra (Fig. 6.).
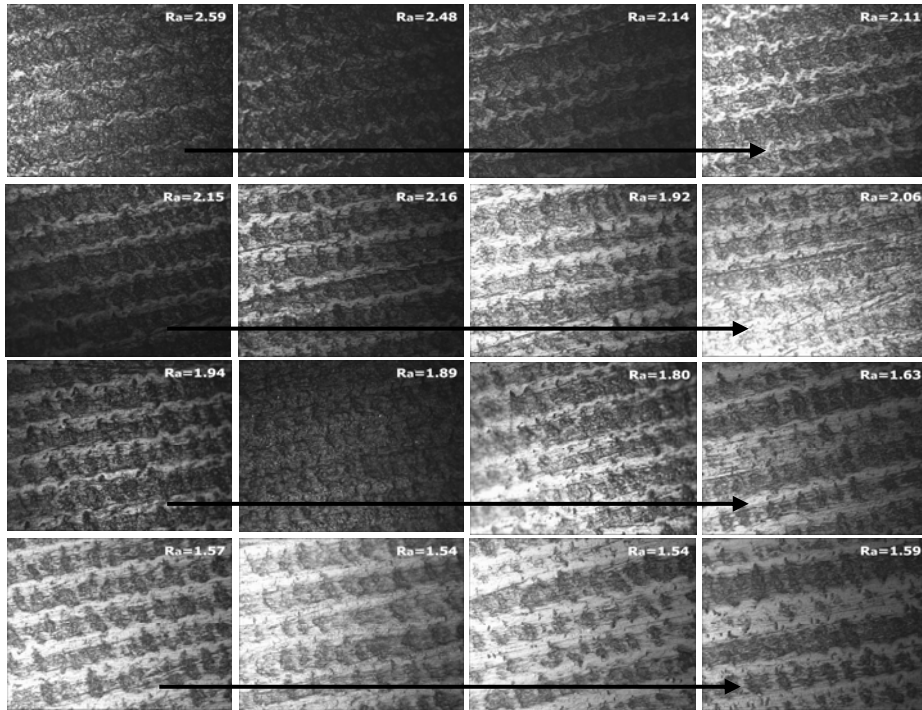
Figure 5. The micrograph of the worn surface and the corresponding roughness values taken at regular intervals.

Abrasion of soft polymer by the structural steel is seen from the lines running over the contact surface. The change in Ra for the speculated test period is 38 % and considered to be significant in case of tribological testing.

$$y = 0.029x^2 - 0.3695x + 2.4967$$
$$R^2 = 0.922$$
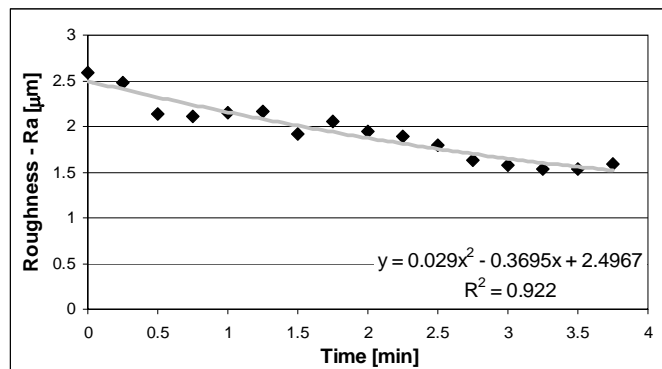
Figure 6. Roughness changing at every 15 minutes.

The trend for the change in roughness is illustrated by polynomial function similar to the friction force. The equation for the calculated curve is (4), which valid from 0-225 minutes.

$$Ra = 0.029 \cdot T^2 + 0.3695 \cdot T + 2.4967 \; , \; R^2 = 0.9220 \tag{4}$$

4. Discussion

Standards for measuring system can provide a systematic approach to acquire error free data. Acceptable range for the errors in the obtained results depend upon the sector, however considering tribology field limitations exists. Measuring friction torque using standard procedures for roll-slip phenomenon aids precise results. Isolation of complex phenomenon provides a chance to analyze the influence of individual parameters. Considering the base torque in fig 2 it can be seen from the plot it is almost constant which is due to the lubrication effect from the bearing are moreover the oil temperature is constant. The obtained base torque from the machine is removed as compensation from friction torque due to the contact. The 3 hours test shows a trend with polynomial of degree 2 where the friction force which can be attributed theoretically to the change in surface and temperature. From the temperature plot it is evident that the change is less than 7˚C where the curve as seen from the plot has a linear increase. This might be due to the cooling effect between every contact where the contact surface is exposed to the ambience temperature (25˚). Moreover, there is enough time to conduct the heat via the metal counterpart and the shafts. Based on the temperature measurement the change in surface has a vital effect of the friction force but not to the temperature.

The rate of change of roughness is high which is seen from the micrograph. It is evident from the curves that the change in roughness is also polynomial, because the at the initial stage the roughness peeks are worn much faster. This influence can be attributed from the topographical change of the surface: Initially the surface changes fast, because the real contact area is much smaller at this stage where the contact is mostly from the tip of the roughness peaks. For which the contact pressure is relatively high for the individual peaks. After a specific period of testing the peaks are damaged and the real contact surface increases. The bigger area leads smaller contact pressure but help to the adhesion phenomenon. This effect has a vital influence to change the friction force.

5. Conclusions

Structured roll-slip tribological measurement was identified where careful consideration was taken for the compensation of the friction torque from the machine itself. It was also found the base torque is almost constant along the testing which aids to obtain the real values from the measurement. Following the

systematic approach, the long term measurement (3 hours) shows that, the friction force between the NaPA6/S33J2 can be described using a polynomial function with degree 2. Micrograph was used as evidence to compare the change in roughness. It was clearly seen that, the peeks are destroyed at the beginning of testing. In the initial stage the rate of change in roughness is much higher and further it becomes linear. The polynomial function in both the cases for roughness and the friction force illustrates the relationship between each other, although the relations are reverse. By using the results high precision online tribological measurements can be recorded. Further attempts to acquire the images online can aid to reveal the actual mechanisms involved in the course of testing.

6. Acknowledgements

References

1. P. Samyna, P. De Baets a, G. Schoukens b, I. Van Driessche, Friction, wear and transfer of pure and internally lubricated cast polyamides at various testing scales, Wear 262 (2007) 1433–1449,

2. H. Unal a, U. Sen, A. Mimaroglu, Dry sliding wear characteristics of some industrial polymers

against steel counterface, Tribology International 37 (2004) 727–732

3. S. Apichartpattanasiri, J.N. Hay, S. N. Kukureka, A study of the tribological behaviour of polyamide 66 with

varying injection-moulding parameters, Wear 251 (2001) 1557–1566

4. P. Samyn, P. De Baets a, G. Schoukens, A. P. Van Peteghem, Large-scale tests on friction and wear of engineering polymers for material selection in highly loaded sliding systems, Materials and Design 27 (2006) 535–555

5. G Komandi, An evaluation of the concept of rolling resistance, Journal of terramechanics 36(1999) 159-166

6. D.H. Gordona,b, S. N. Kukurekaa,The wear and friction of polyamide 46 and polyamide 46/aramid-fibre composites in sliding–rolling contact, Wear 267 (2009) 669–678

7. Kukureka SN, Chen YK, Hooke CJ, Liao P. The wear mechanisms of acetal in unlubricated rolling - sliding contact. Wear 1995;185:1-8.

8. Chen YK, Modi OP, Mhay AS, Chrysanthou A, Sullivan JMO. The effect of different metallic counterface materials and different surface treatments on the wear and friction of polyamide 66 and its composite in rolling–sliding contact. Wear 2003;255:714-721.

9. L Xiaoa, S Bj R Lund, BG. Rose, The influence of surface roughness and the contact pressure distribution on friction in rolling/sliding contacts, Tribology International 40 (2007) 694–698

10. V Quaglini, Paolo Dubini, Daniela Ferroni, Carlo Poggi Influence of counterface roughness on friction properties of engineering plastics for bearing applications, Materials and Design 30 (2009) 1650–1658

An implicit return mapping algorithm for anisotropic plasticity with mixed non-linear kinematic-isotropic-hardening

Mohsen SAFAEI, Wim DE WAELE

Department of Mechanical Construction and Production,
Laboratory Soete, Ghent University

Abstract

Advanced material models can be used to simulate most of the characteristics of sheet metal subjected to plastic deformation. Commercial Finite Element (FE) codes are limited in terms of available advanced material models. Therefore the authors developed and implemented into FE an advanced anisotropic material model using UMAT in which the implicit radial return mapping was used. The model can be used for any yield criterion combined with mixed non-linear kinematic hardening and isotropic hardening (NLK-IH) originating from the Armstrong-Frederick hardening model and later developed by Chaboche. This paper discusses in detail the integration algorithm used for the implemented UMAT. This material model will improve the modelling capabilities for sheet metal forming processes, such as the prediction of earing in cup drawing and springback in U bend operations.

Keywords

sheet metal forming, finite element, mixed hardening, anisotropic material, implicit return mapping

1. Introduction

In recent years several comprehensive constitutive models have been developed (Barlat and Lian 1989; Banabic, Aretz et al. 2005; Bouvier, Gardey et al. 2006) and implemented in dedicated software. In the commercial finite element code ABAQUS (Hibbitt, Karlsson and Sorensen Inc) the user is limited to the Hill 48 model for anisotropic yielding. More advanced models have to be implemented by means of the user material (UMAT) subroutine. Unfortunately, the codes of such subroutines for advanced constitutive models are typically not available as open source.

Implementing material constitutive equations into finite element code can simply be explained as defining stress update algorithms in which an imposed strain increment gives rise to a corresponding stress increment. Describing this incremental relation is not always straightforward. Fully implicit, explicit and semi-implicit integration schemes can be used for introducing the material

constitutive behaviour into FE. As opposed to explicit integration, implicit integration used with consistent Jacobian overcomes the convergence problems encountered at the transition from elastic to plastic behaviour. As a result, overestimation of stress at first yield will not appear. Moreover, contrary to explicit integration which uses small time steps, implicit integration enables the use of larger time steps so CPU time can be highly reduced. Note that a finite element method is referred to as an implicit method when implicit schemes are employed for the integration of the momentum balance or equilibrium equations. Therefore an implicit finite element method can use implicit or explicit integration for constitutive equations such as stress update algorithms (Dunne and Petrinic 2005).

This paper discusses implicit radial return mapping used for introducing a material model for plane stress which is based on a quadratic yield function (Hill) and mixed non-linear kinematic hardening and isotropic hardening (NLK-IH) originating from the Armstrong-Frederick hardening model and later developed by Chaboche. This material model will improve the modelling capabilities for sheet metal forming processes, such as the prediction of earing in cup drawing and springback in U bend operations

2. Constitutive plasticity model

Yield criteria and the NKH-IH hardening model

Based on the additive decomposition of the strain tensor increment $d\underset{\sim}{\varepsilon}$ into an elastic and a plastic part and using Hooke's law, the relation between stress and elastic strains can be written as:

$$d\underset{\sim}{\sigma} = \underset{\approx}{C^e} : \left(d\underset{\sim}{\varepsilon} - d\underset{\sim}{\varepsilon^p} \right) \tag{1}$$

$$\underset{\approx}{C^e} = \frac{E}{1-v^2} \begin{bmatrix} 1 & v & 0 \\ v & 1 & 0 \\ 0 & 0 & \frac{1-v}{2} \end{bmatrix} \tag{2}$$

where $\underset{\approx}{C^e}$ is the elastic tangent moduli tensor. As used in ABAQUS, the Voigt notation is used in this paper.

$$\underset{\sim}{\sigma} = \begin{bmatrix} \sigma_1 \\ \sigma_2 \\ \sigma_{12} \end{bmatrix}, \ \underset{\sim}{\varepsilon} = \begin{bmatrix} \varepsilon_1 \\ \varepsilon_2 \\ \gamma \end{bmatrix}, \ \gamma := 2\varepsilon_{12} \tag{3}$$

An implicit return mapping algorithm for anisotropic plasticity with mixed
non-linear kinematic-isotropic- hardening

TRANS–TRIO SCIENCES

Where σ, ε and γ are Cauchy (plane) stress, strain and engineering shear strain which is twice the tensorial shear strain, respectively.

Yield criteria are defined by

$$F = f(\overline{\underset{\sim}{\sigma}} - \sigma^{iso}(\overline{\varepsilon}^{p})) \tag{4}$$

f_y is the continuously differentiable yield function, $\overline{\underset{\sim}{\sigma}} = \underset{\sim}{\sigma} - \underset{\sim}{\alpha}$ with $\underset{\sim}{\alpha}$ the back stress tensor, σ^{iso} is the isotropic hardening function and $\overline{\varepsilon}^{p}$ is effective plastic strain. In associated plasticity, the effective plastic strain is equal to the plastic multiplier λ:

$$d\overline{\varepsilon}^{p} = d\lambda \tag{5}$$

In the presented integration algorithm, f can be any yield function but in this paper only Hill's 48 quadric yield criterion is discussed:

$$f = (\tfrac{1}{2}\overline{\underset{\sim}{\sigma}} : \underset{\approx}{P} : \overline{\underset{\sim}{\sigma}})^{\tfrac{1}{2}} \tag{6}$$

The P tensor can be calculated based on the Lankford coefficients R_x with x the orientation of a tensile specimen with respect to the rolling direction:

$$\underset{\approx}{P} = \begin{bmatrix} 1 & -\beta_{12} & 0 \\ -\beta_{12} & \beta_{22} & 0 \\ 0 & 0 & \beta_{66} \end{bmatrix} \tag{7}$$

$$\beta_{12} = \frac{R_0}{1+R_0}; \beta_{22} = \frac{R_0(1+R_{90})}{R_{90}(1+R_{0)}}; \beta_{66} = \frac{(R_0+R_{90})(1+2R_{45})}{R_{90}(1+R_0)}$$

The isotropic hardening function (σ^{iso}) determines a uniform change in all directions of the yield surface's size , and the back stress function ($\underset{\sim}{\alpha}$) translates the yield surface in stress. The former and the latter are functions of accumulated plastic strain and plastic strain, respectively. Whereas the isotropic hardening is reasonably effective to simulate monotonous and proportional operations during which load direction does not change (Chung, Lee et al. 2005), this function overestimates hardening and springback for non-monotonous deformations. At the other hand, the kinematic hardening function, when used alone, underestimates both hardening and springback (Zhao and Lee 2002). Therefore a combination of isotropic and kinematic hardening is required to predict the phenomena observed in the evolution of the yield stress surface due to change of

load direction. These phenomena are Bauschinger effect, softening, transient (Fig. 1.) and stagnation behavior.
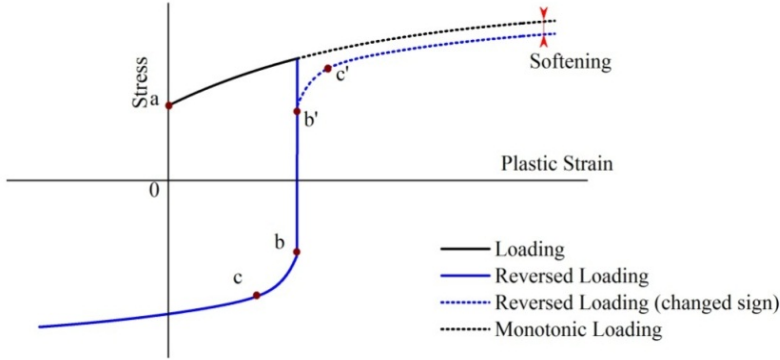
Figure 1. Phenomena observed in the hardening curve due
to reversed loading cycles

When material hardens due to slip deformation, strain incompatibilities occur between grains resulting in micro-residual stresses in the material. These micro-residual stresses cause the renown Bauschinger effect which is macroscopically characterized by reduced yielding of material upon load reversal. This effect decreases during cyclic loading. The linear kinematic hardening law with one material parameter proposed by Prager takes the Bauschinger effect into account (Prager 1956). The Prager's model is written as:

$$d\,\underset{\sim}{\alpha} \approx d\,\underset{\sim}{\varepsilon}^{p} \tag{8}$$

Here, the yield surface translates in the same direction as the plastic strain increment. Due to linearity, difficulties occur when this model is used for cyclic loading which involves reversing the load direction (Chaboche 1986). In addition, as described by Ziegler, the Prager's model does not produce consistent results for 2D and 3D cases (Ziegler 1959). To overcome this inconsistency, Ziegler proposed another linear kinematic hardening law in which the yield's surface translates radially from its center (Ziegler 1959). The Ziegler's model assumes the following evolution:

$$d\,\underset{\sim}{\alpha} \approx \underset{\sim}{\sigma} - \underset{\sim}{\alpha} \tag{9}$$

Neither Prager nor Ziegler models can address the hardening nonlinearities which play an important role in the behaviour of materials such as aluminium or advanced high strength steels.

20

An implicit return mapping algorithm for anisotropic plasticity with mixed
non-linear kinematic-isotropic- hardening

TRANS–TRIO SCIENCES
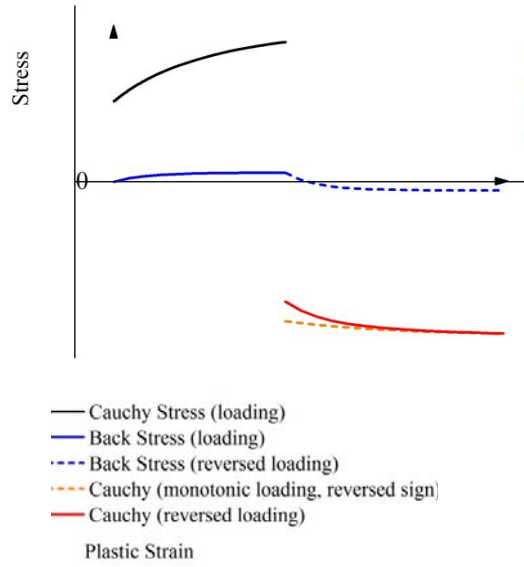
Figure 2. Nonlinear isotropic-kinematic hardening

From these hardening nonlinearities, the transient behaviour introduces a smooth transition from elastic to plastic in the hardening curve which is shown by the segments $b - c$ and $b' - c'$ in fig. 1.. The transient behaviour was considered in hardening models proposed by (Armstrong and Frederick 1966; Chaboche and Rousselier 1983; Chaboche 1986; Chaboche 1991; Armstrong and Frederick 2007). The non-linear kinematic hardening law of Armstrong & Frederick considers the evanescent strain memory effect observed in cyclic loadings by adding a relaxation term (recall term) to the Ziegler's linear kinematic hardening model, both of which evolve independently.

$$d\underset{\sim}{\alpha} = c\frac{\overline{\sigma}}{f}d\overline{\varepsilon}^{p} - \gamma\underset{\sim}{a}\,d\overline{\varepsilon}^{p} \qquad (10)$$

Where c and γ are hardening parameters and as described before for convenience $\overline{\underset{\sim}{\sigma}} = \underset{\sim}{\sigma} - \underset{\sim}{\alpha}$. Integrating this model for uniaxial conditions gives:

$$\alpha = {c}/{\gamma}\left(1 - e^{-\gamma\overline{\varepsilon}^{p}}\right) \qquad (11)$$

where ${c}/{\gamma}$ and γ denote to saturated value of back stress and rate of saturation, respectively.
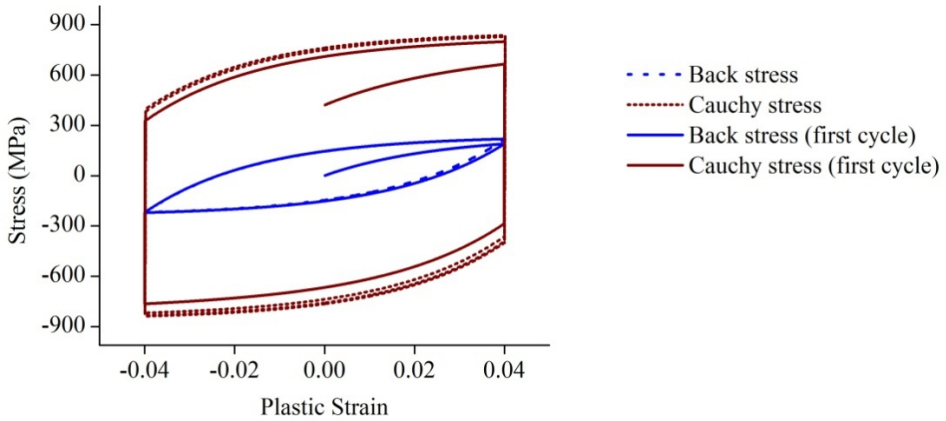
Figure 3. Stress-strain curve for dual phase steel DP600 and Chaboche model

Later Chaboche (Chaboche 1986) proposed superposing multiple Armstrong & Frederick laws as one model. As suggested by Chaboche, using multiple back stresses may result in a considerable improvement of results in some cases (Hibbitt, Karlsson and Sorensen Inc).

$$\underset{\sim}{\alpha} = \sum_{i=1}^{N} \underset{\sim}{\alpha_i} \tag{12}$$

where N is number of back stress components.

The Voce isotropic hardening model is written as:

$$\sigma^{iso}\left(\overline{\varepsilon}^{p}\right) = \sigma_0 + R \tag{13}$$

and

$$\dot{R} = b(Q - R)\dot{\overline{\varepsilon}}^{p} \tag{14}$$

where Q and R are material parameters.

After a certain number of cycles Voce isotropic stabilizes to Q with saturation rate of b (Chaboche 1986). When Voce isotropic hardening is used in conjunction with Chaboche kinematic hardening saturating hardening curves are produced for cyclic loadings, Fig. 3. For materials with non-saturating hardening (such as Aluminum) the Voce model can be replaced by other hardening laws such as Swift's law. In the Voce model, the yield surface expansion rate decreases monotonically which properly produces a convex curve for stable materials such as (advanced) high strength steels (Chun, Jinn et al. 2002).

However, this approach may result in erroneous results for some materials with upper and lower yield or relatively flat stress strain curve

Loading/un-loading and consistency conditions
The Kuhn-Tucker unilateral constraints (also called complementarity conditions) provide the most convenient formulation of the loading/unloading conditions for classical plasticity. Stresses must be admissible and plastic strain can only take place on the yield surface. Therefore λ and σ are restricted by the following unilateral constraints (Belytschko, Liu et al. 2000):

$$\lambda \geq 0, \; f(\sigma, \rho) \leq 0$$
$$\lambda f(\sigma, \rho) = 0 \tag{15}$$

In addition $\lambda \geq 0$ must satisfy the consistency requirement. This hypothesis describes that when the material hardens, the load point remains on the yield surface, and can be mathematically expressed as:

$$\lambda f \cdot (\sigma, p) = 0 \tag{16}$$

or alternatively

$$\underset{\sim}{n} : d\overline{\underset{\sim}{\sigma}} = H(\overline{\varepsilon}^p) d\overline{\varepsilon}^p$$
$$\underset{\sim}{n} = \frac{\partial f_y(\overline{\underset{\sim}{\sigma}})}{\partial \overline{\underset{\sim}{\sigma}}} \tag{17}$$

and

$$H(\overline{\varepsilon}^p) = \frac{\partial \sigma^{iso}(\overline{\varepsilon}^p)}{\partial \overline{\varepsilon}^p} = bQ_e^{-b\overline{\varepsilon}^p} \tag{18}$$

Reminding $\overline{\underset{\sim}{\sigma}} = d\underset{\sim}{\sigma} - d\underset{\sim}{\alpha}$ and substituting $d\underset{\sim}{\sigma}$ from Eqn.(1) and $d\underset{\sim}{\alpha}$ from Eqn. (10) into Eqn. (17) results after some manipulations in:

$$d\lambda = \frac{\underset{\sim}{n} : \underset{\approx}{C}^e : d\underset{\sim}{\varepsilon}}{H + \underset{\sim}{n} : \underset{\approx}{C}^e : \underset{\sim}{n} + \underset{\sim}{n} : \underset{\sim}{A}_{kin}}$$
$$A_{kin} = c\frac{\overline{\underset{\sim}{\sigma}}}{f_p} - \gamma \underset{\sim}{\alpha} \tag{19}$$

The elasto-plastic tangent modulus is after some manipulation obtained by using the incremental plastic multiplier from Eqn.(5)

$$\frac{d\,\sigma}{d\,\varepsilon} = C^{ep} = C^{e} - \frac{\left(n : C^{e}\right) \otimes \left(n : C^{e}\right)}{H + n : C^{e} : n + n : A_{kin}} \tag{20}$$

Stress update algorithm

The stress update algorithm starts with assuming that the increment of strain is completely elastic. The resulting stress is called trial stress, which goes beyond the yield surface in case of plastic deformation.

$$\sigma^{trial} = {}^{i}\sigma + \Delta\varepsilon : C^{e} \tag{21}$$

The back-superscript i refers to the previously converged calculation step, while the current step is i+1. Variables without the back-superscript mean in the current step, unless stated otherwise.

$$\overline{\sigma}^{trial} = \sigma^{trial} - {}^{i}\alpha \tag{22}$$

Occurrence of plastic deformation is evaluated by checking the following formula

$$F = f(\overline{\sigma}^{trial}) - \sigma^{iso}({}^{i}\overline{\varepsilon}^{p}) < \delta \tag{23}$$

in which δ is a very small number such as 10E-15. When Eqn (22) is fulfilled, it means that the material is in the elastic region, otherwise it is yielding.

The associated plastic flow is described by:

$$d\,\varepsilon^{p} = d\lambda\,n \text{ and } d\,\overline{\varepsilon}^{p} = d\lambda \tag{24}$$

Using this sub-stepping algorithm introduced by Yoon (1999), a new series of equations is made for k-th sub-potential residual.

$$\sigma = {}^{i}\sigma + C^{e} : \Delta\varepsilon^{el} = {}^{i}\sigma + C^{e} : (\Delta\varepsilon - \Delta\varepsilon^{p}_{k}) \tag{25}$$

where $\Delta\varepsilon^{el}$ and $\Delta\varepsilon^{p}$ are increments in elastic and plastic strain.

$$\alpha_{\sim} = {}^{i}\alpha_{\sim} + \left(c \frac{\overline{\sigma}_{\sim}}{f_p} : \Delta \overline{\varepsilon}_k^p - \gamma \, \alpha_{\sim} \, \Delta \overline{\varepsilon}_k^p \right) \tag{26}$$

The $\sigma_{\sim}$ and $\alpha_{\sim}$ should comply with the following yield condition

$$F_k = f(\overline{\sigma}_{\sim}) - \sigma^{iso}({}^{i}\overline{\varepsilon}^p + \Delta \lambda_k) \tag{27}$$

The $\sigma_{\sim}$, $\alpha_{\sim}$, $\overline{\sigma}_{\sim}$ and $\overline{\varepsilon}^p$ in Eqns. (25)-(27) are dependent on $\Delta \lambda_k$ which needs to be determined by the Newton-Raphson iteration method. For simplicity the k index is omitted.

Using the sub-step iterative algorithm, the radial return of stress on the yield surface is not happening in one step but is divided in m steps. For the k-th step the solution is obtained by solving a series of non-linear equations using Newton-Raphson iteration. In this method r-residuals are defined to present the difference between current constitutive variables and backward Euler ones. Applying r-residuals for Eqns (25)-(27)

$$r^{\sigma}_{\sim} = \sigma_{\sim} - {}^{i}\sigma_{\sim} - C^e_{\approx} : (\Delta \varepsilon_{\sim} - \Delta \lambda_k \, n_{\sim}) \tag{28}$$

$$r^{\alpha}_{\sim} = \alpha_{\sim} - {}^{i}\alpha_{\sim} - c \frac{\overline{\sigma}_{\sim}}{f} \Delta \overline{\varepsilon}_k^p + \gamma \, \alpha_{\sim} \, \Delta \overline{\varepsilon}_k^p \tag{29}$$

$$r^{F} = f(\overline{\sigma}_{\sim}) - \sigma^{iso}({}^{i}\overline{\varepsilon}^p + \Delta \lambda_k) - F_k \tag{30}$$

Using a truncated Taylor expansion for Eqns (28)-(30)

$$r^{\sigma(Taylor)}_{\sim} = r^{\sigma}_{\sim} + \dot{\sigma}_{\sim} + \dot{\lambda}_k \, C^e_{\approx} : n + \Delta \lambda_k \, C^e_{\approx} : \dot{n}_{\sim} = 0 \tag{31}$$

and

$$\dot{n}_{\sim} = (\dot{\sigma}_{\sim} - \dot{\alpha}_{\sim}) : \frac{\partial n_{\sim}}{\partial \sigma_{\sim}}$$

$$r^{\alpha(Taylor)}_{\sim} = r^{\alpha}_{\sim} + \dot{\alpha}_{\sim} - c \frac{\overline{\sigma}_{\sim}}{f} \Delta \dot{\overline{\varepsilon}}^p_{k} \, c_1 \frac{\left(\dot{\sigma}_{\sim} - \dot{\alpha}_{\sim}\right)}{f} \Delta \overline{\varepsilon}^p_{k} + \tag{32}$$

$$+ \frac{\overline{\sigma}_{\sim} \dot{f}}{f^2} \Delta \overline{\varepsilon}^p_{k} + \gamma \, \alpha_{\sim} \, \Delta \dot{\overline{\varepsilon}}^p_{k} + \gamma \, \dot{\alpha}_{\sim} \, \Delta \overline{\varepsilon}^p_{k}$$

$$r^{F(Taylor)} = r^F + f_y - H\Delta \dot{\overline{\varepsilon}}^{p}_{k} \tag{33}$$

After laborious calculations, incremental change in the back stress is found as

$$\dot{\underset{\sim}{\alpha}} = \underset{\sim 1}{o}(\dot{\lambda}) + \dot{\underset{\sim}{\sigma}} o_2 \tag{34}$$

where

$$\underset{\sim 1}{o}\left(\dot{\lambda}\right) = -\frac{r^{\alpha 1} + \dfrac{g_1\left(\dot{\lambda}\right)}{g_2} \underset{\sim 1}{l}}{1 + \gamma\Delta\overline{\varepsilon}^{p} - l_2}, \quad o_2 = -\frac{l_2}{1 + \gamma\Delta\overline{\varepsilon}^{p} - l_2}$$

$$\underset{\sim 1}{l} = \left(\gamma \underset{\sim 1}{\alpha} - c_1 \frac{\overline{\underset{\sim}{\sigma}}}{f_p}\right), \quad l_2 = g_3 \underset{\sim}{n} : \underset{\sim 1}{l} \tag{35}$$

$$g_1\left(\dot{\lambda}\right) = \dot{\lambda} + \Delta\overline{\varepsilon}^{p} \frac{r^F}{f_y}, \quad g_2 = 1 + \Delta\overline{\varepsilon}^{p} \frac{1}{f_y} H, \quad g_3 = \frac{\Delta\lambda}{f\,g_2}$$

Incremental change in the Cauchy stress is

$$\dot{\underset{\sim}{\sigma}} = -\underset{\approx}{\Theta}^{-1} : r^{\sigma} - \underset{\approx}{\Theta}^{-1} \dot{\lambda} \underset{\approx}{C}^e : n + \underset{\approx}{\Theta}^{-1} \underset{\approx 1}{A} : \underset{\sim 1}{o}(\dot{\lambda}) \tag{36}$$

Where

$$\underset{\approx 1}{A} = \Delta\lambda \underset{\approx}{C}^e : \frac{\partial \underset{\sim}{\overline{n}}}{\partial \underset{\sim}{\sigma}}$$

$$\underset{\approx}{\Theta} = \underset{\approx}{I} + \Delta\lambda \underset{\approx}{C}^e : \frac{\partial \underset{\sim}{\overline{n}}}{\partial \underset{\sim}{\sigma}}(1 - o_2)$$

Implementation of plasticity constitutive equations into ABAQUS using implicit integration, demands the definition of the tangent stiffness matrix or material Jacobian ($\partial\Delta\sigma / \partial\Delta\varepsilon$) which highly depends on material behaviour. It should be noted that the material Jacobian does not affect the accuracy of the

An implicit return mapping algorithm for anisotropic plasticity with mixed
non-linear kinematic-isotropic- hardening

TRANS–TRIO SCIENCES

solution but the rate of the convergence of the solution. In case of isotropic elasticity the material Jacobian is the same as the elastic tangent stiffness ($\underset{\approx}{C^e}$).

$$\dot{\lambda} = \frac{r^F + \underset{\sim 1}{d} : \underset{\approx 2}{B} : \underset{\sim 1}{B} - (1 - o_2)\underset{\approx}{\Theta^{-1}} : r^\sigma : \underset{\sim 1}{B}}{H + (1 - o_2)\underset{\approx}{\Theta^{-1}} \underset{\approx}{C^e} : \underset{\sim}{n} : \underset{\sim 1}{B} + \underset{\approx 2}{B} : \underset{\sim 1}{B} : \underset{\sim 2}{d}} \tag{37}$$

$$\underset{\sim 1}{d} = \frac{-r^{\alpha 1}}{B_3} - \frac{\underset{\sim 1}{l}}{g_2 B_3}\Delta\varepsilon^{-p}\frac{r^F}{f}, \quad \underset{\sim 2}{d} = \frac{\underset{\sim 1}{l}}{g_2 B_3}$$

$$\underset{\sim 1}{B} = \underset{\sim}{n} - H(2\Delta\gamma\frac{1}{f}\underset{\sim}{n}), \quad \underset{\approx 2}{B} = (1 - o_2)\underset{\approx}{\Theta^{-1}}\underset{\approx 1}{A} - \underset{\approx}{I}, \tag{38}$$

$$B_3 = 1 + \gamma\Delta\bar{\varepsilon}^p - l_2$$

When $\dot{\lambda}$ is found from (37), then $\dot{\sigma}$, $\dot{\alpha}$ are found from, (34) and (36). Stress and strain can finally be updated according to the following equations:

$$^{i+1}\underset{\sim}{\sigma} = {}^i\underset{\sim}{\sigma} + \dot{\underset{\sim}{\sigma}} \tag{39}$$

$$^{i+1}\underset{\sim}{\alpha} = {}^i\underset{\sim}{\alpha} + \dot{\underset{\sim}{\alpha}} \tag{40}$$

$$^{i+1}\Delta\lambda = {}^i\Delta\lambda + \dot{\lambda} \tag{41}$$

$$^{i+1}\Delta\bar{\varepsilon}^p = {}^{i+1}\Delta\lambda \tag{42}$$

Where superscripts i and i+1 denote to iterative steps.

Conclusions

This paper presents the elastic-plastic integration of material constitutive laws for the case of plane stress and mixed non-linear kinematic hardening and isotropic hardening and any arbitrary yield criterion. The key parameter in this is the plastic multiplier λ for which Newton's iteration method has been used. Effective plastic strain and plastic strain are stored at the end of the subroutine and are recalled at the next iteration. Finally, material Jacobian is returned to the program even though that it has no effect on the accuracy of the solution but the rate that it converges.

Acknowledgements

References

1. Armstrong, P. J. and C. O. Frederick (1966). "A Mathematical representation of the multiaxial Bauschinger effect." Central Electricity Generating Board Report, Berkeley Nuclear Laboratories, RD/B/N 731.

2. Armstrong, P. J. and C. O. Frederick (2007). "A mathematical representation of the multiaxial Bauschinger effect." Materials at high temperatures 24(1): 11-26.

3. Banabic, D., H. Aretz, et al. (2005). "An improved analytical description of orthotropy in metallic sheets." International Journal of Plasticity 21(3): 493-512.

4. Barlat, F. and K. Lian (1989). "Plastic behavior and stretchability of sheet metals. Part I: A yield function for orthotropic sheets under plane stress conditions." International Journal of Plasticity 5(1): 51-66.

5. Belytschko, T., W. K. Liu, et al. (2000). Nonlinear finite elements for continua and structures. Chichester, John Wiley.

6. Bouvier, S., B. Gardey, et al. (2006). "Characterization of the strain-induced plastic anisotropy of rolled sheets by using sequences of simple shear and uniaxial tensile tests." Journal of Materials Processing Technology 174(1-3): 115-126.

7. Chaboche, J. L. (1986). "Time-Independent Constitutive Theories for Cyclic Plasticity." International Journal of Plasticity 2(2): 149-188.

8. Chaboche, J. L. (1991). "On some modifications of kinematic hardening to improve the description of ratchetting effects." International Journal of Plasticity 7(7): 661-678.

9. Chaboche, J. L. and G. Rousselier (1983). "On the Plastic and Viscoplastic Constitutive Equations---Part I: Rules Developed With Internal Variable Concept." Journal of Pressure Vessel Technology 105(2): 153-158.

10. Chun, B. K., J. T. Jinn, et al. (2002). "Modeling the Bauschinger effect for sheet metals, part I: theory." International Journal of Plasticity 18(5-6): 571-595.

11. Chung, K., M.-G. Lee, et al. (2005). "Spring-back evaluation of automotive sheets based on isotropic-kinematic hardening laws and non-quadratic

An implicit return mapping algorithm for anisotropic plasticity with mixed
non-linear kinematic-isotropic- hardening

TRANS–TRIO SCIENCES

anisotropic yield functions: Part I: theory and formulation." International Journal of Plasticity 21(5): 861-882.

12. Dunne, F. and N. Petrinic (2005). Introduction to computational plasticity. Oxford ; New York, Oxford University Press.

13. Hibbitt, Karlsson and Sorensen Inc ABAQUS User's Manuals Version 6.10, Pawtucket, Rhode Island, USA.

14. Prager, W. (1956). "A new method of analysing stresses and strains in work hardening plastic solids." Transactions of ASME, Journal of Applied Mechanics 23: 493–496.

15. Simo, J. C. and T. J. R. Hughes (1998). Computational inelasticity. New York, Springer.

16. Yoon, J. W., D. Y. Yang, et al. (1999). "Elasto-plastic finite element method based on incremental deformation theory and continuum based shell elements for planar anisotropic sheet materials." Computer Methods in Applied Mechanics and Engineering 174(1-2): 23-56.

17. Zhao, K. M. and J. K. Lee (2002). "Finite element analysis of the three-point bending of sheet metals." Journal of Materials Processing Technology 122(1): 6-11.

18. Ziegler, H. (1959). " A modification of Prager's hardening rule." Quarterly of Applied Mechanics 17: 55-65.

Review of current knee biomechanical modeling techniques

[1,2]Gusztáv FEKETE, [2]Béla CSIZMADIA, [1]Patrick DE BAETS,
[1]Magd ABDEL WAHAB

[1]Department of Mechanical Construction and Production,
Laboratory Soete, Ghent University

[2]Department of Mechanics and Technical Drawing, Institute for Mechanics and Machinery
Szent István University

Abstract

In this paper we are going to present an essential modification of an existing analytical model. The model creation normally starts with a simplified, less complex analytical model, where the phenomena can be easily interpreted, checked and controlled. If this model is available and valid – with its certain simplifications – then as a following step, it can be either extended by taking into account earlier neglected factors or a similar but more advanced computational model has to be created in order to broaden the investigated factors.

   The accent will be set on a neglected factor, the moving center of gravity (COG), in this paper, and the obtained results will be compared with some external data from other authors.

Keywords

biomechanics, human knee, analytical model

1. Introduction

The applied tools in the biomechanical modeling begin with the use of mechanical-analytical models and involve MR techniques, computer-aided-design, multibody- or finite element simulations.

   In order to investigate complex motions with such programs and methods, a well-based, reliable analytical model has to be created with adequate number of constrains and reasonable simplifications. To show the impact of the neglected factors in the models, a well-known motion, the deep-squat will be presented, examined and explained throughout the paper. Let us look at the analytical modeling part of the investigation.

2. Analytical model

In the relevant literature, the kinetics of deep-squat is investigated by mechanical models and test rigs. The most spread among the test rigs is the so-called Oxford

type while so far the most typical approximation of the deep-squat is the mechanical model shown in Figure 1 (Cohen et al., 2001). In the figure, the flexion angle is denoted as α, L is the theoretical length of the femur and the body weight vector is denoted as G.
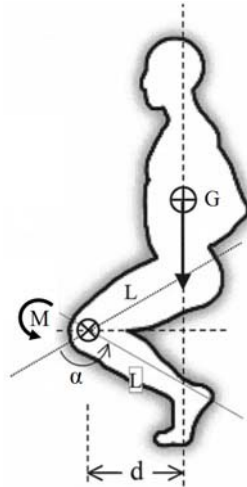

Figure 1. Deep-squat movement by Cohen et al.

The following simplifications were considered related to Cohen model:
– The model is quasi-static,
– Two-dimensional,
– The inertial forces during the movement are neglected,
– No internal forces (F_s, F_N) between the surfaces are considered,
– Only the squatting movement is investigated with the model,
– The load is derived from the mass of the person,
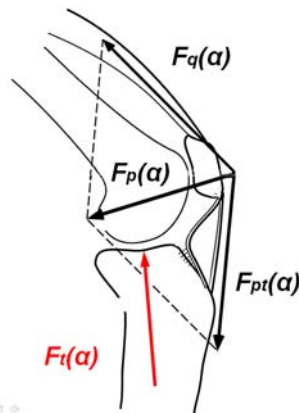– The body weight vector (G) can only move vertically.

Figure 2. Free body diagram of the patellofemoral forces

There are three major forces which have significant effects in the knee joint, namely the quadriceps force (F_q), the patellofemoral joint reaction force (F_{pf}) and the patellar ligament force (F_p) (see in Figure 2). Besides these forces there is one more important force the tibio-femoral force (F_{tf}), but this force cannot be calculated with most of the analytical models.

Let us follow Cohen's approach in the derivation of the formulas according to Mason's description (Mason et al., 2008), thus let us note that L represents the length of the femur and the length itself is considered here as 0.45 m. The moment arm is represented as d, while the body weight vector as G:

$$d(\alpha) = L \cdot \sin(\alpha/2) \tag{1}$$

The so-called net-knee moment can be derived as follows:

$$M_k(\alpha) = 0.5 \cdot G \cdot d(\alpha) = 0.5 \cdot G \cdot L \cdot \sin(\alpha/2) \tag{2}$$

The quadriceps force (F_q) can be derived from the net knee moment (M_k) and the effective moment arm (see in Table 1) of the quadriceps (Salem and Powers, 2001):

$$F_q(\alpha) = \frac{M_k(\alpha)}{L_{eff}(\alpha)} \tag{3}$$

The patellofemoral joint reaction force (F_{pf}) can be expressed as a product of the quadriceps force and the $k(\alpha)$ dimensionless function (Van Eijden et al., 1986) which is found in Table 1:

$$F_{pf}(\alpha) = F_q(\alpha) \cdot k(\alpha) = \frac{M_k(\alpha)}{L_{eff}(\alpha)} \cdot k(\alpha) \tag{4}$$

Finally, the patellar ligament force (F_p) can be derived by substituting Eq. (5) in Eq. (1), where $g(\alpha)$ dimensionless function (Van Eijden et al., 1986) which is found in Table 1.

$$F_p(\alpha) = F_q(\alpha) \cdot g(\alpha) = \frac{M_k(\alpha)}{L_{eff}(\alpha)} \cdot g(\alpha) \tag{5}$$

Thus the model is based on the assumption, that during the squat the center of gravity (shortly COG) – the body weight – does not change its line of action, thus the net knee moment can be derived as a simple function of the flexion

angle. This approach assumes that the subject stays in perfectly vertical position during squatting which gives two false results. First, if a person tries to carry out a deep-squat movement, the balancing is completely necessary, which means that the COG has to change its place. Second, by neglecting the change of the COG calls forth unnecessary overestimation. The excursion of the COG has been described as a linear function of the flexion angle (Fekete et al., 2011), thus by inserting this function into the L length, the moment arm of the net-knee moment is reduced and the moving COG phenomena is taken into account. Let us consider the dimensionless λ_3 function (Table 1) which describes the change of COG (Fekete et al., 2011):

$$\lambda_3(\alpha) = -0.0022 \cdot \alpha + 0.86 \tag{6}$$

Then, let us create a new function for the L length:

$$L(\alpha) = L \cdot \lambda_3(\alpha) = -0.00099 + 0.387 \tag{7}$$

Table 1. Functions and constants of the
mathematical model

	C0	C1	C2	C3	C4	SD	r^2	Sample	p-value
g(α) [-]	1.102	-2.209D-3	-1.493D-4	1.138D-6	0	0.1	0.989	13	p < 0.05
k(α) [-]	0.486	1.324D-2	-1.151D-4	+3.35D-7	0	0.11	0.989	13	p < 0.05
L_{eff}(α) [mm]	0.046	2.8D-4	-1.3D-5	8D-8	0	N/A	0.98	N/A	N/A
λ_3(α) [-]	0.86	-2.2D-3	0	0	0	0.2	0.63	31	p < 0.05

3. Results

With this altered length the net-knee moment is highly lowered as it follows:

Naturally, all the other forces become lower than in the case of the original calculation method. In order to prove the validity of moving COG implementation, experimental data or other author's results are plotted along the results.
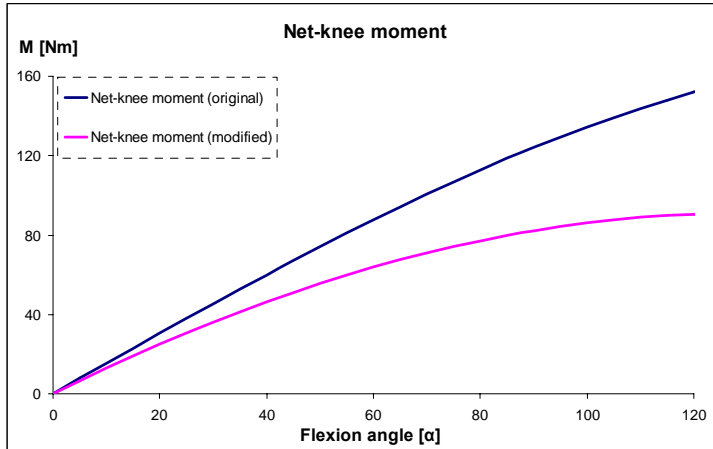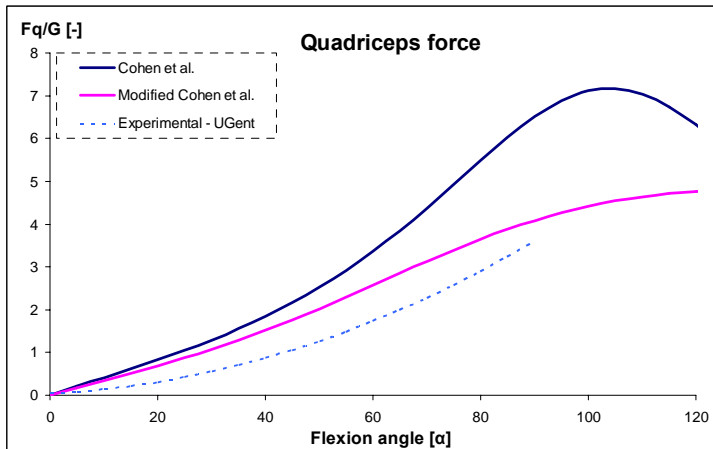
Net-knee moment

Figure 3. Net-knee moment functions

Quadriceps force

Figure 4. Quadriceps force function
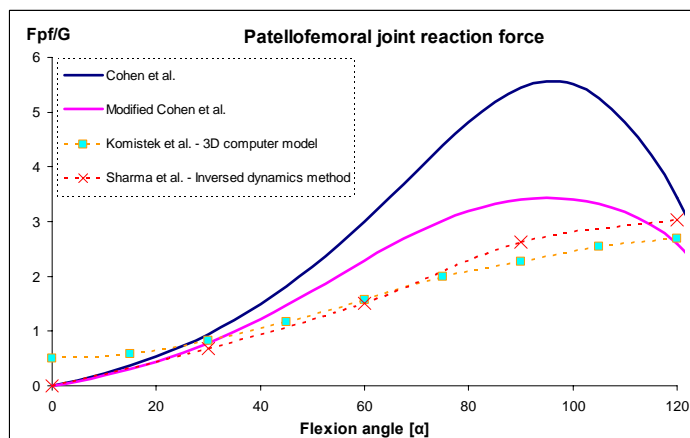
Patellofemoral joint reaction force

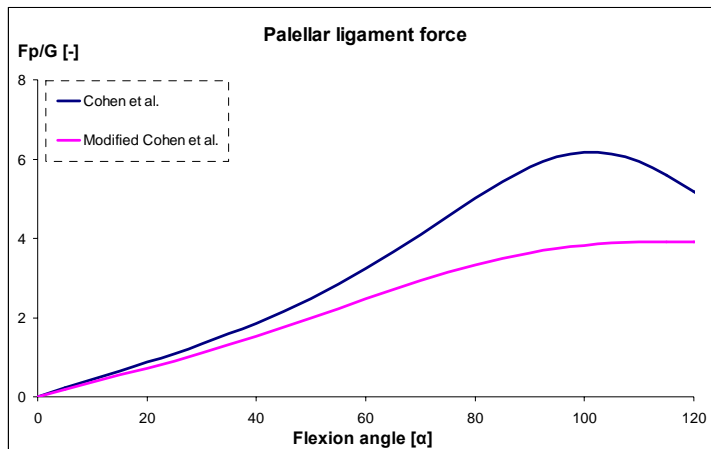*Figure 5.* Patellofemoral joint reaction force

Figure 6. Patellar ligament force

The results obviously show that the modified model – with the moving COG – gives a better approximation (with less overestimation) contrarily the original method.

5. Conclusion

In summary, a novel modification of an existing model was presented. The moving COG has significant impact on the forces, and this was demonstrated in this paper. This analytical model was derived from theoretical assumptions and experimentally determined parameters – based on multiple human participants. The obtained, modified $F_q(\alpha)$ force function can be extended for further use as an input function for isometric motion, since all the descriptive relationships found in the literature provide a ratio of the patellofemoral forces divided by the quadriceps force.

Acknowledgement

References

1. Cohen, Z.A., Roglic, H., Grelsamer, R.P., Henry, J.H., Levine, W.N., Mow, V.C., Ateshian, G.A. (2001): Patellofemoral stresses during open and closed kinetic chain exercises – An analysis using computer simulation. The American Journal of Sports Medicine, 29, 480-487.

2. Fekete, G., Csizmadia, B., Wahab, M.A., De Baets, P. (2011): Experimental determination of horizontal motion of human center of gravity during squatting.Experimental Techniques, (Accepted, Publication status "Early view").

3. Frohm, A., Halvorsen, K., Thorstensson, A., 2007. Patellar tendon load in different types of eccentric squats. Clinical Biomechanics, 22, 704-711.

4. Komistek, R.D., Kane, T.R., Mahfouz, M., Ochoa, J.A., Dennis, D.A., 2005. Knee mechanics: a review of past and present techniques to determine in vivo loads. Journal of Biomechanics, 38, 215-228.

5. Mason, J.J., Leszko, F., Johnson, T., Komistek, R.D. (2008): Patellofemoral joint forces. Journal of Biomechanics, 41, 2337-2348.

6. Salem, G.J., Powers, C.M., 2001. Patellofemoral joint kinetics during squatting in collegiate women athletes. Clinical Biomechanics, 16, 424-430.

7. Sharma, A., Leszko, F., Komistek, R.D., Scuderi, G.R., Cates, H.E., Liu, F., 2008. In vivo patellofemoral forces in high flexion total knee arthroplasty. Journal of Biomechanics, 41, 642-648.

8. Van Eijden, T.M.G.J., Kouwenhoven, E., Verburg, J., Weijs, W.A., 1986. A mathematical model of the patellofemoral joint. Journal of Biomechanics, 19, 219-229.

9. Zheng, N., Fleisig, G.S., Escamilla, R.F., Barrentine, S.W., 1998. An analytical model of the knee for estimation of internal forces during exercise. Journal of Biomechanics, 31, 963-967.

Influence of wire-EDM on high temperature sliding friction response of WC-10wt%Co cemented carbide

[1]Yeczain PÉREZ DELGADO, [1]Koen BONNY, [1]Patrick DE BAETS,
[1]Vanessa RODRIGUEZ FEREIRA, [2,3]Olivier MALEK, [2]Jef VLEUGELS,
[3]Bert LAUWERS, [4,1]Patric Daniel NEIS

[1]Department of Mechanical Construction and Production,
Laboratory Soete, Ghent University

[2] Metallurgy and Materials Engineering Department, Catholic University of Leuven

[3] Mechanical Engineering Department, Catholic University of Leuven

[4] Department of Mechanical Engineering, Universidade Federal do Rio Grande do Sul

Abstract

Continuous sliding experiments on WC-10wt%Co have been conducted at temperatures of 25 and 400 °C in dry conditions according to the ASTMG99-95a standard. WC-6wt%Co pins were used as counter body. The plate specimens were surface finished by grinding and wire-EDM. The tests were performed using a rotating sliding speed of 0.3 m/s and mean Hertzian contact pressure of 2.06 GPa. Pins and plate specimens were analyzed by 2-D and 3-D surface topography scanning and optical microscopy. The experimental results demonstrated that wear and friction of WC-Co cemented carbides is influenced significantly by elevated temperature as well as surface finishing condition.

Keywords

WC-10wt%.Co, wire-EDM, Friction and wear, High temperature, pin-on-plate

1. Introduction

Cemented carbides, best known for their high hardness and superior wear resistance, have a range of industrial uses more diverse than that of any other powder metallurgy product. These materials are commonly used for cutting tools, drilling applications, mining equipment, etc (Glaeser, 1998). However, there is a high need in the industry to improve the profit and production by reducing maintenance cost, lubricants, etc. Cemented carbides are basically produced by powder metallurgy which involves milling, mixing, green densification and finally liquid phase sintering. Cobalt is the alloying metal and constitutes only a small part (ranging from 3 up to 20%) of the total mass. It is the most preferred binder in WC-based hardmetals due to its outstanding wetting and adhesion characteristics in combination with tungsten carbide, leading to unique properties (Zhengui et al, 1998).

Normally, cemented carbides are machined and surface finished by means of grinding and subsequently polished with boron nitride and/or diamond which make the final shaping very hard. In the last years, an innovative technology called wire-EDM has overcome those difficulties. Nevertheless, this machining process is a thermal process and depending on the energy employed it may affect the surface quality by the formation of a recast layer and cracking on the surface being wire-EDM'ed.

The impact of wire-EDM machining process on the friction and wear response of cemented carbides have been already elucidated in reciprocating sliding motion, e.g. (Bonny et al, 2010 and Perez Delgado et al, 2010). However, there is a vague scientific perception of the influence of wire-EDM at high temperature on friction response of cemented carbides under continuous sliding contact.

This paper aims to investigate the friction response of WC-6wt%Co pins against WC-10wt%Co plates with different surface finishes attained by grinding or wire-EDM in rotating sliding experiments performed at room and high temperature (400 °C) and examines the interaction of the originated oxide layer and wear particles.

2. Experimental procedure

Test specimens
The WC-10%wtCo cemented carbides were produced by liquid phase sintering (LPS). It is a process for forming high performance, multiphase components from a powder which involves sintering under conditions where solid grains coexist with a wetting liquid. The test material displays an E-modulus of 541 GPa, a Vickers hardness HV_{10} of 1685 kg/mm^2, a compressive strength of 6.6 GPa, fracture toughness $K_{IC,10kg}$ of 11 MPa m$^{1/2}$ and an electrical resistivity of 1.7 x 10^{-7}Ω.m.

The young's modulus, E, was obtained by resonance frequency method (ASTM C 1259-94) on a Grindo-sonic (J.W. Lemmens, Elektronika N.V., Leuven, Belgium). The Vickers hardness was measured with indentation weights of 10 kg (Model FV-700, Future-Tech Corp., Tokyo, Japan). The fracture toughness, $K_{IC,10kg}$, was obtained by Vickers indentation, see (Shetty et al, 1985). The electrical resistivity was obtained by the 4-point contact method using a Resistomat Mikroohmmeter (Type 2302, Gernsbach, Germany).

Surface finish
The plate samples of WC-10%wtCo were machined and surface finished by grinding and wire-EDM, thus obtaining final dimensions of 4 mm x 38mm x 58 mm. The grinding was done using JF415DS grinding equipment (Jung, Göppingen, Germany) with a diamond abrasive wheel (type MD4075B55, Wendt Boart, Brussels, Belgium). Furthermore, wire-EDM was achieved using ROBOFIL 2030SI technology (Charmilles Technologies, Switzerland) in de-

ionized water with dielectric conductivity of 5 µS/cm. This machining process involves several steps ranging from a rough cut to smooth surface finish. In this paper a fine EDM surface finish was chosen and identified as 'E21'through the text.

The surface roughness of the WC-10wt%Co cemented carbides was measured using surface profilometry (Somicronic® EMS Surfascan 3D, type SM3, needle type ST305) according to the ISO 4228 standard. R_a values of 0.22 µm and 0.23 µm for ground and wire-EDM'ed specimens, respectively, were obtained. It is worth noting that the R_a roughness level of both surface finishes is very similar and could be subjected to comparison.

Wear testing
Wear tests were carried out at temperatures of 25 and 400 °C employing a pin – on – disk high temperature tribometer (CSM Switzerland, maximum temperature 1000 °C). The tests were performed according to the ASTM G99-95a standard under atmospheric conditions, mean Hertzian contact pressure of 2.06 GPa, sliding speed of 0.3 m/s and a total sliding distance of 10000 m. WC-6wt%Co pins were used as static counterpart with a radius of 6mm. The Vickers hardness ratio pins/specimens > 1.1.

3. Results and discussion

Influence of surface finish on friction coefficient
The effect of fine wire-EDM on friction response of WC-10wt%Co cemented carbides with respect to the ground material is illustrated in Fig. 1. Each value in the curve is an average of at least 3 wear experiments performed under identical conditions, with deviations of less than 10 %. Fig. 1 indicates that at 25 °C, sliding speed of 0.3m/s and, mean Hertzian contact pressure of 2.06 GPa and a sliding distance of 10000 m the change of dynamic coefficient of friction is similar for both surface finishes. The obtained friction curves show an increment during the first sliding meters, subsequently decline towards an equilibrium state after running-in. This can be explained in terms of continuous breaking of asperities. However, the wire-EDM'ed samples have randomly evidenced higher friction values during the course of the test and finally there is sudden increase in the last 2000 m. It can be attributed to the presence of wear debris particles and continuous breaking and regenerating of micro-junctions at the contact surface during sliding, and the deteriorated surface quality attained by wire-EDM machining.

Fig. 2 shows the dynamic coefficient of friction of the tribological combinations, which exhibit average values of 0.37 and 0.39 for ground and wire-EDM surface finish, respectively. Nevertheless, the dynamic coefficient of friction reached values up to 0.48 for fine wire-EDM'ed samples, which is in agreement with results obtained in reciprocating sliding motion experiments as reported by (Bonny et al, 2010).
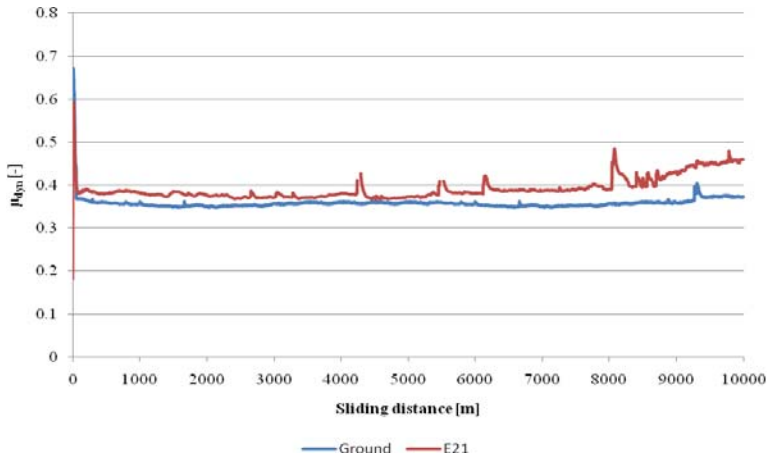
Figure 1. On-line monitoring of dynamic coefficient of friction versus sliding distance of ground and wire-EDM'ed WC-10wt%Co against WC-6t%Co pins (p$_{mean}$ 2.06 GPa, speed 0.3 m/s)
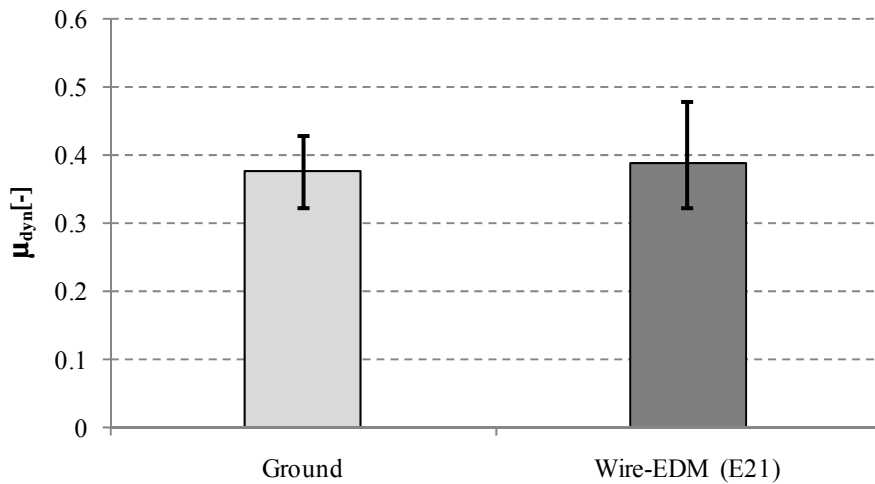

Figure 2. Post-mortem fluctuation and mean value of friction coefficient for ground and wire-EDM'ed WC-10wt%Co, p$_{mean}$ 2.06 GPa, speed 0.3 m/s, 10000 m.

Influence of high temperature on friction coefficient

Fig. 3 shows the minimal, maximal and mean values of dynamic friction coefficient of ground WC-10wt%Co in rotating sliding contact with WC-6wt%Co applying a mean Hertzian contact pressure of 2.06 GPa, a sliding distance of 10000 m, a sliding speed of 0.3 m/s and temperatures of 25 and 400 °C. As can be seen in Fig. 3, the fluctuation range of the friction coefficient becomes larger at 400 °C. Furthermore, the average friction coefficient is more than two times higher at 400 °C compared to friction at room temperature. Mechanical properties

and chemical stability of cemented carbides can strongly be affected by increased temperature. For instance, the transverse rupture strength decreases by increasing the temperature up to 600 °C, see (Ueda et al, 1976). This strength reduction could result in crack propagation on the surface, thus causing more adhesive friction as a consequence of interlocking of wear debris due to irregular shape. Additionally, the generated oxide layer consisted basically of WO_3 and small amounts of Co, CoO, and WC, as reported by (Sheikh-Ahmad and Bailey, 1999).
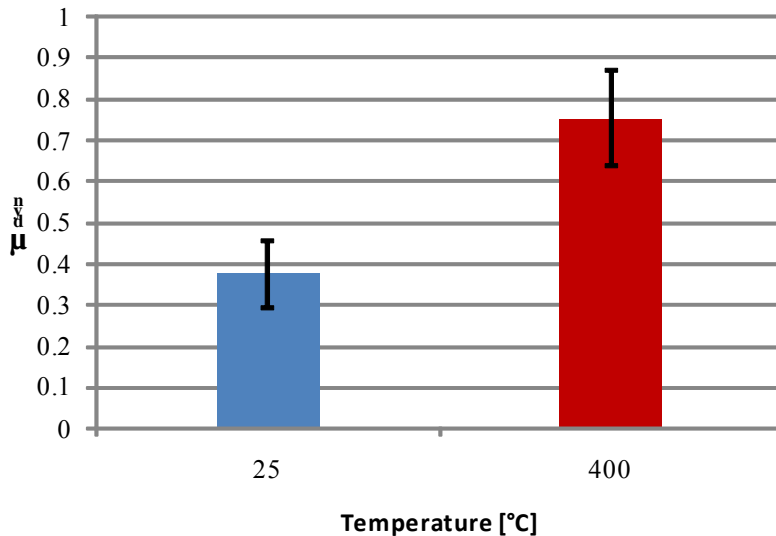

Figure 3. Influence of temperature on dynamic friction coefficient of ground WC-10wt%Co in rotating sliding contact with WC-6wt%Co using a mean Hertzian contact pressure of 2.06 GPa, a sliding speed of 0.3 m/s and a sliding distance of 10000 m.

Identification of wear mechanisms

The discrepancy in friction response between wire-EDM and ground surface finishing conditions could be essentially attributed to the lower surface quality as a result of the thermally affected layer on the wire-EDM surface. SEM analysis on top of the wear track of wire-EDM'ed WC-10wt%Co alloys with wire-EDM surface finish E21 is presented in Fig. 4. A combination of the base material and the adhered debris layer can be observed in the wear track. Basically, the main wear mechanisms identified are surface binder expulsion, abrasion, grain cracking and grain pull out. The binder phase is partially removed by a combination of plastic deformation and abrasive ploughing grooves and fracture of the adhered debris layer. A more prominent occurrence of wear mechanisms can be encountered on the wire-EDM'ed WC-10wt%Co compared to the ground specimens.
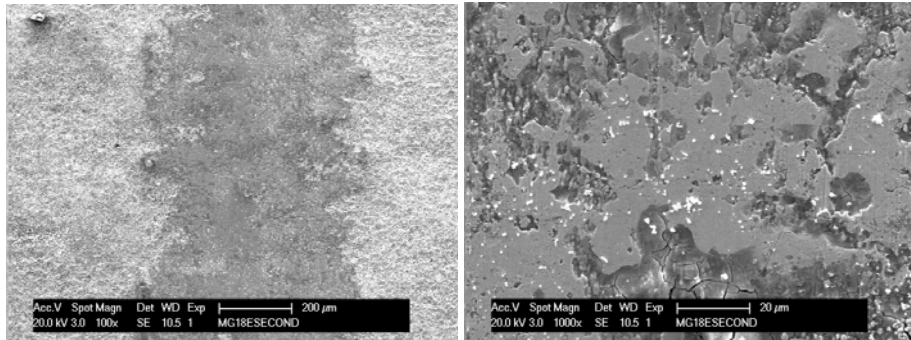
Figure 4. SEM view on central wear track surface of fine wire-EDM'ed grade WC-10wt%Co (a) 100X and 1000X (b) slid against WC-6wt%Co for 10000 m at 0.3 m/s with p_{mean} 2.06 GPa

Visual inspection of worn surfaces after wear testing at 400 °C revealed the presence of wear debris accumulated both outside and inside the wear tracks. A smoother optical aspect was observed on the wear surface compared to wire-EDM and ground surface finish. Additionally, a colored oxide layer was observed on the wire-EDM'ed surface. Nevertheless, further investigation of the oxidation layer, debris layer and wear mechanisms in the specimens tested at high temperatures will be carried out by means of scanning electron microscopy (SEM), energy dispersive X-ray (EDX) spectroscopy and XPS measurements on wire-EDM'ed WC-10wt%Co.

4. Conclusions

Rotating pin-on-plate experiments on WC-10wt%Co cemented carbide plates surface finished by grinding and wire-EDM and slid against WC-6wt%Co pins at room temperature or at 400 °C revealed that the friction response is significantly affected by contact temperature and surface finishing condition. The highest friction was encountered for wire-EDM'ed surfaces, which can be related to the thermal impact of the EDM process, involving at the same time more prominent occurrence of wear mechanisms such as grain and binder removal, grain cracking, formation and delamination of debris layer, polishing and abrasion. Furthermore, the dynamic friction coefficient at high temperature was more than two times higher compared to the friction level at room temperature. The generated wear particles and the oxide compound layer in the wear track will be examined more in-depth in a near future investigation.

5. Acknowledgements

References

1. Bonny K., De Baets P., Perez Delgado Y., Vleugels J. and Lauwers, B. (2010), Friction and wear characteristics of WC-Co cemented carbides in dry reciprocating sliding contact, Wear, 268,11-12, , pp 1504-1517.

2. Glaeser W.A. (1998), ASM Handbook, Friction, Lubrication, and Wear Technology, Volume 18, Section: Materials for friction and Wear Applications.

3. Perez Delgado Y., Bonny K., De Baets P., Malek O., Vleugels J. and Lauwers, B. (2010), Tribological behavior of wire-EDM'ed ZrO2-composites and cemented carbides, Sustainable Construction and Design.

4. Sheikh-Ahmad J. Y., Bailey J.A. (1999), High-temperature wear of cemented tungsten carbide tools while machining particleboard and fiberboard, Journal of Wood Science, 45, pp 445-455.

5. Shetty D. K., Wright I.G., Mincer P. N. and Clauer A. H. (1985), Indentation Fracture of WC-Co Cermets, Journal of Materials Science 20, 5, pp 1873-1882.

6. Ueda F., Doi H., Fujiwara F. and Masatomi H. (1977), Bend deformation and fracture of WC-Co alloys at elevated temperatures, Materials transactions, Vol.18, pp 247-256.

7. Zhengui, Y., J.J. Stiglich, T.S. Sudarshan (1998), WC-Co enjoys proud history and bright future. Metal Powder Report 53(2), 32–36.

Turning of zirconium-dioxide ceramics

Gellért FLEDRICH, István PÁLINKÁS, Róbert KERESZTES,
László SZABADI, László ZSIDAI, Gábor KALÁCSKA

Institute for Mechanical Engineering Technology,
Faculty of Mechanical Engineering, Szent István University

Abstract

The importance of ceramics used in engineering practice is more and more greater. We have planned and accomplished an individual measuring system for turning ceramics. During turning we measured the main cutting forces and the cutting forces in feed rate. To evaluate the practical applicability of ceramic surfaces turned and grinded originally, to compare the tribological behaviour we have also assembled a laboratory measuring equipment by which we measured the frictional force on steel counter-surface grinded at dry friction condition.

We have determined with mathematical-statistical methods the variables of the main cutting forces connections to be found in literature from the measuring results of cutting force. After tests we have analysed the electron-microscope exposures of the surfaces cut concerning the surface cracks and pittings. We also determined the 3D surface characteristics with surface topography measuring method. We proved with complementary, comparative thermo-camera examinations the forming of arising heat-circle at the contact of cutting tool.

Keywords

ZrO_2-MgO ceramic, turning, surface

1. Introduction

The engineering ceramics are such constructional materials which can be used at essentially higher temperature comparing to materials used till now, at under heavy physical and chemical load.

The claim to structural ceramics is continuously increases with the development of the industry and they can get important part just in this segment. The zirconium-dioxide is also such material. The development of manufacturing finished – and intermediate products claim the cutting of more and more complex surfaces [1-4]. The more economical machining of spatial surfaces claims the further development of tools with regular edge. The zirconium-dioxide as basic material having lower hardness and other characteristics is suitable to machine by tool with regular edge, so in case of piece production or in case of small and medium series manufacturing, at quick prototype-manufacturing it can become potential material alike [5-9]. Its cutting and

machinability characteristics has to be known that this could be ensue. Our research work concentrates to one part of this, in accordance with the recommendation of a company producing and developing zirconium-dioxide semi-finished product. The main steps:

- – Testing the cutting characteristics of the engineering ceramics in case of machining by single-point cutting tool at turning.
- – Developing measuring system to measure the main – and feed rate direction forces during cutting.
- – Topographic test of surfaces after machining with cutting parameters set. Analysing the micro-cracks formed possibly on the surface and the shell – like pittings.
- – Examining the heat affected zone arising during cutting.
- – Comparing the cutting characteristics of ceramic with the cutting characteristics of lamellar – and globular cast-irons.
- – To compare the arising frictional characteristics in case of dry friction condition in case of ceramic – steel surface pairs machined with different sets.

2. Material and method

During tests we have machined the surface of ceramic with different settings. Based on preliminary measurings we established that it is expedient to choose the depth of cut between 0,01 and 0,05 mm, the feed rate should be between 0,01 and 0,05 mm/rev. immediately at the tool edge. We also carried out preliminary measurings concerning the approximate value of the cutting speed, this was around 50 m/min. After turning we made surface topography as well as electron microscopic exposures from the surfaces machined and we analyzed those. We have measured the dry frictional characteristics of the ceramic / steel material pair with comparing character as a further test of the surfaces turned and grinded of the ceramic.

The materials tested
Zirconium-dioxide ceramic specimen

The characteristics of the ZN 40 engineering ceramic is that it has got favourable physical and chemical characteristics at high temperature range. It has got high hardness (1250 HV), because of this it can be cut only with polycrystal diamond and with cubic boron nitride tools. The material tested is a zirconium dioxide ceramic stabilized with magnesium. The diameter of the cylindrical specimens was 16 mm used at turning tests.

Cast-iron and Steel specimen

As a reference materials were used.

Single-point cutting tool

The cutting tool was a tipped turning tool with 12x12 –shank. I have carried out my tests with two kinds of inserts (tips) with cubic boron nitride (CBN) and

with polycrystal diamond (PCD). It is expedient to carry out such hard cutting with these materials.

Cutting tests
To measure the axial and tangential components of the cutting force I applied resistance force-meter-tool head between the tool-head and tool shank developed and manufactured by me. It makes possible to measure the feed rate force (F_f) and the cutting force (F_c) in case of straight turning in this form.

Surface topographical tests
Because of the increasing requirements created against surfaces machined there is a need to evaluate many-sided the surface micro-topography which means the surface characteristics by writing up data collected from the sampling surface. I have made electron microscopic exposures from the ceramic surface machined with different cutting parameters as well as from surface grinded.

Friction tests
I have made an equipment to carry out tribological tests. During the test I pressure the steel counterface with determined normal direction force the casing surface of the rotating ceramic specimen and in the meantime I measure the value of the friction force with force meter cell. I have calculated the friction coefficient characterizing the system from the normal direction force and the friction force as well as I measured the wear of the steel specimen and its deformation.

Complementary tests with thermo-camera
The heat developing during cutting has got a great effect on the material removal process as well as it effects strongly the tool service-life. To study the heat affected zone developed I made exposures with thermo-camera during cutting. Considering that the basic material chosen by me for to be machined is significantly more rigid the heat deriving from internal friction presents oneself probably in smaller amount.

3. Results

Cutting tests results of ceramic
During tests I have measured the values of the main – (F_c) and feed rate (F_f) cutting forces. Table 3.1. contains the parameters set in the cutting system. I have determined the characteristic content and the exponents to given parameter of the empirical connection (feed rate, depth of cut, cutting speed) taking into also account the cutting speed from the values of main cutting force measured by using mathematical statistical methods.

   The Figure 1. shows the characteristic values of measurings carried out with CBN – tool at uniformly increasing cutting speed. The cutting speed (v_c)

measured along the horizontal axis the cutting forces (F_c; F_f) can be found on the vertical axis.

Table 1. Main characteristics of measurings

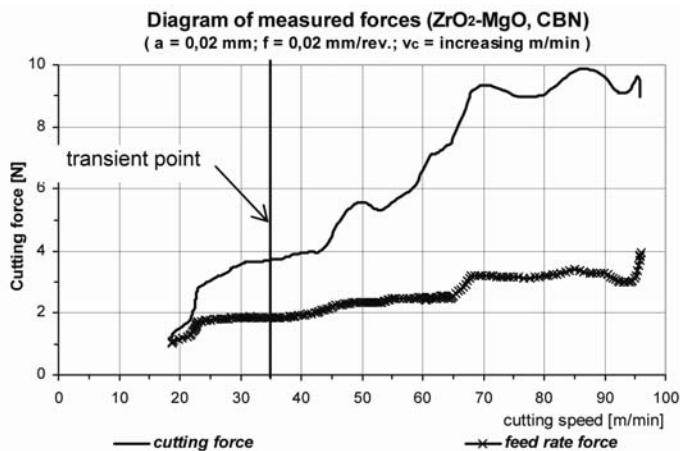|	Ceramic, ZrO_2	Globular cast iron, GJS-400-15	Lamellar cast iron, GJL 200
Cutting speed, v_c [m/min]	25 / 75		
Depth of cut, a [mm]	0,01 / 0,02 / 0,03 / 0,04 / 0,05	0,02	
Feed rate, f [mm/fordulat]	0,01 / 0,02 / 0,03 / 0,04 / 0,05		
Ambient temperature, T [ºC]	23		
Length of casing tested, s [mm]	per feed rate 3 mm, altogether 15 mm		
Tool material	PCD / CBN		

Figure 1. Diagram of main and feed rate forces.
(v_c= changing m/min., a= 0,02 mm, f= 0,02 mm/rev.;
ceramic: zirconium dioxide, tool: CBN)

It can be seen that value of the small forces arising at the beginning of cutting increase. After the transient point the value of the main cutting force increased significantly with the increasing of the cutting speed at cubic boron nitride (CBN) tool.

In case of CBN-tool material the amount of feed rate forces are approximately the half of the amount of main cutting force. The value came about the cutting force with diamond (PCD) tool. The two forces at the two kind of tools show similar characters in their trends.

I also show the change of the cutting forces in the next diagram (Figure 2). I set the cutting speed to 25m/min. value. The value of the depth of cut was 0,02 mm. I changed the values of the feed rate according to f=0,01;-0,02;-0,03;-0,04;-0,05 mm/rev.

The main cutting force increases with the increase of the feed rate, however the value of the feed rate force almost hardly changes. At a=0,04 mm depth of cut the great degree deviation of the main cutting force allows to conclude to the damage of the cutting edge. That was proved later by microscopic exposures.

It is also significant the running up of the feed rate force in the beginning range. Both the ceramic and the tool are at ambient temperature in the beginning first point. During cutting significant amount of heat developed and warning up starts. As an effect of this the value of the force increases to a certain time then sets in a near constant value it can be seen in the diagram.
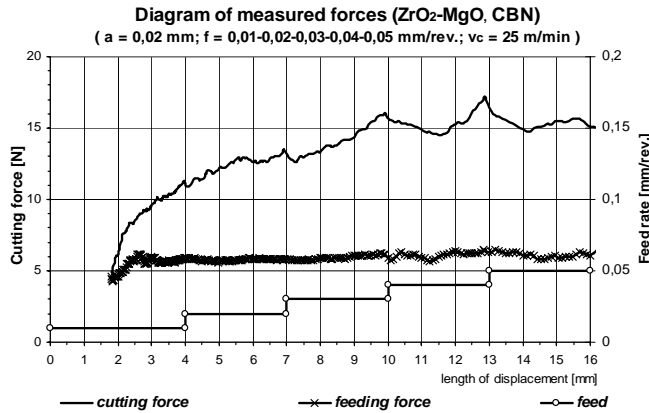

Figure 2. Diagram of main and feed rate forces.

I have also measured the changes of the main cutting force in accordance with the formers to the polycrystal diamond tool. The value of the cutting speed was, v_c=25m/min. The value of the depth of cut was, a=0,02 mm. The values of the feed rate were, f=0,01;-0,02;-0,03;-0,04;-0,05 mm/rev.
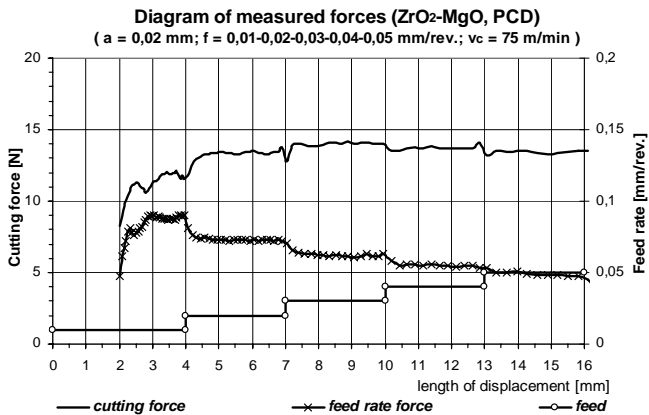

Figure 3. Diagram of main and feed rate forces.

The trends are similar to the cubic boron nitride tool. The cutting force shows increasing tendency, while the feed rate force set in to a certain value, then showed slight decrease.

The cutting force at higher cutting speed (Figure 3) set in a nearly constant value following a steep running up which was lower than at smaller (v_c=25 m/min.) cutting speed. The feed rate force following the running up or decreased or had got the same value. The tool edge caused the deviation of the feed rate force with great probability.

The diagrams so far showed the effect of the feed rate changing. I make known in the followings some diagrams at which I examined the effect of changing the depth of cut concerning to the main and feed rate cutting forces. I have set the cutting speed (v_c) to 75m/min. value. The value of depth of cut were, a=0,05;-0,04;-0,03;-0,02;-0,01 mm at casing turning. The values of the feed rate were, f=0,02 mm/rev. I carried out the tests only with PCD-tool giving more favourable surface characteristics.

Diagram of measured forces (ZrO₂-MgO, PCD)
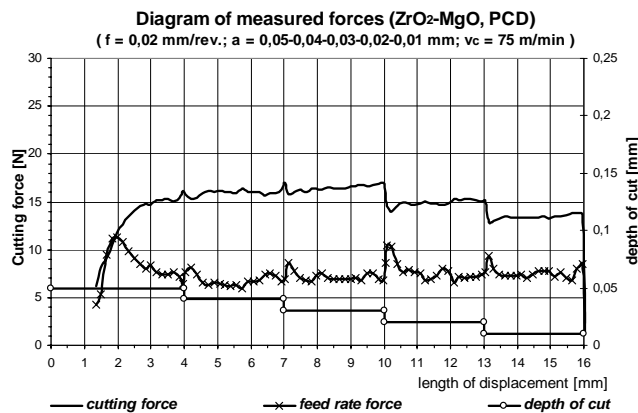**(f = 0,02 mm/rev.; a = 0,05-0,04-0,03-0,02-0,01 mm; vc = 75 m/min)**

Figure 4. Diagram of main and feed rate forces.

The Figure 4 shows the change of the main cutting and feed rate forces taking place of changing the depth of cut. It can be stated that the changing of the depth of cut over a=0,02 mm doesn't effect significantly the value of the main cutting force. In case of machining with higher cutting speed (v_c=75m/min.) comes about lower main cutting force values.

Edge test results of the cutting tool

We have made exposures with optical microscope from the turning tool inserts (Figure5). During cutting the main cutting edge got pittied in low-rate. This pitting also can be seen on the force diagrams. In the first exposure the original polycrystal diamond insert can be seen. In the second exposure already a piece pittied from the edge, the shell-like pitting can be seen. Other pittings were

formed using the tool longer. These pittings change significantly the edge geometry although the tool remained suitable further on, too. The quality properties of the surface cut by pittied insert are worse with high probability and show greater standard deviation than the inserts with regular edge geometry.
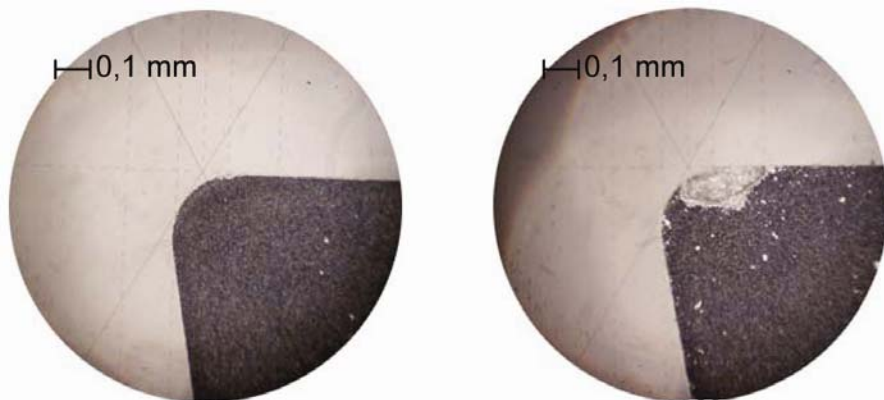

Figure 5. Microscopic exposures, PCD-tool, the original cutting insert,
first pitting and further pittings

Determining the cutting force in the function of parameters

The sources of literature to the cutting force (Horváth and Co. 1995; König and Co. 1997, Dudás 2000) use a theoretical relation worked out first of all to steels which is the following in the function of cutting parameters:

$$F_c = C_v \cdot f^{\,x} \cdot a^{\,y} \cdot v_c^{\,z} \; [N]$$

Our aim is with the planned tests to be carried out to decide the usefulness of the preceding equation at cutting ceramic and to determine the necessary parameters with multivariate linear regression.

The mathematical function matched to the results of tests planned:

$$F = 477{,}183 \cdot f^{\,0,1646} \cdot a^{\,0,4397} \cdot v_c^{\,-0,2994}$$

It is important to mention concerning the usefulness of the equation that this relation describes the formation of the measuring results within the parameter – range determined in the test plan.

Results of surface check with scanning electron microscope

For the sake of greater magnification we have made scanning electron microscopic exposures in 100x, 500x then 2000x-times magnifications from the ceramic surface machined.
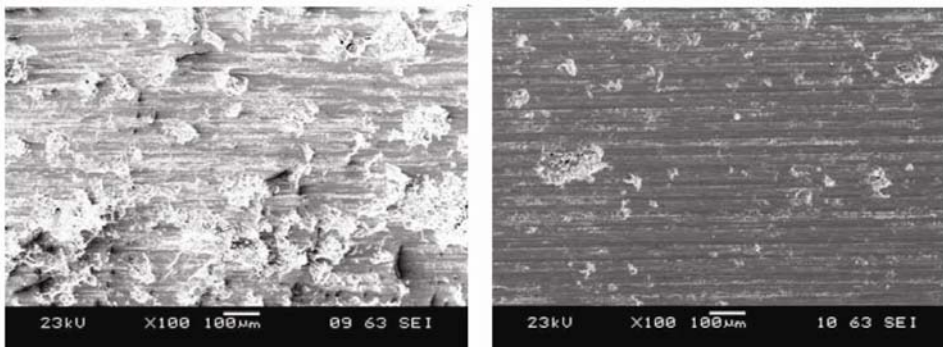
Figure 6. Ceramic surfaces turned with CBN and PCD tools. v_c=75 m/min.,
f=0,04 mm/rev., a=0,02 mm, N=100x

The machining is strongly slashed, very rough, cratered in Figure 6, on the exposure of surface machined with CBN-tool. The turning with PCD-tool resulted less and smaller craters. The cutting direction can be well seen. The tool point formed the surface into serrated.

The original grinded surface electron microscopic exposure can be seen in Figure 7. The amount of craters as a result of machining can be considered identical with the machining with PCD-tool. (Figure 6.). However the dimension of craters formed are 30-40% greater. This dimensional difference can increase the lubricant keeping capacity of the surface. The grinding grains made also the surface into serrated but because of the smaller dimension of grains the ditches, grooves, scratches dimension are also smaller:
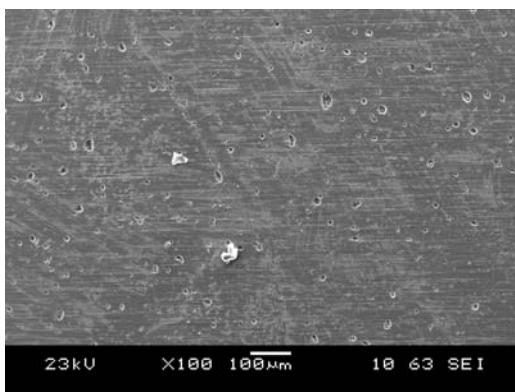

Figure 7. Ceramic surface grinded

The exposures with 2000x magnification prove the producing plastic (ductile) chip removal (Figure 8) which shows favourable surface-continuity. This proves the applicability of turning with polycrystal diamond.
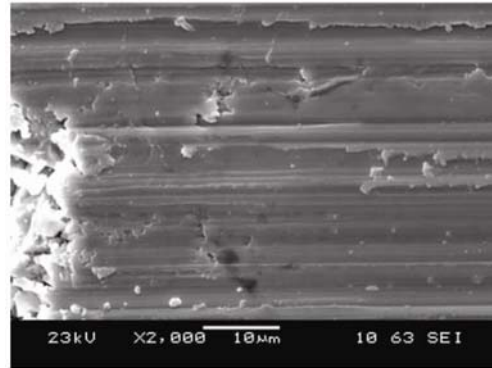
Figure 8. Surface turned with PCD-tool
v_c=75m/min., f=0,04 mm/rev., a=0,02 mm, N=2000x

As a recommendation the whole number multiple is a given of the natural logarithm basis ("e" number) of the hardness of material to be cut as the hardness of the tool material in the practice. The diamond as an usable tool material for machining ceramics is suitable for this requirement. There are such experiments rising as a possibility the machining with lower hardness material as a significantly different conditions can take place compared with machining steels. However these are not suitable for industrial purpose, yet.

Results of frictional model tests and their interpretations
On the casing surface of ZrO_2 ceramic tested at v_c=25 and 75 m/min. cutting speed and 5 different feed rate (f=0,01;-0,02;-0,03;-0,04;-0,05 mm/rev.) machined surface can be found. The width of these are 3 mm one by one. Figure 9 shows the value of arising friction force developed between the ceramic and the steel specimen. We distinguished the different surfaces with various colours and marks. The "k" marks the grinded surface while the numbers "1, 2, 3, 4, 5" mark the feed rates set during turning in hundredth millimeter.
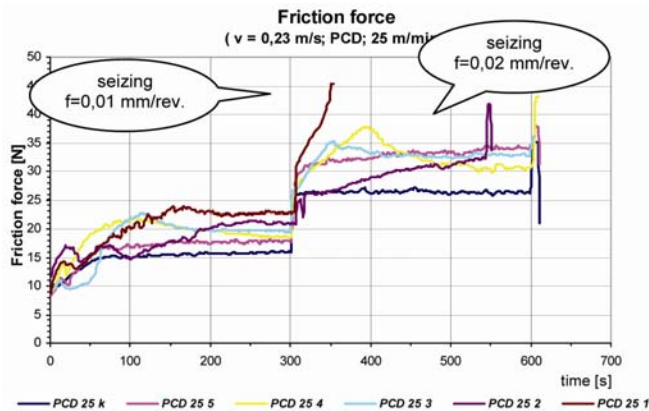

Figure 9. Friction force diagram (between steel/grinded and ceramic surface cut)

The friction force didn't show significant change on the surface grinded within identical load section. It set in a nearly constant value within short time (50s). The grinded surfaces also seized with imposing maximum load. It is striking on the diagram that the friction force increased in such a great extent on the 2. load level on the ceramic surfaces cut with 0,01 and 0,02 mm/re. feed rate, that the surfaces seized in this section. The seizing ensued on the 3. load level on surfaces cut with greater feed rate.
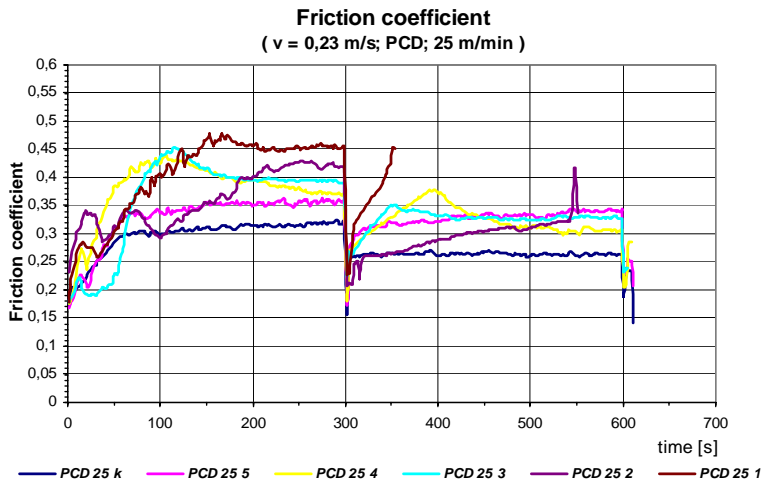
Friction coefficient
(v = 0,23 m/s; PCD; 25 m/min)

— PCD 25 k   — PCD 25 5   — PCD 25 4   — PCD 25 3   — PCD 25 2   — PCD 25 1

Figure 10. Diagram of friction coefficient
(between steel/grinded and ceramic surface cut)

It is evident from the values of friction coefficients (Figure 10) that higher µ values characterize the surfaces machined with smaller feed rate. The value of friction coefficient on the surface turned with f=0,05 mm/rev. feed rate remained at nearly constant value in the sections tested similar to the grinded surface. Fluctuating friction coefficient, characterizing seizure can't be observed.
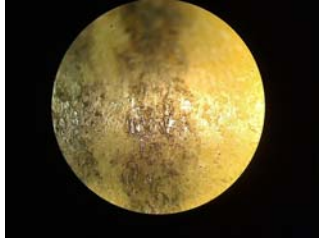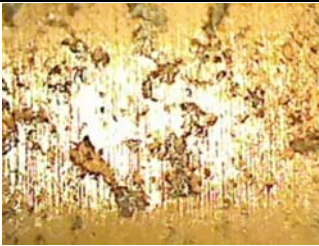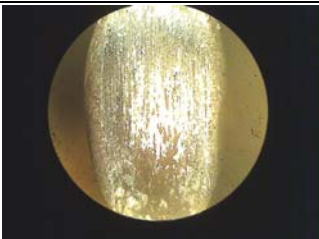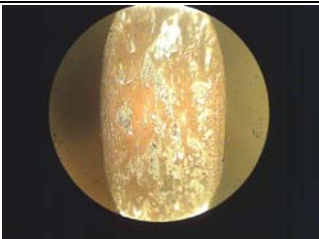
Microscopic comparison of sliding surfaces
I have made exposures from the dry sliding surfaces of ceramic and steel. The maximum magnification of the microscope was 40x. Two exposures are at disposal from both surfaces. One shows the whole sliding surface, the other shows a part of the sliding surface with 40x magnification. I show the sliding test carried out on the surface machined with a given feed rate in Table 2. Further exposures made from the surfaces can be found in the No. 2 supplement.

It can be seen well on the microscopic exposures of sliding track that at lower speed (v_c=25 m/min.) the machining is more rough, it resulted greater craters on the ceramic surface. These craters cut the steel surface in a greater extent during sliding test and thus they were filled up with steel faster. After this adhesive

connection could develop at certain places between identical materials (steel plate and steel particles stick into craters). This accelerates the seizing process significantly.

Table 2. Microcopic exposures of sliding surfaces
(machining parameters: v_c=25 m/min., 75 m/min.; f=0,02 mm/rev.;
a=0,02 mm; test parameters: v_k=0,23m/s; F_n=50N, 100N; 150N).

tool: PCD	cutting speed 25 m/min	cutting speed 75 m/min
feed rate f = 0,02 mm/rev.	ceramic surface	ceramic surface
	ceramic surface 40x	ceramic surface 40x
	steel surface	steel surface
	steel surface 40x	steel surface 40x

4. Conclusions

- We establish in the test field that in case of ZR40 (ZrO_2-MgO) ceramic basic material with the CBN and respectively PCD tool types having regular edge geometry chosen by me can be reached plastic (ductile) chip removal during turning in the cutting parameter field set (a=0,02 mm; f=0,01-0,02-0,03-0,04-0,05 mm/rev.; v_c=25-75 m/min.).

- We have proved with my measurings that in the upper range of the cutting speed of test field the polycrystal diamond tool is more favourable at turning zirconium-dioxide ceramics stabilized with magnesium it can be used with smaller cutting force than the cubic boron nitride tool. Furthermore we have established that the polycrystal diamond (PCD) resulted cutting force similar to the cubic boron nitride at lower (v_c=25 m/min.) testing cutting speed. The occurrence experienced at different frictional processes.

- I have established in the test field that the cutting force at uniformly increasing cutting speed in case of zirconium-dioxide ceramic and lamellar cast iron shows increasing tendency-contrast with the connection concerning steel machining to be in the technical literature. In case of lamellar cast iron used as reference material in v_c=40-50 m/min cutting speed range a transient zone comes about to the cutting force, before which there is an increasing section to be approximated with different incline linear depending on the tool, while following that the cutting force is constant or it has got a nearly constant value. The transient zone also can be measured at turning with PCD-tool in case of 40-50 m/min cutting speed but the trend is contrasted: at lower speed nearly constant cutting force can be measured, above this a continuously increasing force-trend appears. In case of CBN tool there is also a transient zone belonging to 40-50 m/min. cutting speed at which in case of lower speeds appeared a continuously increasing cutting force, after the transient zone the force increase is still steeper respectively.

- I have proved with mathematical-statistical methods that the connection concerning the main cutting force $F_c = C_v \cdot f^x \cdot a^y \cdot v_c^2 [N]$ to be found in the technical literature in the tested parameter field (f=0,02-0,04 mm/rev,; a=0,02-0,04 mm; v_c=25-75 m/min.) can be extended to turning ZrO_2-MgO ceramic with PCD tool (with the edge geometry defined). I have determined with my measurings the values of the constant and exponents – C_v=477,183 - - x=0,1646- - y=0,4397 - - z=-0,2994 – and I proved that the connection can be applied with 95% probability with on the parameter interval tested.

- I have proved with friction tests (block-on-ring tribological system, St37F grinded steel (R_a=0,8mm) "block" surface, without lubrication, ceramic "ring" specimen) that at high turning cutting speed (v_c=75 m/min.) and at small feed rate (f=0,01-0,02 mm/rev.) the friction resistance is smaller on the ceramic surface. The surface grinded has got smaller dimension but into the great number shell pittings the steel worn particles seat quickly, which transforms the ceramic/steel friction

connection into steel/steel characteristic friction, which increases significantly the adhesive component of the friction force.

References

1. Fritz A. H., Schulze G. (Hrsg.) (2007): Fertigungstechnik. 8. Aufl *Springer Verlag, Berlin* 279. p.

2. Becher, P.F., Rose L.R.F. (1994): Toughening Mechanisms in Ceramic Systems. *Materials Science and Technology Vol. 11,* ed. by M. Swain, 568-627.

3. Claussen N., Rüle M., Heuer A. (1983); Science and Technology of Zirconia II, *American Ceramic Society, Advances in Ceramics* Vol. 12.

4. Hannik R. H. J., Kelly P. M., Muddle B. C. (2000): Transformation Toughening in Zirconia-Containing Ceramics. J. *Am. Ceram. Soc*. 83 461-487.

5. Hastings W. F. (1967): A new quick-stop device and grid technique for metal cutting research. *Annals of the CIRP*, vol. XV, pp. 109–116.

6. König W., u. Klocke F. (1997): Fertigungsverfahren. Bd. 1: Drehen, Fräsen, Bohren. 5. Aufl . *Springer-Verlag, Berlin, Heidelberg*.

7. Leopold J. (1980): Modellierung der Spanbildung – Experiment. *Wissenschaftliche Schriftenreihe der TH Karl-Marx-Stadt*.

8. Leopold J. (2000): The Application of Visioplasticity in Predictive Modelling the Chip Flow, Tool Loading and Surface Integrity in Turning Operations. 3rd *CIRP International Workshop on "Modelling of Machining Operations"* University of New South Wales, Australia.

9. Noordin Mohd. Yusof*, Affandi M., Zainal Hendrico, Denni Kurniawan (June 2008): Hard turning of cold work tool steel using wiper ceramic tool, *Jurnal Mekanikal, No. 25,* 92 – 105.

Effect of different fretting fatigue primary variables on relative slip amplitude

Reza HOJJATI TALEMI, Magd ABDEL WAHAB,
Patrick De BAETS, Jan De PAUW
Department of Mechanical Construction and Production,
Faculty of Engineering and Architecture, Ghent University

Abstract

Fretting fatigue is a phenomenon in which two contact surfaces undergo small relative oscillatory motion due to cyclic loading. Due to fretting fatigue, fatigue lifetime of components reduces considerably comparing to when no fretting takes place. There are more than 50 factors that can affect fretting fatigue behavior of material such as, coefficient of friction, contact pressure, slip amplitude, cyclic axial stress, interface stress distribution, etc. These variables can be divided in two set of primary and secondary variables. Some variables such as cyclic axial stress, magnitude of slip, coefficient of friction and normal contact stress that have more influence on fretting fatigue lifetime are considered as primary variables. One of the challenging primary variables parameter that has significant effect on lifetime of component is slip amplitude. Experimental study of slip amplitude measurement at contact interface is either very difficult or not very accurate so that numerical techniques are really desirable to overcome the experimental test difficulties. In this study, we introduce a new approach in order to find the relation between slip amplitude and two other primary variables; namely axial stress and normal contact stress using finite-element. Numerical simulations are done to monitor the slip amplitude at contact interface with different axial and normal-contact stresses ranges. Then based on numerical design of experiments technique, the interaction of these two primary variables on fretting fatigue slip amplitude is monitored.

Keywords

fretting fatigue, primary variables, slip amplitude, finite element

1. Introduction

Fretting occurs due to oscillatory relative displacement between two bodies that are in contact together, which results in damage at contact interface. Depending on contact conditions (i.e. surface finish, coefficient of friction (COF), etc.) and mechanical variables (i.e. axial stress, contact stress and slip amplitude), fretting damage at contact interface can cause either crack initiation and growth leading

to catastrophic failure (fretting fatigue), or fretting wear or combination of both. Fretting fatigue is a serious phenomenon, which results in reduction of fatigue lifetime of component comparing to when no fretting takes place.

Figure 1 shows Silver Bridge (LabSpace, 2011), that was an eye-bar-chain suspension bridge built in 1928. The bridge connected West Virginia and Ohio over the Ohio River in United State. On December 15, 1967, the Silver Bridge collapsed while it was full of rush-hour traffic, resulting in the deaths of 46 people. Investigation of the wreckage pointed to the cause of the collapse being the failure of a single bolted connection in a suspension chain, due to fretting fatigue phenomenon. Actually after that disaster this type of connection never used again but there are a lot of applications that are still subjected to fretting fatigue such as bolted and riveted structures, gas and steam turbines, bearing shafts, steel cabals and so on.
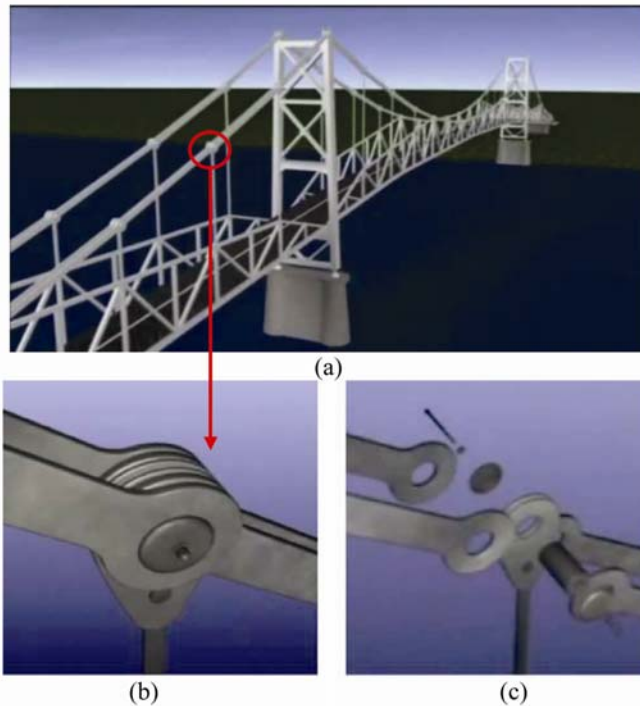
Figure 1. Silver Bridge disaster 1967, (a) Suspension bridge, (b) assemble view of eyebar-chain, (c) explode view of eyebar-chain

Figure 2 illustrates the relation between two connected bodies in bolted structure that are subjected to oscillatory motion due to variety of cyclic loads. The load transfer to the structure takes place on a local scale, though, at the bolt/ plate interface. The remote global stress causes shear stress at contact interface and normal contact stress comes from tightening of nut.
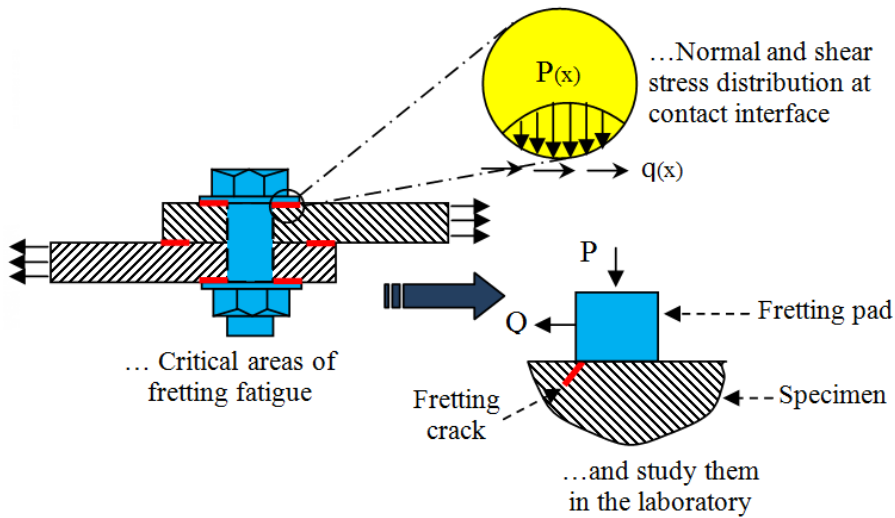
Figure 2. Shematic view of fretting fatigue problem in bolted connections

There are more than 50 factors that can affect fretting fatigue behavior of material such as, coefficient of friction, normal contact stress, slip amplitude, cyclic axial stress, interface stress distribution, etc. These variables can be divided in two sets of primary and secondary variables (Dobromirski 1992). Some variables such as cyclic axial stress, magnitude of slip, coefficient of friction and normal contact stress that have more influence on fretting fatigue lifetime are considered as primary variables. One of the challenging primary variables parameter that has significant effect on lifetime of component is slip amplitude.

In order to characterize fretting fatigue and fretting wear behaviors one of the well-known Fretting maps is introduced by (Vingsbo and Soderberg 1988). The relative slip between contact surfaces was assessed through the relative displacement or strain between two points, one on the fretting pad and the other on the specimen. Based on this measurement, two types of map were proposed:

(I) fretting map based on contact conditions (stick, partial and gross slip), and (II) fretting map based on material response, considering non-degradation, cracking and wear that depend on normal contact stress and relative slip for a given experimental conditions.

These maps are useful to characterize fretting conditions including damage. But the technique that was used to monitor slip amplitude at contact interface was old and the local slip amplitude could not be measured. Besides, all the data in these maps are based on global slip amplitude measurements.

As the role of local slip amplitude in fretting fatigue phenomenon is crucial, thus in this investigation numerical technique is used to monitor the contact stresses and slip amplitude at contact interface, and consequently the effect of different primary variables on local slip amplitude.

For this purpose, a Finite Element (FE) model of geometric configuration shown in Figure 3 is developed using python programming language in ABAQUS, for parametric study of different primary variables in fretting fatigue problem. The radius of contact surface of pad is 25 mm. Also specimen length, width and thickness are equal to 20 mm, 2 mm and 6.35 mm, respectively. The pad and the specimen are made from aluminum alloy Al7075-T6 with ultimate strength and yield stress of the material equal σ_{ult}= 590 MPa and σ_y= 503 MPa, respectively. The FE model is verified through comparison to the analytical elastic solutions (Hills and Nowell 1994).

One approach to studying the interaction effects between two or more factors in an experimental program is known as factorial design. This efficient experimental strategy, which often falls under the more generic term 'design of experiments,' calls for the variation of factors together with a final aim of relating the change in experimental response to the change in the factors. Often used in industrial research and development or process improvement, factorial design and subsequent statistical analysis of the experimental results can provide a method for quantitative identification of not only main effect of factors, but also any potential interaction between factors. In this paper, after getting the output data from parametric study the effect of two of primary variables namely axial stress and contact pressure on slip amplitude is investigated. This understanding will help us to choose appropriate boundary conditions for modeling the actual fretting fatigue problems in laboratory and numerical codes.
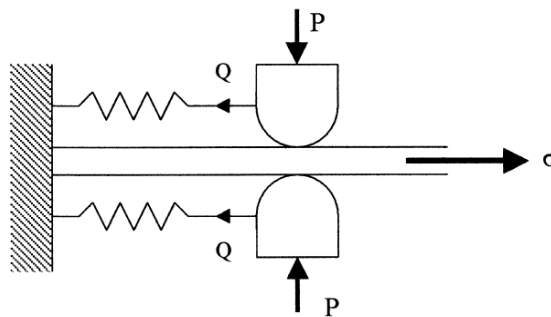
Figure 3. Configuration of fretting fatigue experiments:
specimen on contact with cylindrical pad.

2. Background

In order to verify the FE model and its numerical results of the fretting fatigue problem, a brief description of the relevant theory with known analytical formulations and solutions is given in this section.

In fretting fatigue problem the contact stresses play significant role. In order to calculate normal stress distribution at contact interface Hertz contact model can be used.

$$P(x) = -P_0 \sqrt{1 - \left[\frac{x}{a}\right]^2}$$

(1)

Where $P(x)$ is normal contact stress distribution, P_0 is maximum normal contact stress and a is semi contact width. Hertz' original theory has been extended to cover the application of tangential loads and the presence of friction at the interface independently by (Cattaneo 1938) and (Mindlin R.D. 1953). The Coulomb friction model was employed:

$$q(x) < \mu P(x)$$

(2)

Where $q(x)$ is the shear traction at point x and μ is the coefficient of friction. In this case the Coulomb friction law is applied on a local basis, i.e. if the shear traction at any point is less than the critical value μp, no relative displacement occurs. However, if the Coulomb limit is reached at any point along the surface, the shear traction at this point is essentially the pressure scaled by μ.

$$q'(x) = -\mu P_0 \sqrt{1 - \left[\frac{x}{a}\right]^2}$$

(3)

If the global Coulomb limit is not exceeded, i.e. $Q < \mu P$, a central stick region will exist of width 2c:

$$\frac{c}{a} = \sqrt{1 - \frac{Q}{\mu p}}$$

(4)

A second shear traction in the region -c<x<c is given by:

$$q''(x) = -\mu \frac{c}{a} P_0 \sqrt{1 - \frac{x^2}{c^2}}$$

(5)

The problem is depicted in Figure 3; being similar to the configurations used in many fretting fatigue experimental studies, it provides a useful benchmark solution. The effect of the bulk stress is to create an eccentricity to the Mindlin-Cattaneo shear traction distribution (Hills and Nowell 1994):

$$q''(x) = -\mu \frac{c}{a} P_0 \sqrt{1 - \frac{(x-e)^2}{c^2}} \quad \text{where } e = \frac{\sigma_{axial} a}{4\mu p_0}, \text{ -a<x<a}$$

(6)

61

The overall shear traction across the contact is given by the superposition of $q'(x)$ and $q''(x)$, i.e.

$$q(x) = q'(x) + q''(x) \tag{7}$$

3. Slip amplitude

There is a significant amount of evidence that the most damaging scenario is one where a large portion of the contact interface sees no relative displacement (sticking) and the edges of contact experience small amplitudes of relative displacement (slipping). This effect is illustrated in Figure 4 (Vingsbo and Soderberg 1988), which shows that sticking contact and gross sliding are not as damaging as the partial slip regime. Figure 4 is taken from Experimental observations of surface cracks that nucleate at the edge of contact support the general notion that the behavior of interest is in the partial slip zones.
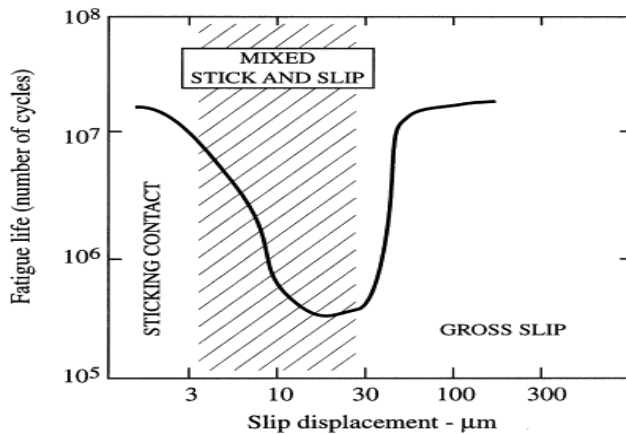
Figure 4. Schematic of fretting fatigue lifetime vs. relative slip amplitudes,
taken from (Vingsbo and Soderberg 1988)

As mentioned in the introduction section, this measurement is based on measuring global slip amplitude. However, at contact local interface, the amplitude of slip may be less and consequently the horizontal axis of this fretting map may change.

5. Fretting fatigue numerical contact model

Finite element software, ABAQUS (ABAQUS 6.10, 2011) is employed to solve the fretting fatigue problem shown in Figure 3. Configuration of fretting fatigue experiments is specimen in contact with cylindrical pad.

The geometry and loading conditions are shown in Figure 5, due symmetric condition shown in Figure 3, just half of specimen is modeled. A two-dimensional, four noded, plane strain quadrilaterial element is adopted for this finite element model. The circular surface of the pad is defined as a top (slave) contact surface and top surface of the specimen is defined as a bottom (master) contact surface. Both top and bottom contact surfaces are defined as a contact pair to model the possible contact region. The Lagrange multiplier of friction is included in the contact pair to define the friction behavior of the contact region (μ=0.5). The contact region is divided into stick and microslip regions. The stick region does not have relative movement between the top and bottom contact surfaces. The microslip regions show a small relative movement between the top and bottom contact surfaces, which is commonly observed in fretting.

The normal and shear stresses along the contact region can be also calculated from FE model. Since the stress components near the contact region are high and their distributions are quite complex, a very fine mesh (a four node quadrilateral element with size of 5 μm x 5 μm) is used in this region. The mesh used is also fine enough to capture the relaxed stress state near the trailing edge and the reverse slip near the leading edge. In order to model the effect of attached spring to the pad for generating tangential load Q (Figure 3) both side of pad are restricted to move in vertical direction then the reaction stress ($\sigma_{reaction}$) is applied at the other side of specimen so that Q can be calculated based on equation 8, where A_s is cross section area of specimen as shown in figure 5:

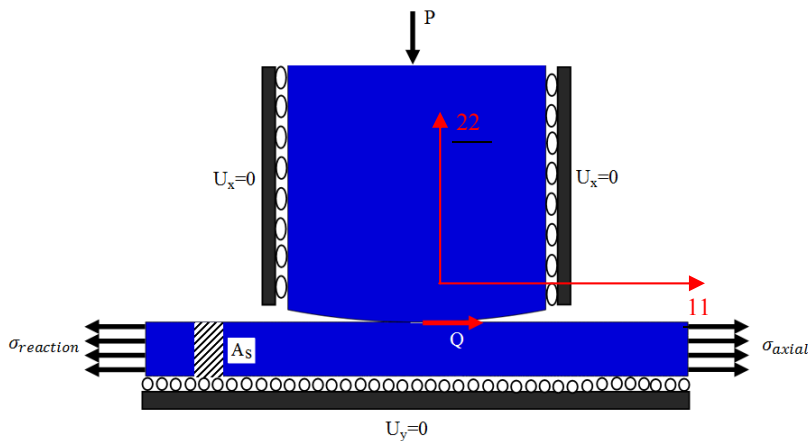*Figure 5*. Fretting fatigue general contact model

$$Q = \frac{\sigma_{axial}}{A_S} - \frac{\sigma_{reaction}}{A_S} \qquad (8)$$

Python programming language is used for parametric study in order to investigate the effect of different primary variables and their interaction effects

on slip amplitude. All design variables for this parametric study or Numerical Design of Experiments (NDOE) is tabulated in Table 1. Four and seven variables are used for axial stress and normal contact force, respectively. With these variables 28 (4×7= 28) numerical simulations are done.

Table 1. fretting fatigue primary varibales.

σaxial (MPa)	30	60	90	150	-	-	-
P (N)	5	50	300	600	900	1200	1500
Q (N)	18	18	18	18	18	18	18

Then MATLAB (MATLAB 7.12, 2011) code is used to post process the FE outputs for monitoring the interaction effect of primary variables on fretting fatigue slip amplitude. For this purpose, in each FE model maximum local slip amplitude at contact interface is extracted. Then, a surface is interpolated through these points at each axial stress and normal contact load.

6. Numerical results

In order to validate fretting fatigue FE model, stress distribution at contact interface is compared with the analytical solution (Hills and Nowell 1994) as explained in section 2.

Figure 6 shows the shear stress distribution at contact interface. As it can be seen with 5 µm mesh size at contact interface, a good correlation between numerical and analytical method can be achieved.
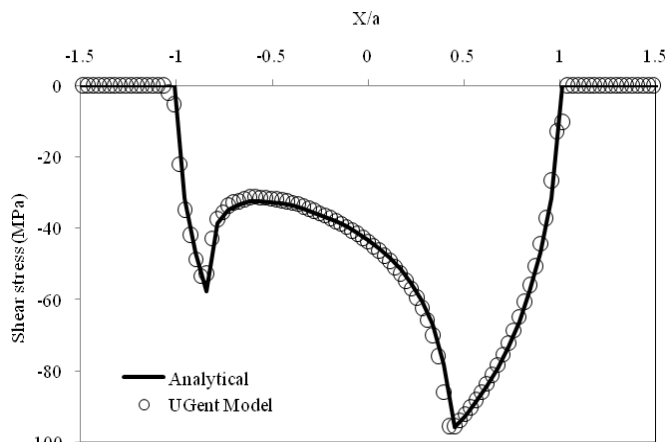
Figure 6. Shear stress distribution via normalized contact distance
(σ_{axial}= 90 MPa, P= 1200 N, a=177.9µm).

Figure 7 shows fretting slip distribution at half-contact interface between pad and specimen for different normal contact forces (σ_{axial}= 30 MPa). As it can be seen the slip amplitude near trailing edge reaches its maximum value and it is near to the side where axial stress is applied. It can be seen that the slip change does not follow a constant trend when normal contact force increases. Almost in all cases this behavior can be noted.
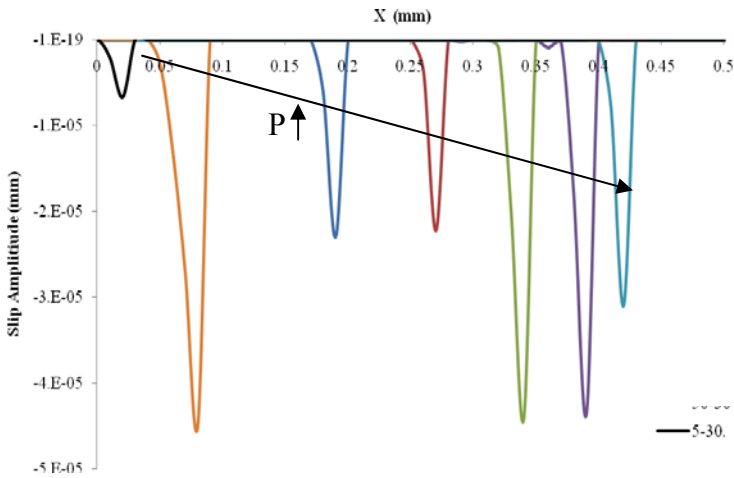
Figure 7. Fretting fatigue slip amplitude at half-contact interface
(σaxial= 30 Mpa, P= 5, 50, 300, 600, 900, 1200 and 1500 N)
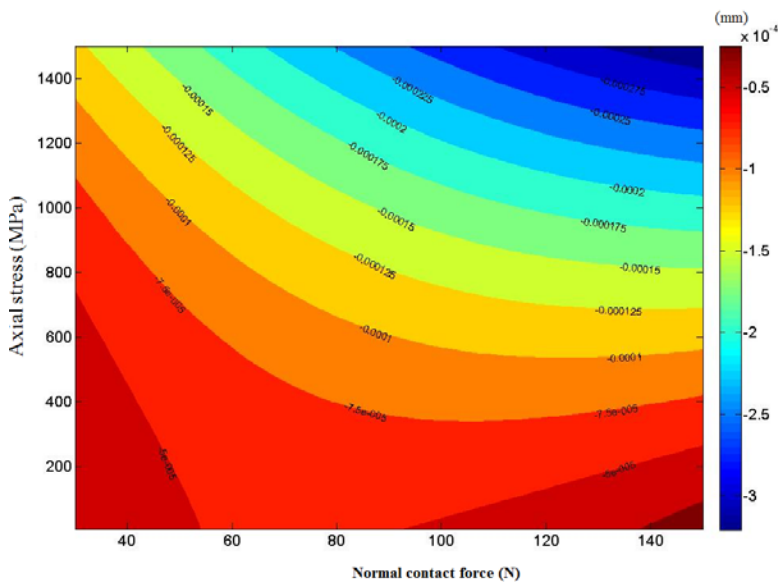
Figure 8. Fretting fatigue slip map

Figure 8 shows the effect of different normal contact force and axial stress and their interaction on slip amplitude. As it can be seen in this illustration that is called fretting fatigue slip map, it is possible to find the relevant local slip amplitude and the fretting fatigue parameter at which the partial slip occurs. So, based on the proposed FE methodology it is possible to renew the fretting map (Figure 4). It is also possible to extend the number of design variables to more than two and taking into account some other primary variables such as tangential force (Q), coefficient of friction (μ) or even different pad's geometries.

7. Conclusions

In this investigation a FE fretting fatigue model is introduced. Based on the FE model a parametric study is done in order to find the interaction effects of two primary variables; namely axial stress and normal contact force, on fretting fatigue slip amplitude. Also Numerical Design of Experiment (NDOE) method is used to post process the FE output data.

To conclude, a fretting fatigue slip map is proposed based on the FE model that can be used for monitoring the local slip amplitude and consequently, choosing right fretting fatigue parameters that are near to the practical applications.

Furthermore, it is possible to extend this method to investigate more about interaction effects of different primary and secondary variables of fretting fatigue on local slip amplitude, which play a significant role in fretting fatigue problem.

Acknowledgement

References

1. ABAQUS 6.10/ user manual (2011).

2. Cattaneo, C. (1938). "Sul Contatto di due corpi elastici: distribuzione locale degli sforzi." Rend Accad Naz Lincei

3. Dobromirski, J. M. (1992). Variables of fretting process - are there 50 of them. Standardization of fretting fatigue test methods and equipment. M. H. Attia and R. B. Waterhouse. Philadelphia, American Society of Testing and Materials.

4. Hills, D. A. and D. Nowell (1994). Mechanics of fretting fatigue, Kluwer Academic Publisher.

5. LabSpace (2011). http://labspace.open.ac.uk/mod/resource/view.php?id=391149

6. MATLAB 7.12/ user manual (2011).

7. Mindlin R.D. , D. H. (1953). "Elastic spheres in contact under varying oblique forces." Journal of applied mechanics.

8. Vingsbo, O. and S. Soderberg (1988). "On fretting maps." Wear.

Friction and wear properties of polyamides filled with molybdenum disulphide (MoS$_2$)

[1]Vanessa RODRIGUEZ, [1]Jacob SUKUMARAN,
[1]Patrick DE BAETS, [1]Wouter OST,
[1]Yeczain PEREZ DELGADO, [2]Mátyás ANDÓ

[1]Department of Mechanical Construction and Production, Ghent University

[2]Institute for Mechanical Engineering Technology,
Faculty of Mechanical Engineering, Szent István University

Abstract

Polyamides (PAs) form a major class of tribo-polymers used in various types of friction and wear situations, especially because they exhibit advanced mechanical properties and abrasive wear resistance. In this paper, the influence of fillers like molybdenum disulphide (MoS$_2$) and nanoparticles in polyamides describing friction and wear behaviour was investigated. Reciprocating wear experiments were performed in polyamide 6 (PA6) and polyamide 6.6 (PA6.6) against low carbon steel counter plates using a medium scale flat on flat tribotester. The polymer test specimens were slid at a constant velocity of 10 mm/s and contact pressure of 10 MPa was included. The experimental results demonstrates that the friction coefficient of PA6 increase with increasing the temperature caused by frictional heating. PA6.6 composite filled with molybdenum disulphide (MoS$_2$) has lower coefficient of friction on comparing with PA6 due to the addition of nanoparticles. The PA6.6 sliding against steel is found to be more sensitive than PA6 to stick-slip motion, which complicates the wear mechanisms involved.

Keywords

Polyamide 6 (PA6), Polyamide 6.6 (PA6.6), carbon fiber, MoS$_2$, friction and wear.

1. Introduction

Thermoplastics have replaced metals in many light duty load bearing applications because of their lightweight, economic fabrication and good chemical resistance. The increase in use of polymers is due to the low coefficient of friction when compared with metals because of low interfacial adhesion energy [1]. The mechanical strength and wear resistance of polymers largely determine the suitability of these materials for applications like gears, bearings, cams, etc.[2]. Furthermore polymer gears and bearings can accommodate shock loading, shaft misalignment and bending better than the metal parts. Polyamide (PA) and polyacetal (POM) are the widely used thermoplastic polymers for engineering applications.

PA is one of the major engineering high performance plastics used in dry running applications for their good balance in properties. Thanks to their crystalline structure they show an excellent mechanical properties and chemical resistance. In addition, these materials have very good flame retardant property and can be extruded, thermoformed, or molded. Both polyamide 6 (PA6) and polyamide 6.6 (PA6.6) are widely used in many different markets and applications due to their good performance. They are by far the most used polyamide globally. In the recent years there is an increase in the usage of PA in food, medical, and chemical packaging applications [1]. Over 100 different formulations are available in the production of PA film, but PA6 and PA6.6 with melting point of 215, and 264°C, is commonly found polymer in food packaging applications [3]. Although they PA6 and PA6.6 exhibit similar properties some slight differences remain were PA6.6 has the following advantages on comparing with PA6 with better hydrolytic stability, lower cost, better long term heat ageing, the PA6.6 at 1.8 MPa is 80-90°C. PA6.6 is used in high temperature applications. It provides good surface appearance and good weld strength leading to burst pressure resistance. The water absorption properties of polymer are important because of influence on mechanical, electrical and tribological properties. PA6.6 has a lower absorption percentage of 8.5%, where PA6 which has 9.5%. The relatively high absorption percentage in PA6 is due to the high ratio of amide group to the CH_2 group were the amide group has a greater water absorbing property.

Several research has already been performed on the tribological behaviour of PA and it was fairly satisfactory even at dry sliding and lubrication was considered necessary only at high speeds [4]. However, this paper is focused on the comparison of the friction coefficient and the wear rate of PA6 and PA6.6 in the medium-scale testing with the goal to improve the fundamental insight into the tribology of these materials and to further extend the scientific perception of the influence of reinforced composites. In the last years various fillers have been used to develop polymers composites for high wear resistance, for example, short fibers reinforcements, such as carbon, glass and aramid fibers have been successfully used to improve the strength and therefore the load carrying capacity of polymers composites. In the other hand, with solid lubricants, such as polytetrafluoethylene (PTFE), graphite and MoS_2 have proved to be generally helpful in reducing the coefficient of friction and consequently the wear rate. Nevertheless, all of those composites are used in polymer to increasingly applied as structural materials in the aerospace, automotive and chemical industries due to provide lower weight alternatives than metallic materials and a number of these applications are concentrated on tribological components, such as gears, cams, bearings and seals where the self-lubrication of polymers is of special advantages.

2. Materials and methods

Three different types of polymers with dimension of 30x30x30 mm^3 have been used in the current investigation, commercially available (Zell Metal, Austria).

PA6 (Zellamid 202XN) is reinforced by nanoparticles. PA6.6 (Zellamid 250) is one of the hardest and most rigid types of extruded nylon. And the last PA6.6 (Zellamid 250MO) filled with Molybdenum disulphide (MoS_2) having improved strength, rigidity and friction ratio (Table 1). Main characteristics of all the three polymers are high resistance to react with fuels, oil, greases, most organic solvents and alkalis.However, Zellamid 250 and Zellamid 250MO has low moisture absorption rate which ensures better dimensional stability. Before the test the samples are machined by milling, and the arithmetic mean roughness was found to be 3.5 µm.

Table 1. Properties of the polyamide PA6 and PA6.6

Property	Unit	Zellamid 202 XN	Zellamid 250	Zellamid 250 MO
Density	g/cm³	1.15	1.15	1.15
Tensile strength at break	MPa	93	80	80
Elongation at break	%	5	50	50
Modulus of elasticity in tension	MPa	4200	3200	3200
Hardness Shore, Scale D		80	80	80
Moisture absorption	%	3	2.8	–
HDT	°C	168	100	---
Melting Point Method A	°C	215	255	265

S235JR low carbon steel (1.0037, EN10025) plates were used as counter material for all experiments, with dimensions of 100mm x 200mm x 20mm. The chemical composition of the counter plates are summarized in Table 2. The surface finishing of counter plates was obtained by means of grinding. The surface roughness of the counter plates was measured before and after the tests using a Hommel Tester T1000 according to DIN EN ISO 4287 standard with an assessment length $l_t = 4.0$ mm and cut off $\lambda_c = 0.80$ mm. The resulting R_a roughness values before tests were found between 0.6 and 0.7µm.

Table 2. Chemical composition and properties of S235JR carbon steel.

Material	C[%]	Si[%]	Mn[%]	P[%]	S[%]	Cr[%]	Ni[%]
S235JR	0.22	0.35	1.10	0.05	0.05	0.3	0.3

3. Test-setup

The medium-scale tests were performed on a flat on flat setup a schematic view of the test rig is shown in the figure 1, the adaptability of testing of the

convenience to handle the system. Beside, the results can be extrapolated to large scale thus making the test more economical. The test bench is built on a fatigue rated load-frame with 200 kN capacity. Two steel counter-faces (2) are mounted (bolt connection) on a central sliding block (1). This central sliding block is connected to the actuator of the load frame. The sliding block moves in the vertical direction and slides against the two specimens (5) placed in holders (4). The maximum normal load which can be applied on the friction specimens is 225 KN. The test material (5) and the holders (4) are held in (vertical) position by the reaction fork (3). Wear of the friction material is compensated by horizontal movement of the holders (4) with respect to the reaction fork (3). The reaction fork is constructed in such fashion that it can also hold the test medium. The characteristics of the test rig and the test parameters are mentioned in Table 3.
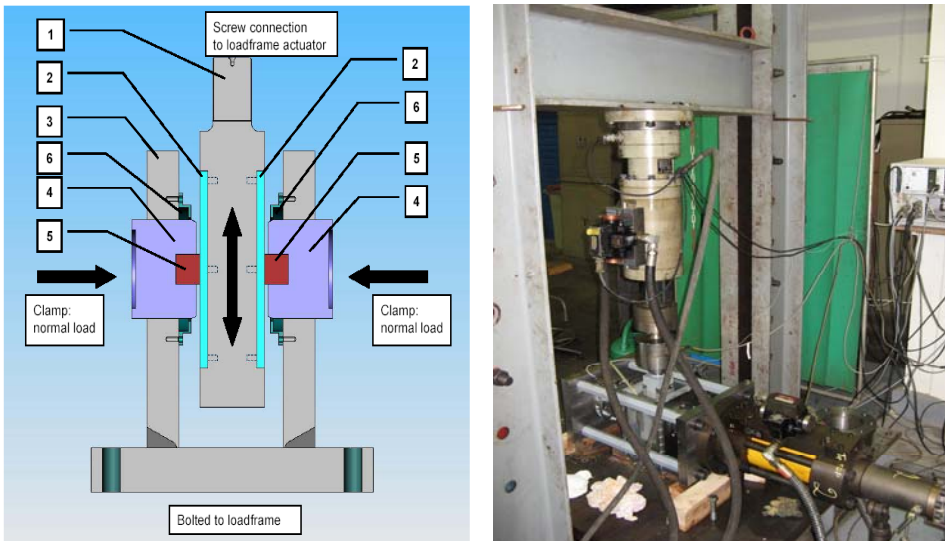
Figure 1. Medium-scale flat (MSF) tribotester

Table 3. Test parameters

Parameters	Units	Limits
Size of test material	[mm]	30 x 30 x 30
Size of counter (steel) material	[mm]	80 x 200 x 19
Maximum stroke	[mm]	100
Maximum normal load	[kN]	225
Maximum friction force	[kN]	200
Maximum frequency at maximum stroke	[Hz]	1

4. Test Procedure

Initially the moisture absorbed by the test specimen from the environment is removed by drying the specimen in an oven for 24 hours at a temperature of 70°C. The specimen was cooled in a controlled atmosphere before measuring the weight and the thickness. Flat polymer materials are slid against flat counter plates to simulate flat on flat condition. Visual inspections were made to ensure the parallelism between the counter plate and the specimen. The used sliding stroke was 10 mm, furthermore the running-in was done for 72 hours with a constant load and velocity at 9000N, 10mm/s respectively, 10 mm was the sliding stroke, Cooling is done in order to study the change in temperature during the initial period of contact which is normally high. After cooling for 4 hours the test was performed for two hours with the same load and velocity. A total of seven loops were done to identify the accuracy level of the test.

5. Calculation of the friction coefficient

For all the measured signals the scale factors and offsets were applied. The total friction force (F_{FR}) is measured by the force transducer. The coefficient of friction (μ) is calculated from the measured friction force (F_{FR}) and the normal force (F_N) according to equation 1, where in the factor of two is used because the friction force is the aggregate of the two friction specimens.

$$\mu = \frac{F_{FR}}{2 \cdot F_N} \qquad (1)$$

The values of friction force in the beginning of sliding will be considered for calculating the static coefficient of friction (μ_{stat}). The dynamic coefficient is the average the second half of the stroke (μ_{dyn}).

6. Results

Parameters like friction force, temperature, and displacement due to wear of material were recorded and the results are summed up for analysis.

The friction coefficient during the 72 hours test is shown in Figure 2(a).Considering the difference between the static and the dynamic friction all the three materials follow the same pattern having larger values for static friction comparing the dynamic friction Figure 2(b) shows the friction coefficient from 76 to 78 hours. The main purpose of running-in for 72 hours is to have a proper surface orientation on polymers to have an error free result. Moreover, the specimen is allowed to cool for four hours from 72 hours until 76 hours. A difference in the range between the running-in period and the test period is

observed. During the running-in period the friction force between a thermoplastic and the steel surface aligns.
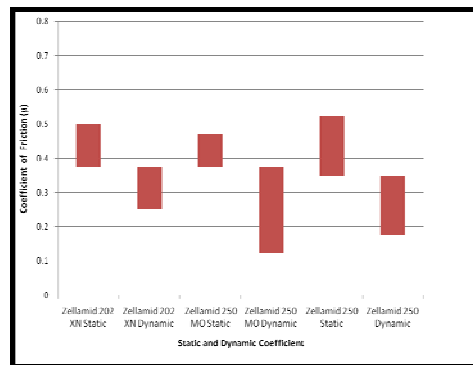
(a)
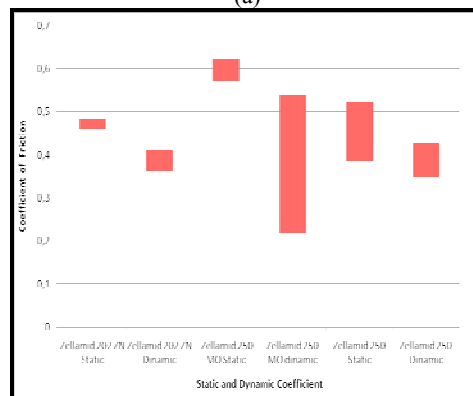
(b)

Figure 2. Illustrates the range of friction coefficient between
all three materials (a) 0 – 72 hours (b) 76 – 78 hours.

The figure 3(a) and (b) shows the friction curves for the running in period for all three test material from 0 to 72 hours. The curve for friction coefficient was made as function of sliding distance (h) where a constant load and sliding velocity of 9000N, 10 mm/sand sliding stroke 10 mm is maintained. Both the static and dynamic friction shows similar behaviour with respect to the sliding distance or sliding time (h). It worth to note that the tendency of the friction coefficient curves is similar in both, forward and reverse directions considering the absolute values. Figure 3(a) shows the friction curves for all three materials during the running in period where the friction coefficient increases dramatically during the initial stage from 0 to 20 hours and then follows a steady pattern until 72 hours. The dynamic friction coefficients among the three materials during two hours from 76 to 78 hours is shown in figure 3 (b) and it clear the friction coefficient is relatively lower in Zellamid 250MO when compared with the other two materials. Both materials Zellamid 250 and Zellamid 202 XN have a similar

trend in the friction curves. Moreover, Zellamid 202 XN produces has high friction coefficient on comparing with other two polymers.
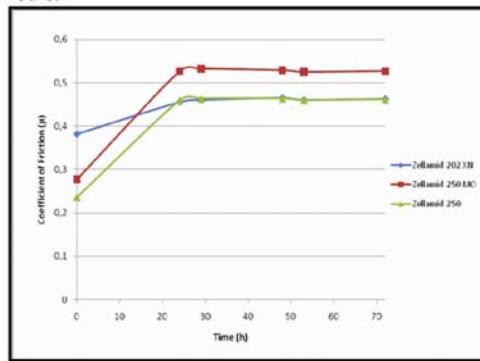
(a)
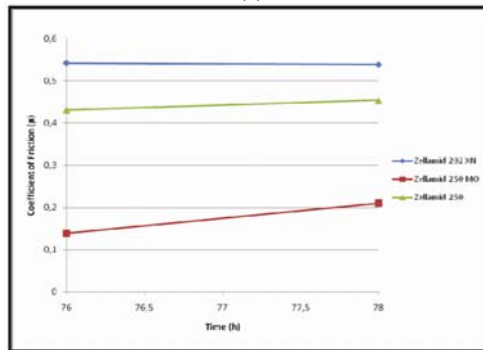
(b)

Figure 3. Coefficient of friction Vs. Displacement during running-in: steel – PA 6.6
(Zellamid 250 MO); s= 64 mm; P= 11-10 MPa; velocity= 10 mm/s for
(a) Running –in 0-72 hrs (b) Test period 76-78 hrs
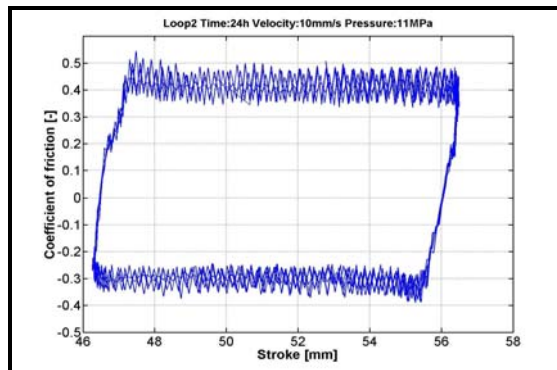
Figure 4. Friction Force vs. Tangential displacement after every standstill,
steel-PA6 (Zellamid 202XN), P=11MPa, v=10mm/s, cycle 1.
Show stick-slip effect during the initial period from 46.6 mm
to 47.05 mm the stroke.

7. Influence of temperature

It is evident from Figure 5 (a) and (b) that for all the three materials the temperature increases to a specific limit initially and reaches a steady state where the temperature remains constant. During the running-in phase, the temperature of the specimens increases above 80˚C as shown in the Figure 5 (a). The temperature of contacts surface increases with sliding distance due to the frictional heat developed during sliding. Figure 5(b) shows the increase in temperature with respect to the sliding distance from 76 to 78 hours and in all the three materials it was found to be linear. The friction and wear behaviours might also depend on the temperature rise of apparatus used. Among all three samples Zellamid 250 MO has the lowest effect of temperature during the test.
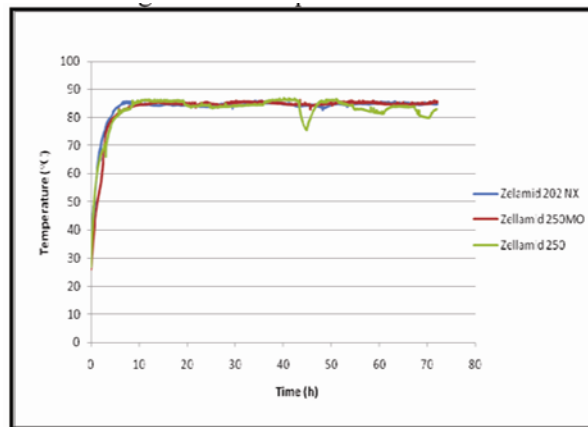
(a)
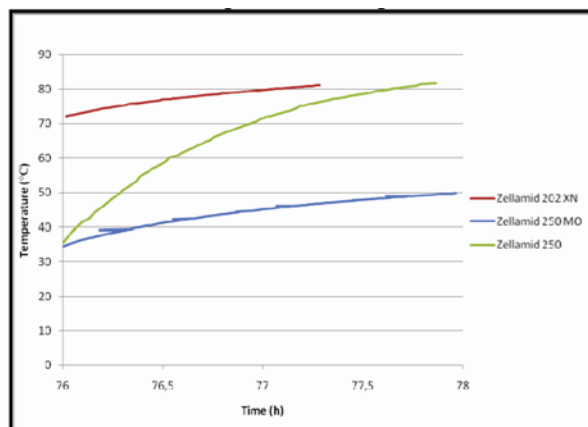
(b)

Figure 5. Temperature of Zellamid 202XN, Zellamid 250 MO and Zellamid 250, (a) From 0-72 hours, (b) From hour 76-78.

8. Wear rate of the polymers used in testing

The total thickness reduction of the three different polymers blocks during the tests at a constant load and velocity is shown in the Figure 6. The total thickness reduction results from the combined action of the following mechanisms: elastic and plastic deformation, thermal expansion and wear (material loss). In order to distinguish real wear (material loss) from deformation, the weight loss of the test material was also measured and thus the wear was calculated. One sample was tested to compare the results for analysing the accuracy level of the experiment. It is clearly seen in Figure 6 Zellamid 250 and Zellamid 202 XN has the highest wear when compared with Zellamid 250 MO. The actual wear (material loss) of the plastic blocks is caused by abrasion, which could be expected for such rough counter plates. No material transfers due to adhesion of the plastic material to the steel counter surfaces were observed. And wear debris on the sides of the wear track gives possible evidence for abrasion.
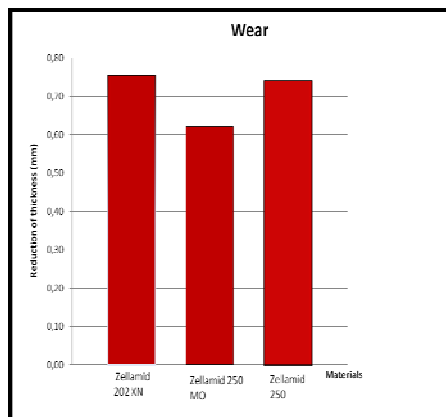
(a)
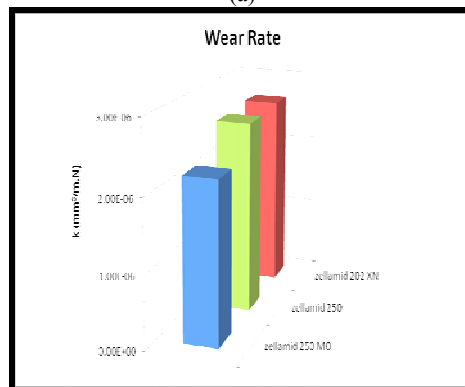
(a)

Figure 6. (a) Illustrates the wear rate of the three materials (Zellamid 250 XN, Zellamid 250 MO, Zellamid 250 from 76 to 78 hours, (b) Wear (material loss).

9. Discussion

The main objective of the current research is to investigate in the friction and wear behavior of the PA6 and PA6.6 which could be used in bearing applications. The friction and wear behaviour of polymeric matrix materials can be improved by having a lower surface tension and high stiffness which is obtained quite successfully by using reinforced or filled with nanoparticles to the polymers. Internal lubricants such as PTFE or graphite are frequently incorporated to the polymers to reduce adhesion. Additives like short aramids, carbon, or glass fibers are used to increase stiffness, strength, impact resistance, thermal conductivity, and creep resistance of the polymers. With a blend of high-performance polymer matrix, internal lubricants and fibrous reinforcement, excellent friction and wear properties can be achieved in composites. In our case additives like nanoparticles and molybdenum is added and the effect of these additives is clearly seen from the results were the friction behaviour of the material changes corresponding to the additives.

Previous research has been conducted with different speeds and it was found that friction coefficient at of nylon reaches a maximum of 1.0-2.0 only higher speeds[5]. The friction coefficient increases rapidly until 20 hours, on comparing the increase in temperature were the relationship between temperature and the friction coefficient is linearly dependent on each other. Two mechanisms controls the friction force F between a thermoplastic and steel: adhesion and deformation of the plastic [6] were adhesion occurs as product of the real contact area and the shear strength of the plastic material. An increase in glass transition temperature (which equals 40-50 °C for PA 6) leads to a gradual decrease in the elasticity modulus E which dominates the deformation mechanism. The difference in the friction curves during the forward and the reverse stroke is possibly due to the asperity interactions were breaking and regeneration of micro junctions. The asperities are broken down during the forward traverse causing a increased value in friction coefficient relative to the reverse stroke were new asperities are formed during the reverse stroke. Moreover, this is explained as the result of frictional heating which increases the temperature of the contact surface, leading to relaxation of polymer molecule chains [7]. Some variations are observed in the friction coefficient are possibly due the critical surface energy of the polymer

In others investigations it was found that for line and point contacts, the flash temperatures at running-in are at maximum due to the high contact pressure in the initial stage [8] this is due to the intensity of heat to a confined area is relatively small on comparing with flat on flat test configuration, this phenomenon is eliminated. It was evident that temperature played a vital role in the material behaviour, for example in all three material from 76 to 78 hours showed a behavior correlating the raise in temperature were the friction coefficient decreases with the increase in temperature. However, considering all the three polymers, the highest temperature was observed in Zellamid 202 XN (PA) which is due to the material property with respect to the strength by

softening were the mobility of the chains increases as they become less rigid. Nevertheless, this higher mobility also makes it easier to remove wear debris from the bulk specimen. Melting can also occur because of the higher temperatures and plastic deformation is more at higher loads. Both effects contribute to a severe wear regime for PA6.

For apparent contact pressure which is sufficiently low to neglect the interaction of the individual contact spots between rough surfaces, the real contact area or the indentation of the hard asperities into the softer material is proportional to the normal load for both elastic and plastic deformation. Such a situation results in a friction coefficient independent of the normal load where the softer material has a constant shear. In our case the load is of the range in between large scale and the medium scale testing causing plastic deformation as a dominant mechanism. As PA6 is a thermoplastic, it deforms more easily at interactions with the harder steel roughness asperities of the mating surface when its temperature is higher. Consequently, at higher temperatures the roughness asperities of the steel counter surface plough through the PA, rather than normal separation of the rubbing surfaces due to the forced tangential motion from the inclinations of roughness peaks over one another (asperity interlocking). The normal vibration caused by asperity interlocking lead to a reduction in the friction force at higher velocities. Figure 5 shows that the mean coefficient of friction during stick-slip is lower than during smooth sliding. During stick-slip serious vibrations of the entire test rig were observed. From the literature, it is known that both normal and tangential vibrations lead to a reduction in the friction force [9, 10]. Therefore, it is well known that for abrasive wear processes the surface roughness especially that of the hardest surface, is extremely important. The higher the surface roughness of the hard surface, the higher the ploughing and abrasive wear. The friction coefficients of thermoplastic polymers PA6.6, PA6 first decrease with increasing surface roughness of the steel counter plate and reach minimum values at R_a about 0.2-0.5µm. With further increasing roughness the friction coefficient increases. The explanation for this behavior in the literature [11] is that, for small values of the surface roughness, adhesion forces are the dominating factor, whereas for higher surface roughness, abrasive processes prevail. The literature supports the finding that abrasive wear of polymers increases considerably with growing surface roughness of the steel mating plate [8].

The influence of particles size plays an important role of the wear resistance was due to either mechanical (the enhanced modulus and hardness practically) or chemical (the improved bonding between transfer films and metallic counterparts) reasons similar effects were observed by Wang et al [12] where the effect of Molybdenum disulphide (MO) additives and nanoparticles in PA 6.6 was investigated recently where PA with MO particles do not have a favorable result but when blended with carbon fibers shows significant improvement in wear resistance of PA 6.6 and higher coefficient of friction. The research work done by Pettarin et al [13] also showed same results of having increased wear

resistance by adding molybdenum disulphide is contributed through the heating effects. It was also observed in our case that the Zellamid 250 MO has the lowest temperature relative to the other two materials where MoS_2 helps in the dissipation of generated heat during friction and thus having high wear resistance.

10. Conclusions

Systematic flat on flat wear experiments at medium-scale on three polyamides: Zellamid 202XN, Zellamid 250 MO and Zellamid 250, in reciprocating sliding contact with low carbon steel counter plates under normal load of 9000N and sliding velocity of 10 mm/s revealed that tribological properties are affected by chemical composition, mechanical properties of the thermoplastic, service temperature as well as reinforcement by means of nanoparticles. PA 6.6 (Zellamid 250) sliding against steel is sensitive to stick-lip motion and favorable behaviour in friction and wear was observed in the PA6.6 with Molybednum disulphide additives. The highest friction coefficient and wear level was encountered with Zellamid 250 the PA6 without any additives. The molybdenum disulphide additives influence the material to have high wear resistance and low co-efficient of friction.

11. Acknowledgments

References

1 .Czichos, H., et al., Advances in tribology: the materials point of view. Wear, 1995. 190(2): p. 155-161.

2. Thorp, J.M., friction of some commercial polymer-based bearing materials against steel. Tribology International, 1982. 15(2): p. 69-74.

3. Soto-Valdez, H. and J.W. Gramshaw, Cyclopentanone and cyclopentanone derivatives as degradation products of polyamide 6,6. Journal of Materials Science Letters, 2000. 19(10): p. 823-825.

4. Srinath, G. and R. Gnanamoorthy, Effect of short fibre reinforcement on the friction and wear behaviour of Nylon 66. Applied Composite Materials, 2005. 12(6): p. 369-383.

5. Watanabe, M., M. Karasawa, and Matsubar.K, frictional properties of nylon. Wear, 1968. 12(3): p. 185-&.

6. Y.Yamaguchi, Tribology of plastics materials Tribology series Vol. 16. 1990: Elseiver.

7. Unal, H. and A. Mimaroglu, Friction and wear behaviour of unfilled engineering thermoplastics. Materials & Design, 2003. 24(3): p. 183-187.

8. Van de Velde, F. and P. De Baets, The friction and wear behaviour of polyamide 6 sliding against steel at low velocity under very high contact pressures. Wear, 1997. 209(1-2): p. 106-114.

9. Tolstoi, D.M., Significance of the normal degree of freedom and natural normal vibrations in contact friction. Wear. 10(3): p. 199-213.

10. Lenkiewicz, W., The sliding friction process--effect of external vibrations. Wear, 1969. 13(2): p. 99-108.

11. Lancaster, J.K., Dry bearings: a survey of materials and factors affecting their performance. Tribology, 1973. 6(6): p. 219-251.

12. Wang, J., et al., Investigation of the influence of MoS2 filler on the tribological properties of carbon fiber reinforced nylon 1010 composites. Wear. 255(1-6): p. 774-779.

13. Pettarin, V., et al., Changes in tribological performance of high molecular weight high density polyethylene induced by the addition of molybdenum disulphide particles. Wear. 269(1-2): p. 31-45.

Analytical validation of crack driving force calculations for defects in plates and pipes under tension

Stijn HERTELÉ, Wim DE WAELE, Rudi DENYS,
Matthias VERSTRAETE

[1]Department of Mechanical Construction and Production,
Laboratory Soete, Ghent University

Abstract

Large scale tension testing of defected girth welds is an essential tool to identify the possible structural failure of a plastically deformed pipeline due to girth weld defects. To enable a profound interpretation of the influences of all parameters and their interactions, the authors have developed a parametric finite element model which describes such large scale tension tests. This paper compares calculated values of crack driving force with an extensive set of existing analytical relations for two simplified geometries created by the model: flat plates and pipes. For all considered cases, excellent agreements are achieved with published literature. Hence, this analytical validation allows to conclude that the finite element model can be used with confidence to calculate crack driving force in large scale tension tests of defected girth welds.

Keywords

1. Introduction

The growing energy demand urges fossil fuel suppliers to install and operate fuel transmission pipelines in increasingly hostile environments. Some of these environments may impose a plastic deformation to the pipeline (e.g. due to land slides). The girth welds that connect different pipes have a high likelihood of defects (e.g. cracks, slag inclusions, lack of fusion) and are critical in terms of structural integrity when loaded in tension. Consequently, girth weld testing is an essential tool for the qualification of pipe and weld design.

Two types of large scale girth weld tension tests are commonly used: the curved wide plate tension (CWP) test and the full scale pipe tension (FSP) test. First, a CWP test can be described as a tensile test on an unflattened sample of a pipeline which traverses the girth weld. Second, a FSP test includes a full scale pipe section containing the entire girth weld. Whereas a FSP specimen can be geometrically described by its length $2L$, mean pipe diameter D and wall thickness t, a CWP specimen is additionally characterized by its width $2W$. For

both a CWP and a FSP test, the girth weld is deliberately notched along the circumferential direction aiming to represent a part-through weld surface defect.

To gain a better understanding in the outcome of a CWP or FSP test result, the authors have developed a parametric script that produces finite element models which can describe both tests. Essential for this model is a correct calculation of the relation between remotely applied conditions and crack driving force. To validate this calculation, this paper elaborates a comparison of calculated crack driving force results with solutions available in literature for simplified geometries.

Section 2 gives an overview of available analytical solutions for validation. Then, Section 3 gives a brief summary of the finite element model. Next, Section 4 discusses the validation. Conclusions are finally drawn in Section 5.

2. Existing analytical equations for validation

Basic principles of fracture mechanics
All considered analytical equations for validation are based upon fracture mechanics. This research field can generally be divided into two approaches, each based upon different assumptions: linear-elastic fracture mechanics (LEFM) and elastic-plastic fracture mechanics (EPFM).

First, LEFM assumes a purely linear-elastic material behaviour defined by Young's modulus E (MPa) and the Poisson ratio ν. Assuming a tensile loaded crack, crack driving force is described by a stress intensity factor K_I (MPa.mm$^{1/2}$), generally expressed as follows:

$$K_I = Y\sigma_m \sqrt{\pi a} \tag{1}$$

with σ_m the remotely applied stress (MPa), a the crack depth (mm) and Y a dimensionless scaling factor. Y depends on the geometry, the defect size and the investigated position on the crack tip front. Second, EPFM includes the effect of advanced crack tip plasticity. Compared to LEFM, it has a wider application range but is more challenging to perform. The current study deals with the frequently applied J-integral, which is a measure for crack driving force in EPFM. J is the sum of a linear-elastic component J_{el} and a plastic component J_{pl}. On the one hand, J_{el} is theoretically related to K_I as follows:

$$J_{el} = K_I^2 / E' \tag{2}$$

where E' is E under plane stress conditions and $E/(1 - \nu^2)$ under plane strain conditions. For applied stresses well below the yield stress, J merely consists of the linear-elastic component J_{el}. Hence, focusing on those stresses, Eq. (2) can be used to calculate K_I.

J_{pl}, on the other hand, can be expressed as proposed in the EPRI handbook [Kumar et al., 1981]:

$$J_{pl} = \alpha \varepsilon_0 \sigma_0 t h_1 \left(\frac{\sigma_m}{\sigma_0} \right)^{n+1} \tag{3}$$

where *t* is the thickness of the structure and ε_0 (yield strain = σ_0/E), σ_0 (yield strength), α (yield offset) and *n* (strain hardening exponent) are four parameters which define the material's true stress-true strain (σ-ε) behaviour assuming a Ramberg-Osgood [Ramberg et al., 1943] relation:

$$\frac{\varepsilon}{\varepsilon_0} = \frac{\sigma}{\sigma_0} + \alpha \left(\frac{\sigma}{\sigma_0} \right)^n \tag{4}$$

J_{pl} is proportional to a dimensionless factor h_1, which depends on the geometry of the structure, the crack dimensions, the material behaviour (more specifically, the strain hardening exponent *n*) and the considered position on the crack tip front. In literature, solutions for J_{pl} are often provided on the basis of tabulated h_1-factors, which have been obtained from finite element analyses. Using Eq. (4), Eq. (3) can be converted into an alternative expression which indicates the influence of both the remotely applied stress σ_m and the remotely applied plastic strain $\varepsilon_{m,pl}$:

$$J_{pl} = h_1 t \sigma_m \varepsilon_{m,pl} \tag{5}$$

In Eq. (5), $\varepsilon_{m,pl}$ is the plastic (power-law) component of the remotely applied strain ε_m, related to σ_m through Eq. (4).

Since the investigated application involves remote plasticity, the presented validation will cover EPFM calculations. Applying Eq. (2) for stresses way below yielding (where $J \approx J_{el}$) additionally allows for an LEFM validation.

Solutions for validation of a CWP simulation
To the authors' knowledge, crack driving force equations for curved plates with a surface crack are currently inexistent. Therefore, the validation of the CWP model has been simplified to flat plates, which are extensively described in literature. In addition, the validation assumes plain plates without weld.

For the LEFM calculation of K_I in surface-cracked flat plates, the closed-form Newman-Raju equation [Newman et al., 1984] is universally accepted and will therefore be applied in this paper. For the EPFM calculation of *J* over the entire crack front, a closed-form equation does not exist. Nevertheless, several authors have summarized discrete h_1-solutions in a tabulated form. In this paper, finite element results will be compared to h_1-values tabulated in four different studies: [Yagawa et al., 1993], [McClung et al., 1999], [Lei, 2004], and [Wang, 2006]. All abovementioned studies provide solutions for all positions on the crack tip front, characterized by a crack tip angle ϕ (Figure 1).
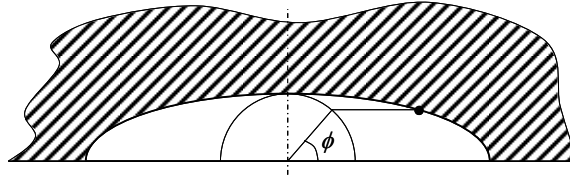
Figure 1. Definition of crack tip position ϕ.

Solutions for validation of a FSP simulation

A literature survey indicated that the availability and completeness of existing full pipe solutions is rather limited. In fact, no solutions were found which cover all possible positions on the crack tip front. Nevertheless, [Miura et al., 2008] found that, if $D/t \geq 21$ and $a/t \leq 0.6$, the stress intensity factor K_I for a circumferential defect in a pipe with diameter D and thickness t is comparable to that of an equal defect in a flat plate with width πD and thickness t. Adopting this agreement and assuming that a similar statement can be made for J, the solutions pointed out in Section 2.2 will be used for validation of FSP simulations.

3. Parametric finite element model

An in-house developed Python script communicates with the finite element software package ABAQUS®. Depending on a user-defined option, it creates finite element (FE) models that represent either CWP specimens or FSP specimens. The created models consist of one half of a specimen, assuming transversal symmetry. This involves that only one half of a crack is modelled, the crack tip angle ϕ varying between 0 and $\pi/2$. A full technical description of the structure of the script and the produced finite element models is beyond the scope of this paper. For a more detailed description and parametric studies, the reader is referred to [Hertelé et al., 2011]. For the simulations performed in the current study, it suffices to note that:

- mesh density was chosen fine enough to generate accurate results as indicated by a previously performed mesh convergence study.
- the defect tip was surrounded by a fine spider-web mesh, which facilitates accurate calculations of J.
- a material that hardens according to the Ramberg-Osgood model (Eq. (4)) has been assumed. This enables the calculation of h_1 through Eq. (5). In accordance with all considered literature, small strain isotropic hardening has been used in combination with the Von Mises yield criterion.

4. Analytical validation

Considered geometries and material

Two geometries were considered: a flat plate and a full pipe (Figure 2). Geometrical characteristics are summarized in Table 1. The investigated

geometries were long enough to eliminate possible unwanted effects of the boundary conditions at the end planes, enabling an extraction of remotely applied conditions in a cross section with uniform stress (σ_m) and strain (ε_m). Aiming at remote strains up to roughly 0.05, the end plane displacement was set to 5% of the total specimen length.

The material was assumed to harden with a strain hardening exponent $n = 10$. This value has been chosen for since it is included in all abovementioned tabulated solutions for h_1, enabling a comparison with published literature.

Thickness, crack dimensions and material definitions are equal for both plate and pipe. From the assumption made in [Miura et al., 2008] as discussed in Section 2.3, both specimens should hence yield similar values for K_I (and, hypothetically, J) for equal remote conditions and an equal crack tip position (note that $D/t = 21$ and $a/t < 0.6$).
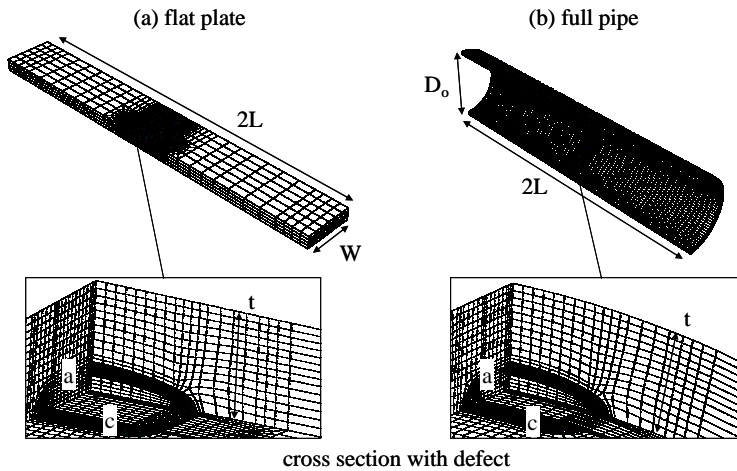
Figure 2. Mesh of the considered geometries

Table 1. Geometrical characteristics of the considered geometries

Specimen	Length 2L (mm)	Width 2W (mm)	Mean diameter D (mm)	Thickness t (mm)	Crack length 2c (mm)	Crack depth a (mm)
Flat plate	480	120	–	15	30	3
Full pipe	1320	–	315	15	30	3

Validation of K_I (LEFM)

The extraction of K_I starts from the assumption that $J \approx J_{el}$ (or $J_{pl} \approx 0$) for stresses well below yielding ($\sigma_m << \sigma_0$). As can be seen in Figure 3 this assumption is valid. Indeed, J is proportional to σ_m^2 for small linear-elastic stresses, which is theoretically the case for J_{el} as follows from Eqs. (1) and (2).

Figure 3. *J* equals J_{el} for stress levels up to roughly $\sigma/\sigma_0 = 0.6$
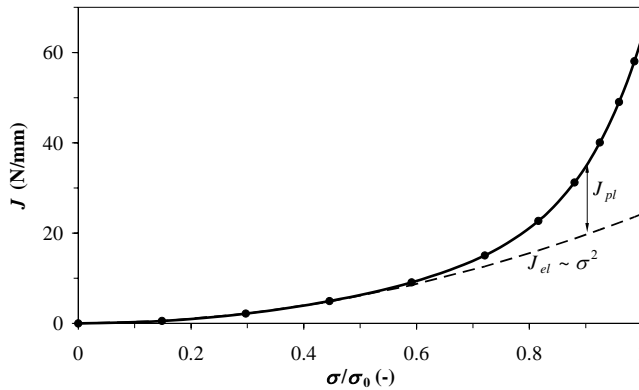(*J* response for full pipe at $\phi = \pi/2$).

Starting from the J_{el}-values as calculated in Figure 3 and assuming plane strain conditions ($E' = E/(1 - \nu^2)$), Figure 4 shows the comparison of the obtained K_I-values (normalized against σ_m) with the Newman-Raju equation for both plate and pipe. The following observations can be made:

– the K_I-values calculated by the finite element model are in close agreement with those predicted by the Newman-Raju equation. The best agreement is found near the deepest point of the crack ($\phi = \pi/2$). For long, shallow defects (as mostly the case in pipeline girth welds), this crack front area is of the highest interest since it shows the largest K_I-values.

– as stated in [Miura et al., 2008], the K_I-values for the pipe approach those for a flat plate with the same crack dimensions.

It can be concluded that the FE model can serve as a tool to calculate K_I-values and, hence, allows to perform a linear-elastic fracture mechanics analysis.
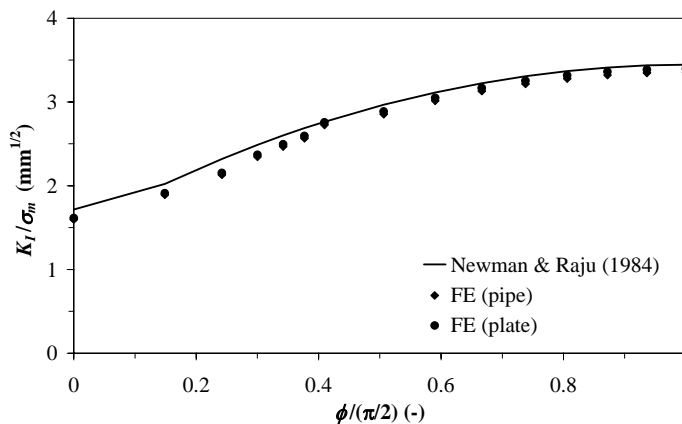

Figure 4. The obtained K_I-values are in close agreement with the equation of Newman & Raju.

Validation of J_{pl} (EPFM)

Subtracting J_{el} (obtained as in Figure 3) from J, J_{pl} is obtained and h_1-factors are calculated (Eq. (5)). Figure 5 shows the comparison with previously published h_1-factors, valid for both considered geometries. The following is observed:

- The calculated h_1-factors closely agree with literature and are within the scatter band created by the different published results.
- In contrast with the K_I-values, there is a greater divergence between the h_1-factors of the flat plate and those of the pipe. Hence, the statement made in [Miura et al., 2008] for LEFM cannot be fully extrapolated to EPFM. Nevertheless, it can serve as a rough estimation if a limited accuracy suffices for the investigated problem.

Figure 5 indicates that the FE model, next to LEFM, also gives representative results in an EPFM analysis.
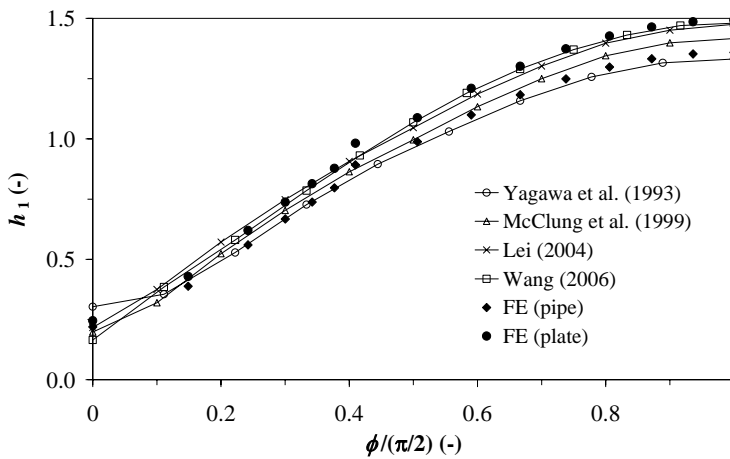
Figure 5. The obtained h_1-factors are in close agreement with previously
published literature.

5. Conclusions

For simplified cases of a flat plate and a full pipe without weld, the following major observations have been made:

1. Compared with existing literature, the finite element model predicts representative values of the stress intensity factor K_I assuming linear-elastic conditions.
2. Calculations of the plastic component of J-integral, J_{pl}, agree with a wide variety of previously published results.
3. Under certain geometrical conditions, K_I-values for a defect in a full pipe can be calculated by simplifying the geometry to a flat plate. A similar statement for J is to be dealt with care, as this simplification might result in a loss of accuracy.

Assuming that the abovementioned observations can be extrapolated to the more sophisticated cases of a curved wide plate with weld or a full scale pipe with weld, this study allows to conclude that the finite element model can be used with confidence to calculate crack driving force values in large scale tension tests of girth welds containing a defect.

Acknowledgement

References

1. Hertelé, S., et al. (2011): Sensitivity of plastic response of defective pipeline girth welds to the stress-strain behavior of base and weld metal. Proc. 30th Int. Conf. Ocean, Offshore and Arctic Eng., OMAE2011-49239, Rotterdam, the Netherlands.

2. Kumar, V., et al. (1981): An engineering approach for elastic-plastic fracture analysis. EPRI Report NP 1931.

3. McClung, R.C., et al. (1999): Development of a practical methodology for elastic-plastic and fully plastic fatigue crack growth. NASA/CR-1999-209428, NASA.

4. Lei, Y. (2004): J-integral and limit load analysis of semi-elliptical surface cracks in plates under tension. Int. J. Press. Vess. Piping, 81, 21-30.

5. Miura, N., et al. (2008): Comparison of stress intensity factor solutions for cylinders with axial and circumferential cracks. Nuclear Eng. Design, 238, 423-434.

6. Newman, J. C., et al. (1984): Stress-intensity factor equations for cracks in three-dimensional finite bodies subjected to tension and bending loads. NASA Technical Memorandum 85793, NASA.

7. Ramberg, W., et al. (1943): Description of stress-strain curves by three parameters, NACA Technical note 902.

8. Wang, X. (2006): Fully plastic J-integral solutions for surface cracked plates under biaxial loading. Eng. Fract. Mech., 73, 1581-1595.

9. Yagawa, G., et al. (1993): Three-dimensional fully plastic solutions for semielliptic surface cracks. Int. J. Press. Vess. Piping, 53, 457-510.

Numerical modelling and experimental validation of a threaded pipe connection under axial tension

Jeroen VAN WITTENBERGHE, Timothy GALLE,
Patrick DE BAETS, Wim DE WAELE

Department of Mechanical Construction and Production,
Laboratory Soete, Ghent University

Abstract

In order to improve a threaded pipe connection's fatigue life, accurate knowledge is necessary of the acting stresses and strains while subjected to external loads. In this study the stress distribution over an API Line Pipe threaded connection subjected to an axial load is studied using a 2D axisymmetric finite element model. It is shown that a non-uniform load distribution over the different threads causes a high stress concentration factor at the last engaged thread of the male part of the connection. The simulated results are compared to strain gauges measurements obtained during a quasi-static axial tensile test on a 4.5" API Line Pipe connection. A good correspondence is found between the two data sets, which proves the validity of the 2D axisymmetric model. Following the quasi-static tensile test, a fatigue test is carried out on the sample in the same test setup. A fatigue crack initiated at the root of the LET thread of the male part of the connection, which is the location where the highest stress concentration appears in the simulations..

Keywords

threaded pipe connection, pipeline, experiment, finite element model

1. Introduction

Threaded pipe connections are used in the oil and gas industry to connect pipelines in risers, drillstrings and casing strings. They consist of a male and a female part called respectively 'pin' and 'box'. To maintain a sealed and secure connection under external variable loads, threaded connections are generally preloaded. The assembly of the connections is referred to as 'make-up'. The combination of the make-up torque together with external loads and the geometry of the threads results in a complex stress distribution over the connection. Local stress concentrations at the thread roots can initiate fatigue cracks, in time causing the connection to fail. According to Griffin et al. (2004) the highest stress concentration under axial load can be expected at the last engaged thread (LET) of the pin.

In this study the stress distribution over an API Line Pipe threaded connection subjected to an axial load is studied using a 2D axisymmetric finite element model. As a validation, the simulated results are compared to strain gauges measurements obtained during an axial tensile test. Afterwards, a fatigue test is carried out on the same sample.

2. Finite element model

To simulate the threaded connections a 2D axisymmetric model is used. This is common practice when modelling threaded connections (cfr. Assanelli et al. 1997) since the reduced calculation time compared to full 3D models. Detailed information on the used finite element model can be found in the article by Van Wittenberghe et al. (2010).

The finite element analysis is performed in two consecutive steps. During the first step the make-up of the connection is simulated. Since a 2D axisymmetric model is used, this can not be done by rotating the pin into the box with a certain number of make-up turns as is done with a real connection. Instead, a radial overlap is applied, corresponding to the specified number of make-up turns and the thread surfaces are brought into contact. From the resulting von Mises equivalent stress distribution in Fig. 1a it can be seen that the stresses in the pin are very high and even exceed the material's yield strength. This is mainly caused by high compressive hoop stresses. The stresses in the box remain much lower than in the pin, since this is the more rigid part.

During the second step of the analysis an additional axial tensile stress is applied. The resulting von Mises stress distribution for an external axial tensile stress of 150 MPa is presented in Fig. 1b. The highest stress concentration appears at the root of the LET of the pin (indicated by the arrow). This corresponds to the earlier obtained results by Griffin et al. (2004) and as will be shown later, this location is also susceptible to fatigue crack initiation.
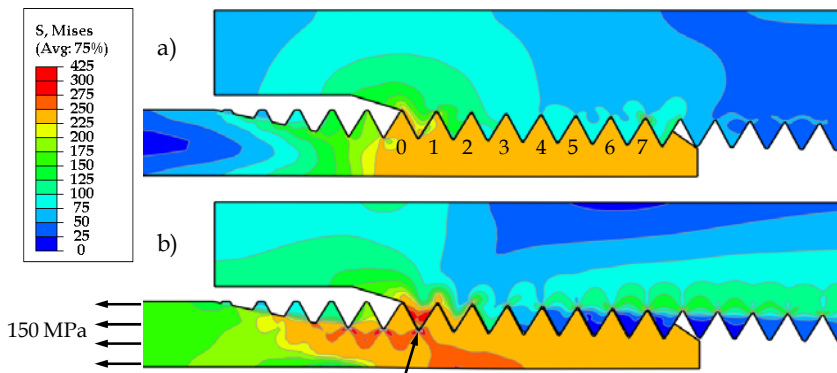

Figure 1. Von Mises stress distribution in: (a) a preloaded threaded connection and (b) a preloaded connection with an additional tensile stress.

The high stress concentration at the LET of the pin is the consequence of an uneven load distribution over the engaged threads of the connection. This load distribution as a percentage of the total load carried by the connection is given in Fig. 2. The threads are numbered as shown in Fig. 1a. Thread nr. 1 is the so-called 'last engaged thread' or LET of the pin and carries 36% of the total load. This is a highly undesirable situation. When trying to improve the performance of a threaded connection, one should try to obtain a more uniform load distribution over the threads and hence have a lower load and stress intensity factor at the LET.
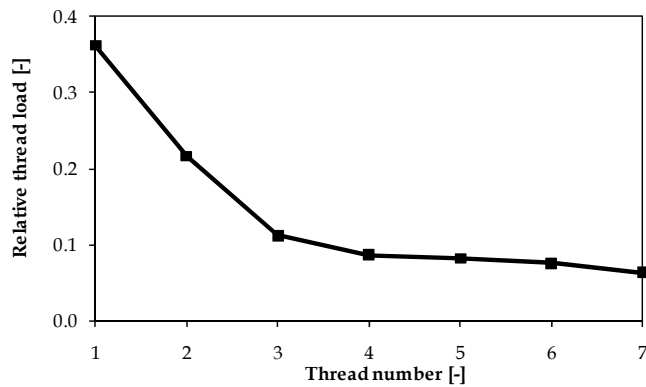

Figure 2. Thread load distribution (thread numbering according to Fig. 1).

3. Axial tensile validation test

To validate the simulation, an experimental axial tension test is carried out on a 4.5" API Line Pipe specimen of Grade B steel in the 1000 kN universal testing machine shown in Fig. 3. The specimen consisting of the pin (1a) made up in the box (1b) is placed vertically in the test rig. To compensate for any misalignment errors, the sample is connected to two ball joints (2) at the top and bottom. The upper ball joint is connected to the load cell (3) that measures the load applied by the vertical hydraulic actuator (4). During the test an axial tensile load is gradually applied and the appearing strains are continuously logged by several strain gauges.

Following the quasistatic axial tensile test a dynamic fatigue test is carried out in the same setup. The fatigue test is performed at a load ratio of R = 0.1, with a maximum stress in the pipe body of 161 MPa. The load is fluctuated at a frequency of 3 Hz. The connection failed after 10712 cycli as shown in Fig. 4. Several mechanisms contributed to the connection's failure. Firstly, a fatigue crack initiated at the last engaged thread of the pin and propagated over part of the pin's cross-section. This caused the load to concentrate on the remaining section and the partition of the threads in this area. Once this area became too small, the threads sheared of locally in this region and finally jumpout occurred.
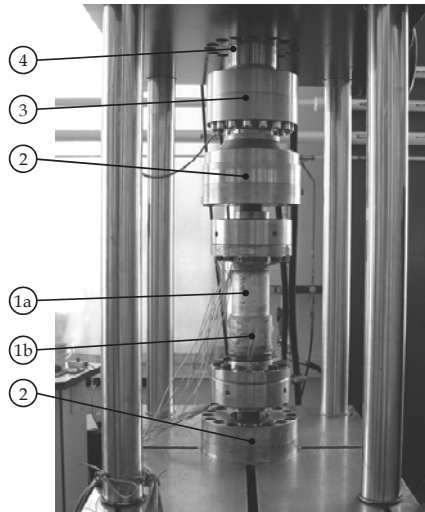
Figure 3. Axial tension setup.

Figure 4. Failed connection after fatigue test

4. Discussion

The strains measured during the axial tensile test are now compared to the simulated values obtained by the finite element model. In Fig. 5 and 6, the results are shown for respectively the axial strain values E_{xx} and the hoop strain values E_{zz} for the made up connection subjected to an axial tensile stress of

150 MPa in the pipe body. The strains are plotted along the axial length of the pipe where $x = 0$ corresponds to the outer left end of the box, as shown in the upper part of Fig. 5.

Figure 5. Comparison of axial strains E_{xx} (SG = measured strain gauge values).

Figure 6. Comparison of hoop strains E_{zz} (SG = measured strain gauge values).

It is noted that the strain values measured in the box are much lower than in the pin since the box is the more rigid part. The maximum axial strain appears around the region of the LET around $x = 20$ mm. For all strain components, the results obtained by the finite element model are in good agreement with the meas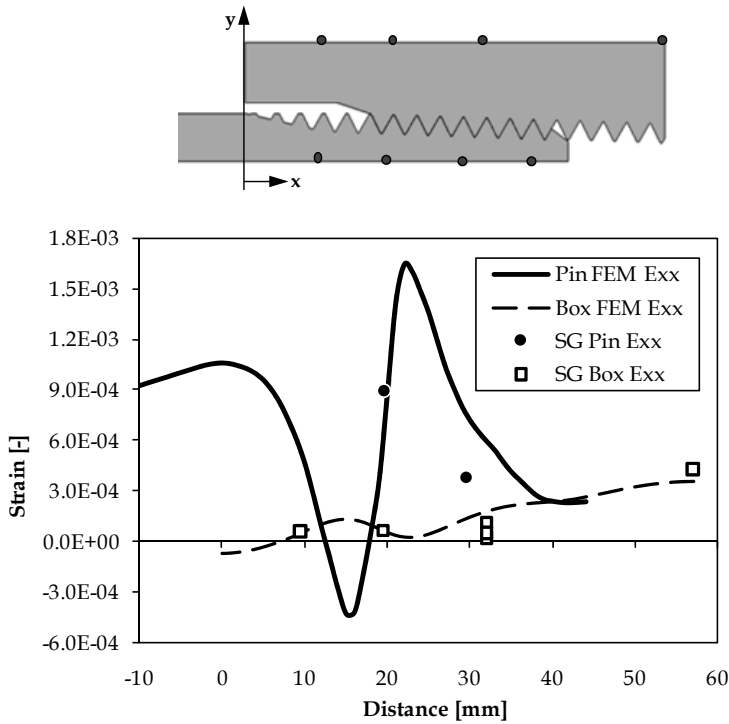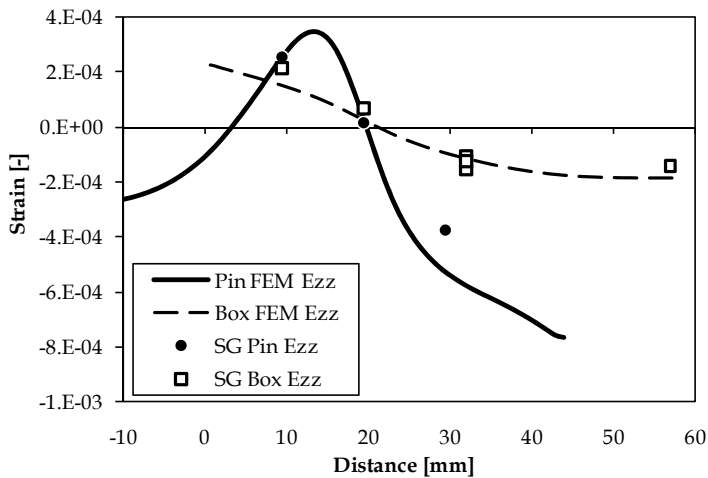ured strains. The RMS deviation is limited to 84 µε. Consequently, the model is validated for the axisymmetric load case of axial tensile loading.

5. Conclusions

In this paper the behaviour of a threaded pipe connection under axial tensile loading is investigated. This is done by a combination of finite element modeling and experimental validation. A good correspondence is found between the two data sets, which proves the validity of the 2D axisymmetric model. Following the quasi-static tensile test, a fatigue test is carried out on the sample in the same test setup. A fatigue crack initiated at the root of the LET thread of the male part of the connection, which is the location where the highest stress concentration appears in the simulations and where the highest axial strain values are measured during the experiments.

Acknowledgement

References

1. Assanelli, A.P., Xu, Q., Benedetto, F., Johnson, D.H., Dvorkin, E.N. (1997): Numerical/experimental analysis of an API 8-round connection. Journal of Energy Resources Technology-Transactions of the ASME. 119(2), pp. 81–88.

2. Griffin, R.C., Kamruzzaman, S., Strickler, R.D. (2004): Casing Drilling Drill Collars Eliminate Downhole Failures. Offshore Technology Conference, 3–6 May 2004, Houston, Texas, USA.

3. Van Wittenberghe, J., De Baets, P., De Waele, W. (2010): Non-Linear Contact Analysis of Different API Line Pipe Coupling Modifications, ASME Journal of Pressure Vessel Technology, 132(5), 051701.

The effect of standoff distance (SOD) on mechanical strength of cold flame-sprayed porous metallic coatings

[1]Gábor KALÁCSKA, [2]Lajos FAZEKAS, [3]Otto EBERST

[1]Institute for Mechanical Engineering Technology,
Faculty of Mechanical Engineering, Szent István University
[2]Faculty of Engineering, University Debrecen
[3]Universitatea De Nord, Baia Mare

Abstract

Cold flame-spray technology was investigated in many other areas of mechanical engineering during the past decades and gained overall acceptance in the field of vehicle parts, turbine elements, aviation…etc. However the technological steps are clearly described in the literature [1, 2, 3, 4, 5, 6] and detailed suggestions – regarding the powders, the spraying guns, part preparation and spraying methods - are available from different producers some lack of the technology was found. This paper describe the influence of spraying standoff distance (SOD) on normal component of coating bond strength ($R_\perp$) and on the shear component of coating bond strength ($R_\parallel$). For the test three different metal powder types were used.

Keywords

porous metal layer, cold flame-spray, normal and shear strength

1. Introduction

The technology of surfaces produced with thermal spraying underwent on spectacular development in the past decades and the development goes on nowadays, too. The method is also used at such advanced technical application as renewing, repairing parts of jet propelled power plant. We have put the emphasis to the cold flame spraying that is on the examination of surface coatings with porous structure. The cold flame spraying is a wide – spread method renewing shafts worn in normal work renewing sliding bearing surfaces, or other sliding surfaces well identifiable. The main advantage of the technology is it can be also used in case of alloyed shafts as avoiding heat effect higher than 200-300°C the get hardening, the texture change can be avoided.

   Concerning the practical application it is an outstandingly important fact that the spraying of powders takes place mainly with manual technology, surely this ensures the quickness, elasticity for the process. The manual process has always

got subjectivity and from this results that in case of at most powder compositions the suggested spraying distance as an absolute data can't be kept.

We have selected three, basically different powder alloys representing various powder groups from the powders suggested for cold flame spraying in the commercial turnover, suggested for the most extreme application of parts sprayed with cold technology and they function as sliding surface, too.

2. Materials and method

I have selected three basically different powder alloys representing various powder groups suggested for cold flame spraying in my research program suggested for the most extreme application of parts sprayed with cold technology and they function as sliding surface, too.

I have selected three characteristic powder-alloys for the extreme technological application fields of the cold flame-spraying metal power spraying technology to be characteristically distinguished by their chemical compositions.

- − HardTec 19400 – hard coating, protection against abrasive effects,
- − LubroTec 19955 – excellent sliding requirements,
- − DuroTec 19910 – tough and hard coating utilization of the dynamic loadability,

The manufacturer gives only indicative values about the chemical compositions of the powder alloys, therefore these were analyzed by EDX. The results are reported in Table 1. The characteristic components are Cr, Ni and Fe (in strongly varying proportions), but the following constituents could also be identified: C, Mn, S for each alloy, Mo and Co for DuroTec and LubroTec, B for DuroTec and HardTec, and Si for DuroTec. The alloy for the bonding layer (Xuper Ultra Bond 51000) contained Ni, Mo and Al.

The particle size of the starting powders was between 20 and 80 μm, as determined by vibrating sieving.

The substrate material for each test samples was 16MnCr5. Base (bonding) layer was made of Xuper Ultra Bond 51000.

Table 1. Composition of the applied alloys as determined by EDX (m%)

Alloy	C	Ni	Cr	Fe	Mn	Mo	Co	B	Si	S	Al
Xuper Ultra Bond 51000		89.5				5.4					5.0
DuroTec	0.1	84.6	9.4	2.1	0.02	0.3	0.05	1.1	4.8	0.015	
HardTec	0.1	1.1	15.8	78.1	0.08			1.0		0.018	
LubroTec	0.03	74.7	15.4	8.4	0.11	0.1	0.1			0.01	

Performing spraying-application tests during which we examined the density (porosity), the hardness, the bond strength, the conditions of surface energy, the adsorption – and emission capacity of lubricant of surface layers by applying several spraying distances which is the most subjective technological parameter in case of manual technology.

The main variable of my tests were:
  – generally suggested, producers' spraying distance (180 mm),
  – increased with 40% the spraying distance in extreme value,
  – reduced with 40% the spraying distance in extreme value, and
  – using further spraying distances between extreme values.

3. Test samples

Normal strength investigation
The normal component of bonding strength of the porous layer is defined as follows:

$$R_\perp = \frac{F_\perp}{A} \text{, where}$$

$R_\perp$ = Normal bonding strength (MPa)
$F_\perp$ = Normal force acting on the sprayed surface (N)
A = The sprayed area subjected to the normal force (mm^2).

There are various methods in the literature and engineering practice to carry out such test. I have selected the Nádasi-method, which uses the test sample shown in Fig.1. During the procedure the substrate part is pulled out from the ring while the porous coatings from the top surface of the substrate part is debonding. The measured force and the known surface area is used for calculation for normal strength.
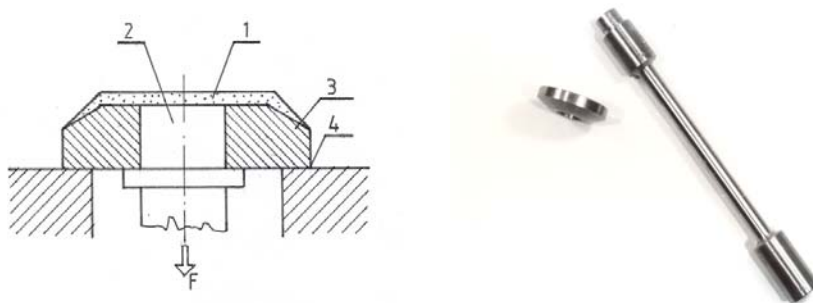

Figure 1. Test combination for normal strength tests.
1 – porous sprayed layer, 2 – tested substrate part, 3 – mating ring part, 4 – fixed base

Shear strength investigation

For the calculation of shear strength of the sprayed porous layer the following formula is used.

$$R_\| = F_\| / A, \text{ where}$$

$R_\|$ = shear strength (MPa)
$F_\|$ = acting shear force (N)
A = surface subjected to shear force (mm^2)

   In accordance with DIN 50161 standard we have selected the METCO method for the shear tests. The applied test sample can be seen in Fig.2.

Figure 2. Shear test samples.
1 – substrate part having sprayed and notched layer, 2 – shearing ring

4. Results and discussion

The dependence of normal component of coating bond strength ($R_\perp$) on the standoff distance for the various coatings is shown in Fig. 3. The evolution of $R_\perp$ proved to be sensitive to SOD and depended on the type of alloy applied. $R_\perp$ for DuroTec (compared hereinafter to the base value obtained at normal SOD), decreased upon increasing SOD, while it did not change much upon decreasing SOD. $R_\perp$ for HardTec decreased upon increasing SOD, but increased upon decreasing SOD. A completely different trend was observed for the LubroTec coating: $R_\perp$ decreased strongly upon decreasing SOD, and appeared to decrease slightly upon increasing SOD.
   This is in agreement with the above results, according to which the composition and hardness of LubroTec differ strongly from those of the other two alloys. The evolution trends of $R_\perp$ versus SOD can be fitted by second order polynoms. Comparing the three alloys, at and near the normal SOD, HardTec and LubroTec seem to have similar $R_\perp$ values (~14 MPa), while the corresponding value for DuroTec is smaller (~9 MPa). This is most likely connected to the hindered diffusion of B and Si due to the relatively low temperature of the cold flame-sprayed system.
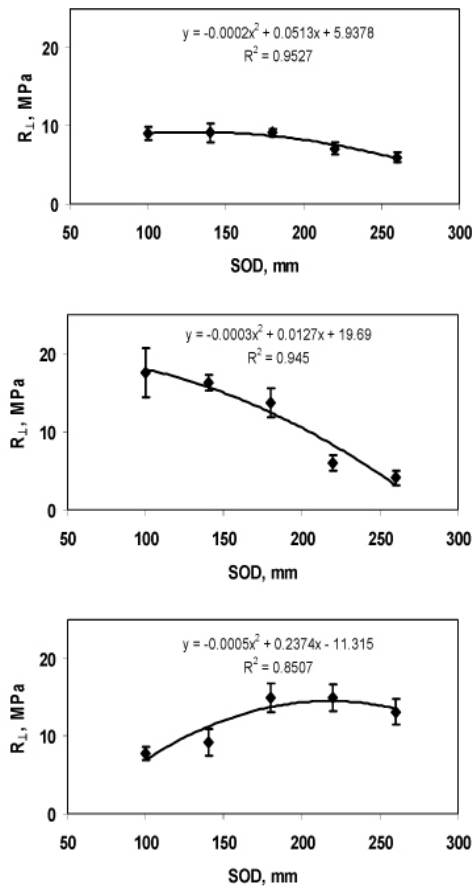
$$y = -0.0002x^2 + 0.0513x + 5.9378$$
$$R^2 = 0.9527$$

$$y = -0.0003x^2 + 0.0127x + 19.69$$
$$R^2 = 0.945$$

$$y = -0.0005x^2 + 0.2374x - 11.315$$
$$R^2 = 0.8507$$

Figure 3. Normal component of coating bond strength, $R_\perp$
From top to bottom: DuroTec, HardTec, LubroTec

Upon shear tests, no detectable scratch tracks remained on the samples, the coating was always sheared off in a form of a 2 mm thick single cylindrical piece, and shear took place inside the bonding layer. The dependence of shear component of coating bond strength ($R_\parallel$) on the standoff distance is shown in Fig. 4. According to these results, $R_\parallel$ was sensitive to SOD and depended on the type of alloy applied, similarly to the case of the normal component. In particular, for HardTec and DuroTec, deviation from the normal SOD was less detrimental in case of decreased SOD, while the opposite trend was observed for LubroTec. The maximum achievable values of $R_\parallel$ were about 40, 50 and 60 MPa for DuroTec, HardTec and LubroTec, respectively. Such a trend can be explained by the hindered diffusion of B in HardTec and of B and Si in DuroTec upon cold flame spraying. Comparing the normal and shear components of coating bond strength, the normal component was always much smaller than the shear one: the values of $R_\parallel/R_\perp$ proved to be about 4.4, 3.4 and 4 for DuroTec,

HardTec and LubroTec, respectively. As mentioned above, flame spraying is usually performed by hand, during which the normal SOD cannot be kept precisely. Therefore, the information presented in Figs. 3 and 4 can be of great practical importance.
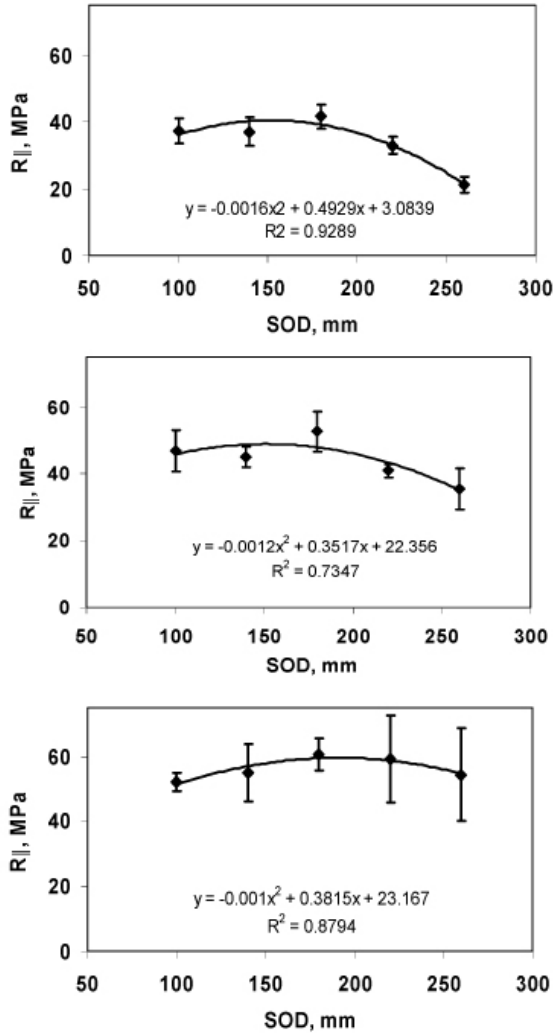

Figure 4. Shear component of coating bond strength, $R_{\parallel}$
From top to bottom: DuroTec, HardTec, LubroTec

5. Conclusion

Based on the normal directional bond strength tests carried out with the Nádasi – method it was established that the spraying distance influences the bond strength

with different degree and character in case of various powder alloys according to the followings:

    – The normal directional bond strength of the sprayed layer made of „DuroTec compositon" powder alloy is sensitive to the increase of spraying distance. The increase of the distance as compared with the 180 mm optimum spraying distance results strength decrease, the trend can be approximated with quadratic polynome:

$$y = -0,0002x^2 + 0,0513x + 5,9378$$

    The reduction of the spraying distance doesn't change in average the bond strength but the increased measuring results' standard deviations indicate the uncertainty of the technology in case of reduced spraying distance. The difference from the 180 mm spraying distance is less disadvantageous if it goes with reduction of spraying distance.

    – The average values of the bond strength in normal direction sprayed with „HardTec composition" coating slightly increased together with the standard deviation of the measuring results in case of reducing the spraying distance. The increase of the spraying distance reduces significantly the bond strength in normal direction. The trend can be approximated with quadratic polynome:

$$y = -0,0003x^2 + 0,0127x + 19,69$$

    The interval of the standard deviation distance was defined, which is a value between 140-180 mm at "Hard Tec composition" powder from the bond strength in normal direction standpoint.

    – The bond strength in normal direction of the sprayed layer with „LubroTec composition" powder alloy in the function of spraying distance results opposite trend with the HardTec and DuoTec compositions. The strength of the sprayed layer with "LubroTec composition" strongly decreases in case of reducing the spraying distance, while increasing the spraying distance reduces less the bond strength. The trend can be approximated with quadratic polynome:

$$y = -0,0005x^2 + 0,2374x - 11,315$$

    The internal of the standard deviation distance can be interpreted, its suggested value is between 180-220 mm.

It was proved with METCO-type measurings of shearing bond strength that the spraying distance influences the shearing bond strength in different degree in case of an three powder-alloys, but this influencing effect doesn't agree with the trends of bond strength in normal direction.

– The shearing bond strength of the "DuroTec" layer is sensible to the increasing of the spraying distance. The distance increase as compared with the optimum 180 mm spraying distance results strength descrease which can be approximated with quadratic polynome:

$$y = -0,0016x^2 + 0,4929x + 3,0839$$

The reduction of the spraying distance reduced hardly 10% in average the bond strength, the standard deviation of the measuring results are nearly identical (relative standard deviations 4-5,5%). I have established that the optimum spraying distance within interval the shearing bond strength of the layers sprayed with "DuroTec composition" powder alloy is 4,4 times higher than the bond strength in normal direction. This rate is smaller in case of other spraying distances.

– The average values of shearing bond strength of sprayed layer with „HardTec composition" coating decreased in small degree with hardly 5% in case of reducing the spraying distance, the standard deviation of values measured didn't change unfavourably, too. The increase of spraying distance reduces the shearing bond strength. The trend can be approximated with quadratic polynome:

$$y = -0,0012x^2 + 0,3517x + 22,356$$

The interval of the suggested optimum spraying distance is 150-190 mm at this powder alloy.

– The shearing bond strength of the "LubroTec" layer in the function of spraying distance resulted opposite trend with the "HardTec" and „DuroTec" coatings, which can be approximated by quadratic polynome:

$$y = -0,001x^2 + 0,3815x + 23,167$$

The shearing bond strength of the "LubroTec composition" coating changes in more sensitive way (more strongly decreases) to the reduction of spraying distance as in case of increasing the spraying distance. Concerning the shearing bond strength it is suggested to keep the 180 mm spraying distance.

References

1. Stern K. H. (1996): Metallurgical and Ceramic Protective Coatings. Thermal Spray Coatings p 261. Chapman & Hall.

2. Grainger S., Blunt J. (Eds.) (1998): Engineering Coatings: Design and Applications, 2nd ed., Woodhead Publishing Limited, Cambridge, UK.

3. Bach F.-W., Laarmann A., Wenz T. (Eds.) (2004): Modern Surface Technology, Wiley-VCH, Weinheim.

4. Davis J. R. (Ed.) (2004): Handbook of Thermal Spray Technology, ASM International, Materials Park, OH.

5. Maev R. GR., Leshchynsky V. (2008): Introduction to Low Pressure Gas Dynamic Spray: Physics & Technology, Wiley-VCH, Weinheim.

6. Molnár A. (2002): Termikus szórás. Miskolci Egyetem. Oktatási segédlet.

Measurement of ductile crack extension in laboratory scale fracture mechanics testing

[1]Matthias VERSTRAETE, [1]Wim DE WAELE,
[1]Stijn HERTELÉ, [1]Rudi DENYS, [2]Dries VAN PUYVELDE,
[2]Koen VAN MINNEBRUGGEN

[1]Department of Mechanical Construction and Production,
Laboratory Soete, Ghent University
[2]Ghent University

Abstract

Within nowadays applications of welded structures, monitoring of defects under large applied deformations can help to understand the behaviour of the entire structure. To monitor the stable crack extension of these defects, several techniques can be applied. Within this research, laboratory scale, non-welded test specimens were tested and two techniques were used to continuously monitor the ductile crack extension, namely the unloading compliance and potential drop technique. Both techniques were simultaneously applied. Based on finite element simulations the measured data is related to the crack size. It is observed that the potential drop technique is able to accurately determine both crack size and crack extension. In contrast, the unloading compliance technique overestimates the crack size, whereas the crack extension is correctly estimated by this technique.

Keywords

1. Introduction

Welded structures unavoidably contain defects. When these structures are subjected to high static loads (i.c. large deformations), the present defects may demonstrate significant stable crack extension before collapse of the structure [Kibey, 2011]. To assess the potential detrimental influence of these defects, fracture mechanics tests are commonly carried out on sample specimens [Shen, 2009]. This yields insight in the behaviour of such defects under fully plastic loading conditions.

Since testing full scale structures is only in rare cases economically viable, small scale test specimens are frequently used and advised by standards, e.g. ASTM E1820 [ASTM, 2009]. A commonly used test configuration is the Single Edge Notched Tensile specimen, which consists of a rectangular bar containing

a through thickness fatigue pre-cracked artificial defect. This specimen is loaded in tension, whereby two variants exist depending on whether the rotation is allowed in the grips (pin-loaded) or not (clamped). Within the framework of this paper, the focus is on clamped SENT specimens [Cravero, 2006; Dexter, 2010].

To continuously monitor the behaviour of the crack during testing, crack growth measurements are performed. Two different measurement techniques are discussed in this paper, the unloading compliance (UC) technique and the direct current potential drop (DCPD) technique. So far, both techniques have only been applied on weld-free samples to check for their feasibility. The application of both techniques for welded samples is part of future research.

2. Unloading compliance technique

Principle
A commonly used method is the unloading compliance technique. Upon loading, specimens are partially unloaded at predefined deformation levels, allowing for the determination of the compliance (C) (see also Figure 1). Subsequently, the measured compliance is related to the crack length. Therefore, several analytical relations are available for standardized fracture mechanics test specimens [Cravero, 2007; Shen, 2009]. However, within the framework of this paper, an in-house developed parametric finite element model is used to obtain the required relationship.

Finite element model
A parametric Python script has been developed for Abaqus® 6.10. This script allows automatically generating and analyzing a finite element model of a SENT specimen, based on a predefined set of geometry, material, loading and meshing parameters.

The geometry of the weld-free SENT specimen is defined by the width (B), height (W) and length of the specimen. In addition, the notch is defined by its relative depth (a/W-ratio) and notch tip radius (see also Figure 2). Within the framework of this study, a notch tip radius of 2.5 µm has been applied, which is widely used in modeling to represent an infinitely sharp (fatigue-precracked) notch [Thaulow, 1999]. Furthermore, the constructed finite element model only represents one half of the specimen, symmetry boundary conditions are assumed along the longitudinal direction. The experiments analyzed in this paper relate to clamped SENT specimens. Therefore, the load boundary conditions restrict all degrees of freedom; no rotation is allowed at the free ends and fixed displacements are applied at the free surfaces.

Compliance theory assumes that this compliance only depends on the elastic material properties and the geometry of the specimen. Consequently, linear elastic material properties are assigned to the finite element model (Young's modulus equal to 206980 MPa). The applied mesh is represented in Figure 2, a spider web mesh is applied around the crack tip. Since a local thickness reduction is often applied in actual SENT specimens, the finite element model

also allows incorporating this local thickness reduction (also referred to as side grooves). This reduction is realized by means of a coordinate transform, applied to the nodes of the mesh. The geometry of these side grooves is determined by the amount of thickness reduction ($\%_{groove}$), the opening angle (α_{groove}) and the root radius of the groove (r_{groove}). Analogous to the performed experiments, a 15% thickness reduction was modeled with a root radius of 0.4 mm and an opening angle of 90°.
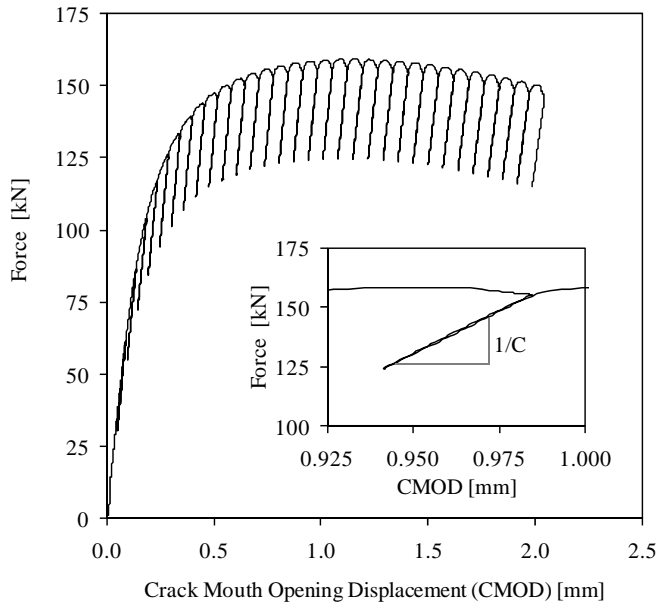

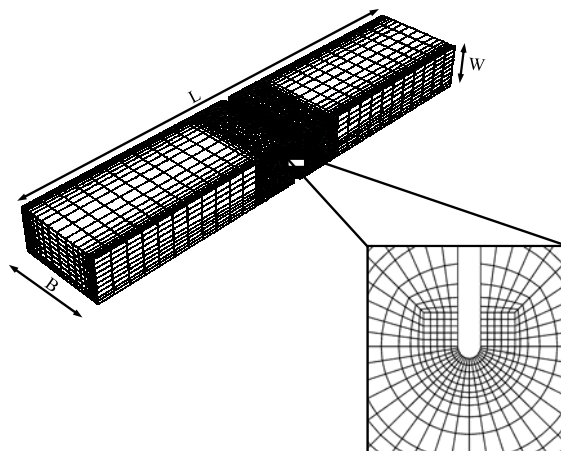*Figure 1.* Result obtained from unloading compliance measurements

Figure 2. Mesh and global dimension of SENT specimen

Experimental procedure

For the experimental tests, the crack mouth opening displacement (CMOD) and force (P) are continuously measured. At predefined CMOD-values, the specimen is elastically unloaded. The unloading range is calculated as follows:

$$P_{unload} = \frac{1}{4} B_e (W - a_0) \sigma_e \qquad (1)$$

With:

B_e effective specimen thickness at crack plane (0.85B for specimens with side grooves) [mm]

σ_e average of yield and tensile strength [MPa]

   In addition, six unloading cycles were carried out in the linear elastic range to determine the initial compliance of the specimen. Subsequently, the slope is determined for each unloading cycle.

   From the finite element simulations, a relationship between crack length and compliance is obtained. This relationship is graphically represented in Figure 3.
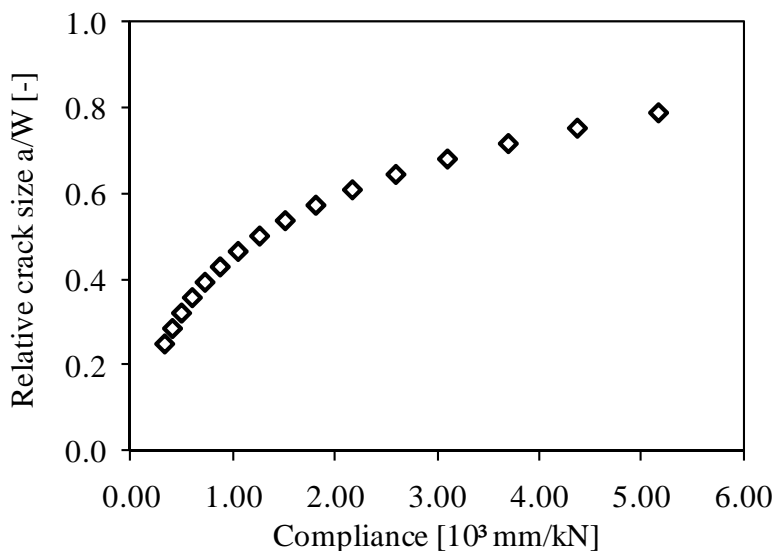

Figure 3. Relationship between crack size and compliance through 3D FEA

3. Potential drop method

Principle

A second method which can be applied to continuously determine the crack length, is the potential drop method. Two different approaches exist, the direct current (DC PD) and alternating current (AC PD) method. A literature survey

has clarified that the direct current method is more suitable for crack sizing, whereas the alternating current method is more suitable for crack detection [Van Minnebruggen, 2011]. However, it should be noted that relative large currents are required for the application of the DC method. For the test specimens under investigations a current of 25 amps was applied.

As the crack grows upon loading, an increase of the potential drop across the cracked ligament is expected. To relate this increasing potential drop to the crack size, finite element simulations are believed to result in a reliable relationship.

Finite element model

Analogous to the compliance technique, a parametric finite element model has been developed. However, for this application no deformation was applied as the coupled thermo-electrical analysis does not allow for this. Instead, a constant current $(= I_{in} = I_{out})$ is applied on two pins near the end of the specimens, reflecting the experimental conditions. In addition, two pins are placed near the crack, representing the measurement pins from which the potential drop across the growing crack is retrieved. The material is defined by its conductance. This conductance is obtained through reverse modeling, considering the initially measured potential drop and the initial crack size.
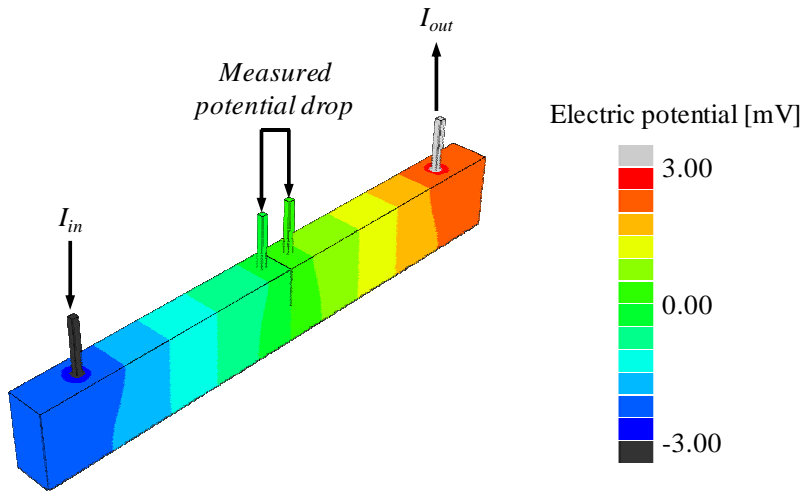
Figure 4. Simulated potential field in SENT specimen

A characteristic configuration is represented in Figure 4, showing the obtained potential field. It is observed that, assuming this reflects the experimental conditions, a homogeneous potential field is obtained between the current input region and the cracked region. Such homogeneous zone is important since interaction between both could possibly complicate the relationship between crack size and potential drop.

Experimental procedure

Simultaneous with the unloading compliance measurements, the potential drop measurements were performed. During the experimental testing, the potential drop is measured every 5 seconds in the plastic cycles, no measurements were performed during the elastic unloading cycles.

From the experimentally measured data, an increase of the potential drop was already noted from the start of the test. Since crack growth is not believed to start immediately, the linear increase observed during the first phase of the test is attributed to blunting and (local) plastic deformation (strain hardening). The presence of such linear blunting phase is also reported in literature [Wilkowski, 2009]. The actual potential drop, related to crack growth, can thus be obtained by subtracting this linear increase from the measured signal. The obtained potential drop is subsequently related to the crack length by means of the relationship graphically represented in Figure 5.
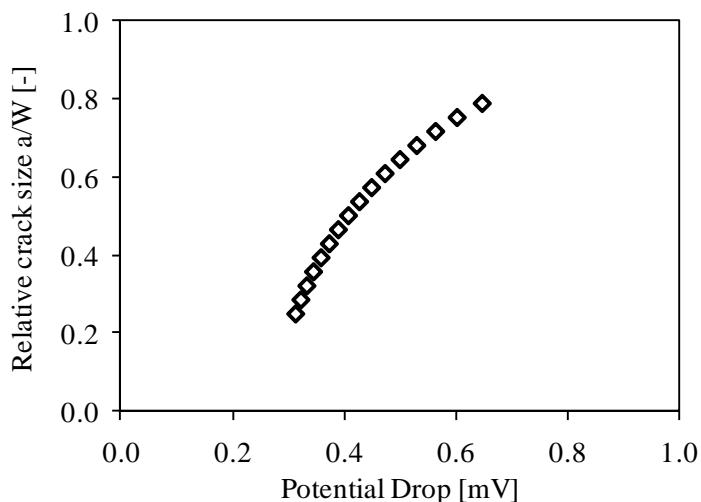
Figure 5. Relationship between potential drop and crack size through 3D FEA

4. Results and Discussion

Test specimens

Within the framework of this research, 2 clamped SENT tests have been performed. All specimens were extracted from plain pipe material grade API-5L X60 and had the same dimensions; a width of 28 mm, height of 14 mm and a relative crack size *a/W* of 25%.

These specimens are fatigue pre-cracked in three-point bending. After this pre-cracking, side grooves are applied resulting in a local thickness reduction of 15%. The actual SENT testing is carried out with hydraulic clamps; a daylight grip length of 10*W* was used.

Unloading compliance test results

From both tests described above, the compliance has been obtained at subsequent intervals. By applying the relationship obtained from the finite element simulations, the crack size has been calculated for both tests. The calculated crack size is plotted in Figure 6 and Figure 7 for test SET11 and test SET12 respectively.

In addition to aforementioned measurements, the tested specimens have been broken open in liquid nitrogen after testing. From the fracture surface both the extension of the fatigue pre-crack and the amount of stable crack extension could be measured. These data are represented by the dotted lines in Figure 6 and Figure 7.
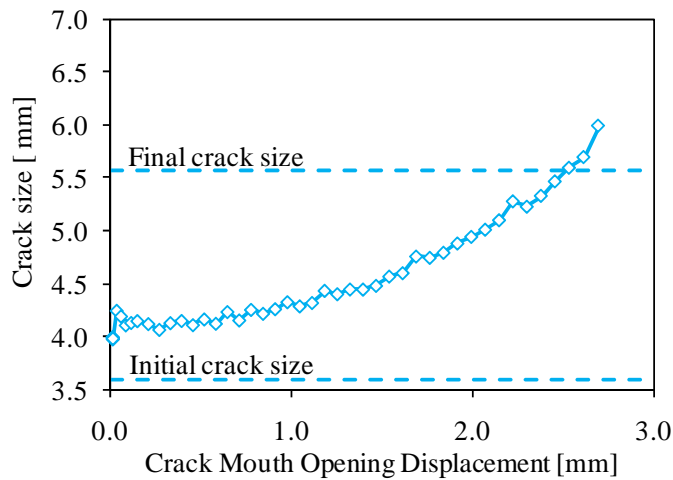

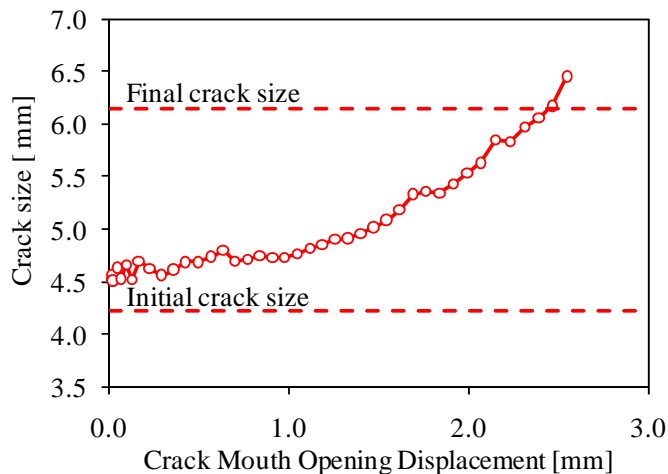*Figure 6.* Calculated crack size for test SET11

Figure 7. Calculated crack size for test SET12

Comparing both reveals an overestimation of the initial and final crack size, whereas the amount of ductile crack extension is believed to be well estimated. For test SET11 the measured crack extension was 1.98 mm, the calculated extension equals 2.00 mm. Test SET12 showed a crack extension of 1.93 mm, while the calculations revealed 1.90 mm of crack extension. Therefore, it is concluded that the unloading compliance technique is able to describe the crack extension with large precision, the exact sizing of the cracks is however not yet accurate. The reason for this overestimation is most probably in the rotation of the specimen, which has not been accounted for in the current procedure. Future research will focus on the description of this rotation.

Potential drop test results
The data obtained from the potential drop measurements revealed the presence of a linear phase in the CMOD-PD diagram, during the initial loading. Upon loading the increase of the potential drop becomes more than linear, signaling stable crack extension (see Figure 8).

Subtracting the linear increase of the PD from the measured signal yields the potential drop related to crack extension. For test SET11 and SET12 this is graphically represented in Figure 9 and Figure 10 respectively. This curve is subsequently related to the crack size by means of the previously described relationship (see §3.3). The obtained relationship between CMOD and crack size is plotted in Figure 9 and Figure 10 together with the measured initial and final crack sizes.
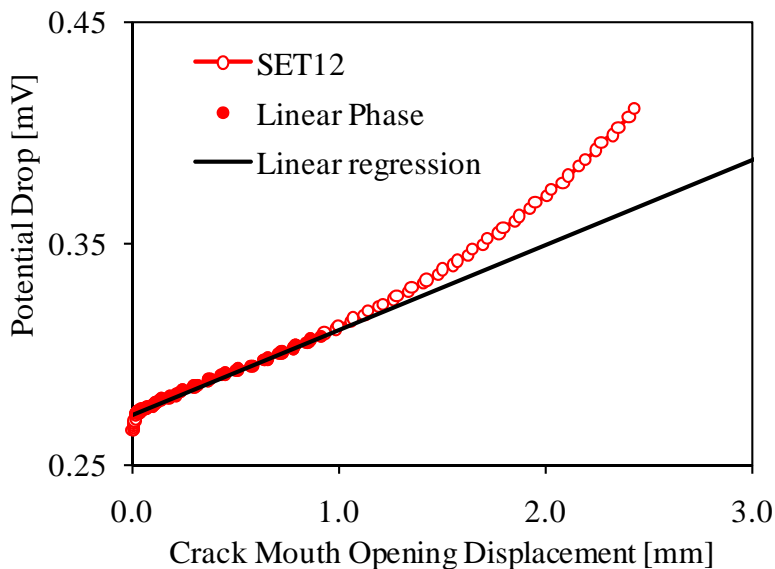

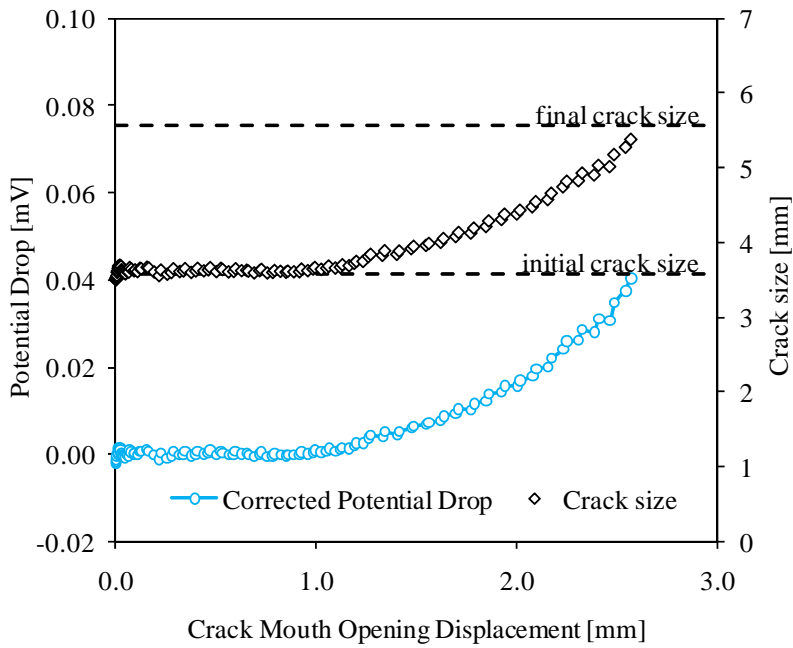*Figure 8.* Measured potential drop signal and linear
blunting phase

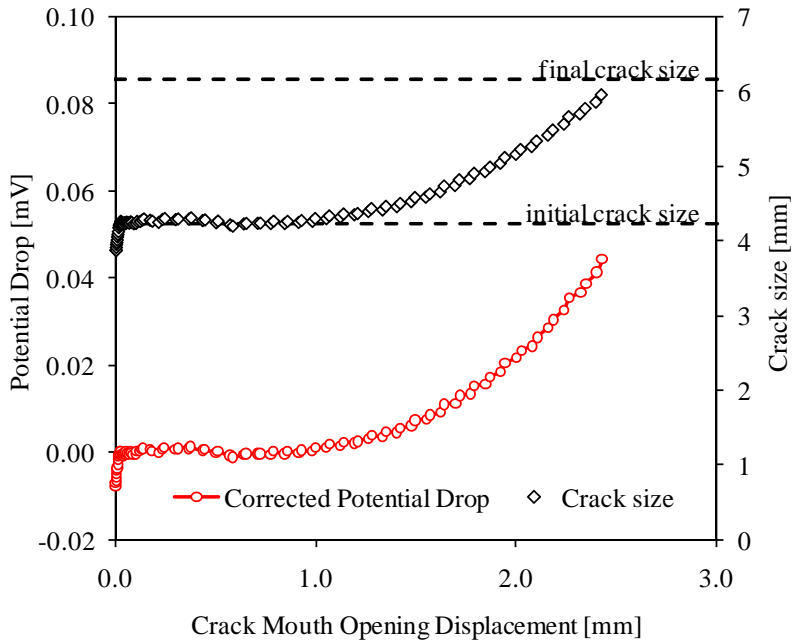*Figure 9.* Calculated crack size and corrected potential drop signal (SET11)

Figure 10. Calculated crack size and corrected potential drop signal (SET12)

An excellent correspondence is observed between calculated and measured final crack size. The same applies for the initial crack size, which is however not surprising regarding the reverse modeling technique applied to determine the conductance of the material (see also §3.2).

5. Conclusion

The stable crack extension in two fracture mechanics single edge notch tension tests has been fully analyzed based on the unloading compliance and potential drop technique. It is concluded that:
– The unloading compliance technique allows to accurately determine the amount of stable crack extension.
– Crack sizing by means of the compliance technique is however not straight forward, an extra rotation correction might be required to overcome this problem.
– The potential drop technique allows determining both crack size and cracking extension accurately.

Acknowledgement

References

1. American society for testing and materials, ASTM (2009): E1820-08a Standard test method for measurment of fracture toughness.

2. Cravero, S. (2006): Correlation of fracture behavior in high pressure pipelines with axial flaws using constraint designed test specimens – part I: plane strain analysis. Engineering Fracture Mechanics.

3. Cravero, S. (2007): Estimation procedure of J-resistance curves for SE(T) fracture specimens using unloading compliance. Engineering Fracture Mechanics.

4. Dexter, E. (2010): SE(T) testing of pipeline welds. International Pipeline Conference, Calgary, Canada.

5. Kibey, S. (2011): Full-scale test observations for measurement of tensile strain capacity of welded pipelines. International Offshore and Polar Engineering Conference, Maui, USA.

6. Shen, G. (2009): Measurement of J-R curves using single-specimen technique on clamped SE(T) specimens. International Offshore and Polar Engineering Conference, Osaka, Japan.

7. Thaulow, C. (1999): Constraint effects on crack tip stress fields for cracks located at the fusion line of weldments. Computational Material Science.

8. Van Minnebruggen, K. (2011): Experimental evaluation of plastic deformation and ductile crack extension. Master Thesis Ghent University (in Dutch).

9. Wilkowski, G. (2009): Using D-C electric potential for crack initiation / growth monitoring during testing of weld metal fracture specimens. Pipeline technology conference, ostend, Belgium.

Influence of tool–piece friction on material flow in inverse extrusion

Lucian BUTNAR, Horia CIOBAN, Otto EBERST

North University of Baia Mare, Romania

Abstract

Punch-material and material-active plate friction has a great influence on material flows quality, extrusion process, on roughness and quality of the processed piece. The paper presents researches about some important aspects concerning material flow in manufacturing process of metal pieces, through inverse extrusion. The tribo-system of plastic deformation punch-piece-active plate is very complex and it is characterized by elementary couples of friction that compose it. Using different lubricants on contact surfaces deformation tool-piece may have a favorable influence on flow quality and on manufactured piece.

Keywords

Extrusion, friction, tribo-system, flow of material, piece's quality

1. Introduction

Extrusion of pieces is a volume pressure procedure in which, under the compression force action of punch, the material solicited on three-dimensional compression has to take through plastic flow, the space between punch and plate – figure 1. Depending on material processed, used machinery, dimensional precision, form and the needed surface quality, extruded piece, can be realized on cold, semi-warm and warm. These high forces need powerful equipments and also high price.
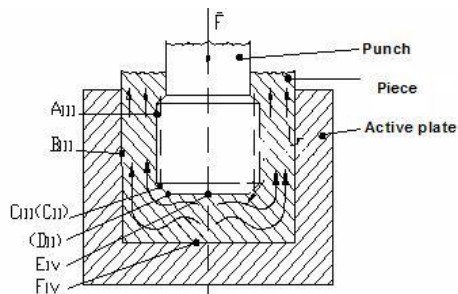

Figure 1. Inverse extrusion.

Therefore, the procedure is applied especially in great series production. Extrusion procedure is used for a large scale of materials: plastics, metals and non-ferrous alloys and carbon and allied steels with low carbon equivalent content.

Researches on inverse extrusion are less than researches for direct extrusion and those for inverse extrusion of pieces with thick walls are almost non-existent. So, in industry, the inverse extrusion is more difficult to apply than the direct extrusion.

2. Tribo-system

The theoretical researches shows a complex inter conditioning between:
– material flow;
– components in contact;
– these components characteristics;
– works environment;
– deformation tool roughness;
– precision of piece;
– technological process parameters multitude.

These interdependences impose a systemic abortion for inverse extrusion process of pieces. Comprising of elements, functions and levels into a unitary form, based on systems theory (Czihos, 1978) will conduce to a "building model" construction: definition for deformation tribo-system for inverse extrusion of a piece – figure 1. During plastic deformation process, there are initializing and developing tribo-contacts between tool and piece surfaces, the ensemble tool-piece becoming a complex couple for plastic deformation. This complex couple and component elementary couples - table 1 - have peculiarities to friction couples, which are characteristics for functioning machine elements:
– couples are submitting by very strong stress that produces material flow;
– mechanic characteristics are complete different – "strong" component (tool) is stressed in elastic domain and the "soft" component (piece) is stressed in plastic domain, through hardening;
– elementary deformation couples are instantaneously - "strong" component is permanent and the "soft" component is other in each moment, being replacing by flowing, with new material stratums;
– deformation couple is very complex, having a numerous elementary couples (6) that will determinate a complex material flow and numerous influence factors;
– complex deformation couple comprises a fundamental elementary couple (superior couple of class II, stressed by deformation forces with essential roll for material flow and its quality), numerous (3) principal elementary couples (inferior couples of class III, stressed by friction forces or deformation force components); the others are secondary elementary couples (inferior couples of class IV, with negligible influences on surface but important for interior material stratums flowing).

Table 1. Elementary couples components of complex couple

Elementary couple	Elementary couples characteristics		
	Contact type	Force	Couple class
A_{III} –Surface punch/material	Generalized cylindrical surface	F_p – friction force	III Inferior
B_{III} – Lateral surface plate/material	Cylindrical surface	F_p – friction force	III Inferior
C_{III} $(C_{II})*$ - Active surface punch/material	Conical surface (linear contact)	F_α – deformation force	III Inferior (II Superior)
$(D_{II})*$ - Edge punch h/material	Linear	F_α – deformation force	II Superior
E_{IV} – Frontal surface punch/material	Plane surface	$F=F_p+F_\alpha+F_n$ Total force for extrusion	IV Inferior
F_{IV} - Frontal surface plate/material	Circular plane surface	$F=F_p+F_\alpha+F_n$ Total force for extrusion	IV Inferior

3. Material flow

The process is characterized through unitary efforts of intense spatial compression $\sigma > \sigma_c$ needed for material flow through space between punch and active plate. Based on plasticity theory, it was realized tensions state scheme deformation state scheme on infinitesimal element with cubic form considered in different zones of material. On these volume elements it was established distribution of principal unitary efforts σ_x, σ_y, σ_z and distribution of specific deformations ε_x, ε_y, ε_z on the three principal directions x, y, and z - – figure 2.
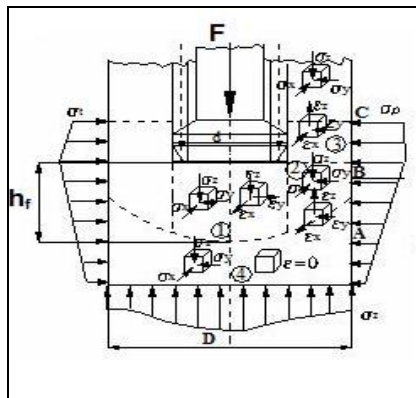

Figure 2. Schemes of unitary efforts
and of deformations

Inverse extruded material can be divided (Butnar & Cioban, 2005) in four distinct zones:

- zone 1 – deformation focus – placed under stamp, with h_f, depth, is strong strained on try-dimensional compression that produces reduces of element dimension on z direction and elongation on x and y directions;
- zone 2 – placed under the punch level, in its exterior, strong strained and deformed where is registered reduces of element on y direction and elongation on x and z;
- zone 3 – lateral wall of tubular piece with internal surface;
- zone 4 – non-extruded material.

Flowing stratums of material is influenced by some factors:

- extruded material and its proprieties;
- deformation grade;
- deformation speed;
- punch-material and material-active plate friction;
- produced piece dimensions.

Un-uniformity flowing of extruded material and piece quality can be characterized by the quality indexed deformation focus high (Socaciu, 1996), relation 1:

$$h_{f1} = \sqrt{\frac{\sqrt{\varepsilon}(1-\varepsilon)(0,5+\mu_p)}{2\beta \cdot \varepsilon(\sqrt{\varepsilon}+2\mu_m)}} \tag{1}$$

where μ_p, μ_m are friction coefficients between semi-product and punch and between semi-product and active plate, $\beta \cong 1.1\ldots1.12$ – Lode coefficient; $\varepsilon = d^2/D^2$ – deformation grade.

Growth of deformation focus high h_{f1} means a superior quality of surfaces of the piece, of structural and physic-mechanical proprieties. In deformation process, is comprised a bigger volume of material. Difference between flowing speed of contiguous stratums is lower, deformation un-uniformity is attenuated and the risk for interior defects is much diminished.

4. Experimental

Material used on experimentation researches was aluminum Al 99.5, semi-warm extruded, 265°C temp., on a hydraulic press PH200 with an extrusion mould, made through personal conception. Material deformation grade on reference diameter was important:

$$\varepsilon = d^2/D^2 = 60.49\% \tag{2}$$

Material flow process was researched through inverse extrusion of a piece with internal diameter d=ø70 starting from a cylindrical semi-product with

dimensions diameter D=ø90 and height H=30mm. The punch and active plate were made of allied steel.

Extrusion was in 4 different lubrication states of punch-material contact (friction coefficient μ_p) and material-active plate (friction coefficient μ_m):

- dry ($\mu_p=\mu_m=0.64$);
- lubrication with hydraulic oil H32EP ($\mu_p=\mu_m=0.31$);
- lubrication with processing oil MET P1C ($\mu_p=\mu_m=0.30$) and
- lubrication with graphite on oil support MET P1C, granulation 1…2 μm, ($\mu_p=\mu_m=0.24$).

For flowing research and friction influence, the semi-product was made by 2 semi-cylinders and on separation plane was traced, by a pantograph milling machine, a fine rectangular net, with side 2.5 mm, precision 0.01 mm, canal width 0.5 mm and depth 0.3 mm.

Extrusion process has modified the net lines. Into separation plane, there was a complex flowing in concordance with the theoretical results.

High determination of deformation focus h_f was made by a measurement instrument through co-ordinate ZKM 05-250D, with precision 0.5 μm, between internal frontal surface of piece and the last "horizontal" line of the deformed net – figure 3. Focus measurement was made on separation plane for two pieces, with the next results - figure 4.
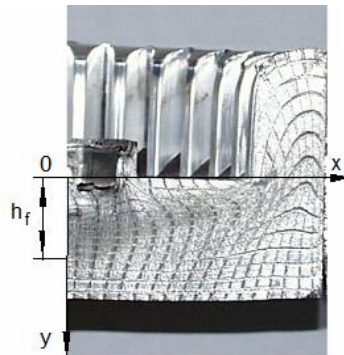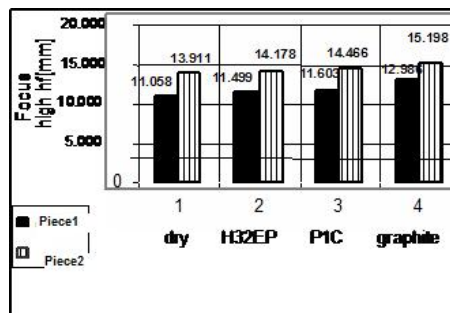

Figure 3. Determinations of deformation focus

Figure 4. Variation of focus deformation with tool-piece friction

5. Conclusions

The most important conclusion is that the deformation focus grows together with tool-piece friction reducing, that favors a more uniform flow and a piece with unitary structure and proprieties. The deformation focus grows is maximum on graphite lubrication, where it grows with about 17.5% towards dry friction. The graphite lubrication offers the best quality of flow material and of processed piece.

On lateral wall of piece, there are registered axial growths of "cell", that confirm material elongation resulted from theoretical studies. But "cells" growths are different: higher in inferior part of piece wall ($\Delta l \approx 0.5\ldots0.7$ mm) and reduced in superior part ($\Delta l \approx 0.05\ldots0.15$ mm).

Lubricant presence favors deformation, "cell" growths being higher on graphite and reduced on mineral oils. Lubricant introduced on surface contact tool-piece reduces deformations non-uniformity. On dry friction, on external wall of piece appear elongations of sliding lines, very pronounced at a half of wall thickness. Using lubricant, this advance of central stratum, decreases. Deformation is most uniform using graphite on support P1C, when the net lines remain approximate at the same level, horizontal.

References

1. Butnar, L., Cioban, H. (2005). Cercetari privind influenta materialului asupra indicilor de calitate la extrudarea inversa a rotilor dintate, *Proceedings of Tehnologii Moderne. Calitate. Restructurare*, Mazuru, S., pp. 321-324, ISBN 9975-9875-4-0, Tehnical University of Moldova, may 2005, Chisinau

2. Czichos, H. (1978). *Tribology*, Elsevier Publishing Company, Amsterdam

3. Socaciu, T., (1996). *Cercetari si experimente asupra exploatarii la rece a aliajelor neferoase si otelurilor utilizand frecarea ca forta activa*, Ph.D. Thesis, Transilvania University, Brasov

4. Tapalaga, I., Berce, P. & Achimas, G. (1986). *Extrudarea metalelor la rece*, Editura Dacia, Cluj Napoca

Test of the electro-rheological attributions of silicon oil without additives under flow mode

László FÖLDI, László JÁNOSI

Department of Mechatronics, Institute for Mechanical Engineering Technology,
Szent István University

Abstract

A claim has come up in the research of the mechatronical systems to develop special materials that can get information from a computer and change their attribution accordingly. From a control technology point of view using electric or magnetic field is the most obvious. One group of these materials is electro-rheologic (ER) fluids that change their shear strength feature according to the electric field applied. The main goal of this work is to build up a test station for determining the effects and the relationships between the oil parameters and the electric field applied. The unique ER valve construction and the test apparatus are shown and also the function tests of this unit have been carried out.

Keywords

Electro-rheological effect, Flow control, Hydraulics

1. Introduction

The electro-rheological effect
The change in apparent viscosity of electro-rheological (ER) fluid is dependent on the applied electric field, i.e. the potential divided by the distance between the plates. The change is not a simple change in viscosity, hence these fluids are now known as ER fluids, rather than by the older term Electro Viscous fluids. The effect is better described as an electric field dependent shear yield stress. When activated an ER fluid behaves as a Bingham plastic (a type of viscoelastic material), with a yield point which is determined by the electric field strength. After the yield point is reached, the fluid shears as a fluid, i.e. the incremental shear stress is proportional to the rate of shear (in a Newtonian fluid there is no yield point and stress is directly proportional to shear). Hence the resistance to motion of the fluid can be controlled by adjusting the applied electric field.

Properties of electro-rheological fluids
Electro-rheological fluids are suspensions of extremely fine non-conducting particles (up to 50 micrometers diameter) in an electrically insulating fluid. The apparent viscosity of these fluids changes reversibly by an order of up to

100,000 in response to an electric field. For example, a typical ER fluid can go from the consistency of a liquid to that of a gel, and back, with response times on the order of milliseconds. The effect is sometimes called the Winslow effect, after its discoverer the American inventor Willis Winslow.

Challenges and advantages of ER phenomenon
A major problem is that ER fluids are suspensions, hence in time they tend to settle out, so advanced ER fluids tackle this problem by means such as matching the densities of the solid and liquid components, or by using nanoparticles, which brings ER fluids into line with the development of magneto rheological fluids. Another problem is that the breakdown voltage of air is ~ 3 kV/mm, which is near the electric field needed for ER devices to operate. An advantage is that an ER device can control considerably more mechanical power than the electrical power used to control the effect, i.e. it can act as a power amplifier. But the main advantage is the speed of response, there are few other effects able to control such large amounts of mechanical or hydraulic power so rapidly. Unfortunately, the increase in apparent viscosity experienced by most electro-rheological fluids used in shear or flow modes is relatively limited. The ER fluid changes from a Newtonian liquid to a partially crystalline "semi-hard slush". However, an almost complete liquid to solid phase change can be obtained when the electro-rheological fluid additionally experiences compressive stress (MONKMAN 1995). This effect has been used to provide very effective clutches or hydraulic valves.

2. Development, structure and operation of an electro-rheological valve

The ER phenomenon as a material model is described by the Bingham model related to ER liquids, which is based on the mathematical model describing the non-newton liquids (LEE 2002). The Bingham model is a complex viscoplastic rheological model (CSIZMADIA 2003). As a material model it can be divided into an ideally ductile an ideally viscous member (ZRÍNYI 1999). (Fig. 1)
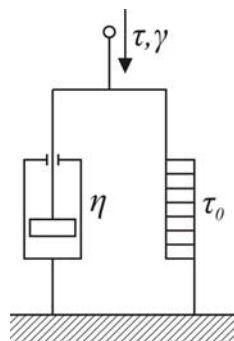

Figure 1. The Bingham model
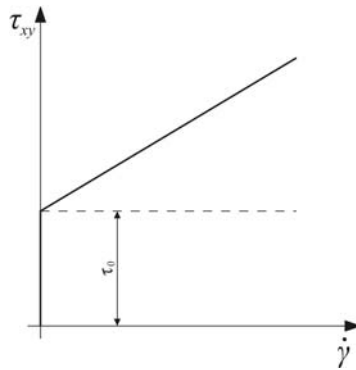
Figure 2. The shearing tension in the function of
shearing gradient

Research objectives

The aim of testing flow properties of the ER liquids is to establish a model, which can be generally applied of testing the behaviors of ER liquids made of different materials considering the physical data of the applied materials. By computer simulation the parameters of this mathematical model can be determined, which can be generated by minimum search. As the first step of the model identification the approximate search of the minimum of the established target function is accomplished by genetic algorithm, then the refinement of the result with the known numerical methods.

The ER valve

During the further material and application tests it is practical to use a device which has application possibilities too. In this consideration for further investigations we need the design of a hydraulic ER valve, which can be operated built in hydraulic circuits.

Figure 3. The ER valve

3. Development of measuring system for investigating the features of electro-rheological fluids

Applied test principle
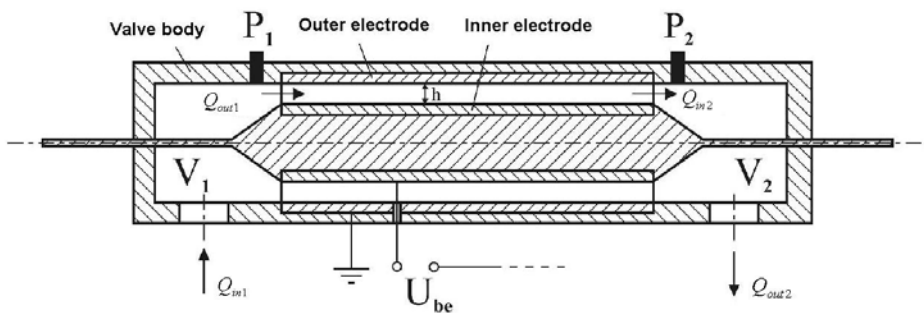Consider two concentric pipes (external and internal electrodes) and constant fluid flow is flowing between them. An electric field will be developed according to the electric potential applied on the electrodes and the gap between the electrodes and all of these causes the change of shearing strengths of fluid. The magnitude of change can be definitely determined from the pressure drop. During the test series the fixed parameters relating to the individual set of measurement are: fluid flow, oil temperature, fluid concentration. The only variable parameter is: the electric field. The parameter to be tested is the pressure drop and the calculated one is the shearing strength.

Design of hydraulic measuring circuit
The system consists of three main parts, like: the hydraulic power unit, ER circuit, data acquisition and control system. The hydraulic unit ensures the flow of ER fluid by a driving servo cylinder. The ER valve with flow meter and the pressure difference meter are fitted into the ER circuit.
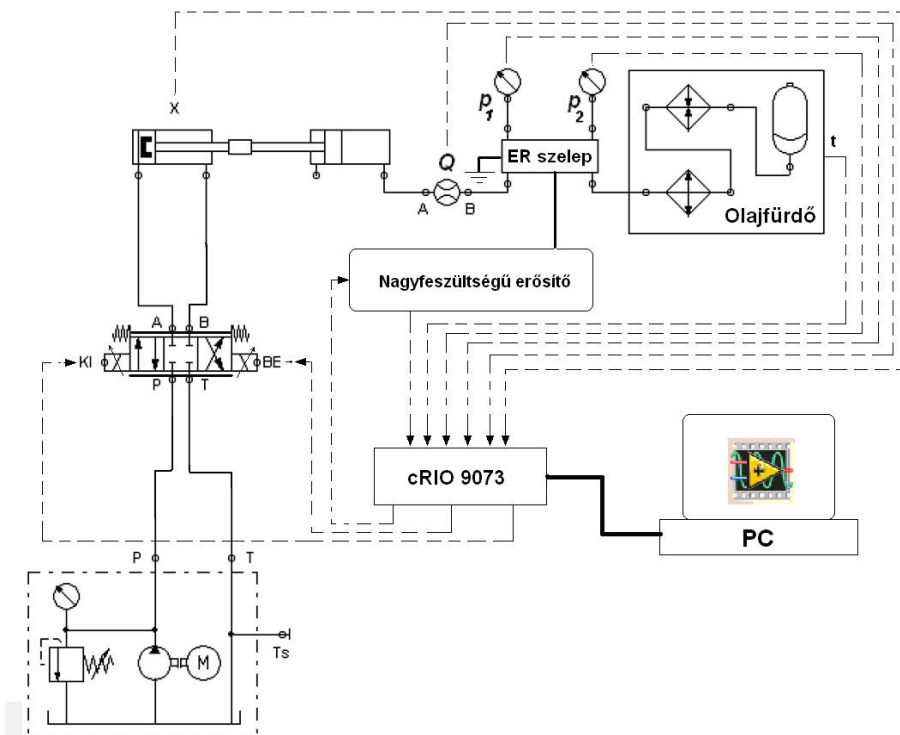

Figure 4. Experimental setup

Test control and data acquisition

The applied NI CompactRIO™ programmable automation controller is a modular system; out of its modules we used the analogue-to-digital converter (NI 9201), for a dual purpose. On the one hand we applied it in the controlling process to measure the voltage signal (which is in proportion to the displacement) provided by the displacement encoder. On the other hand we used it in collecting data about the voltage signals corresponding to pressure values provided by the analogue pressure sensors. The communication between the CompactRIO™ and the computer was ensured by an Ethernet connection. We realised the real-time control by applying the FPGA module of CompactRIO™ programming it in the LabVIEW 2009 software.

4. Test measurement

The pressure difference required by the ER fluid to flow was ensured by a bladder-type accumulator had been pre-charged up to 6 bar before the experiment. The measure of orifice of applied ER valve is h = 0.5 mm, the length is l = 200 mm. During the test we applied silicon oil without additives, whose viscosity is 50 mPas. The test took place in 24 $^{\circ}$C.
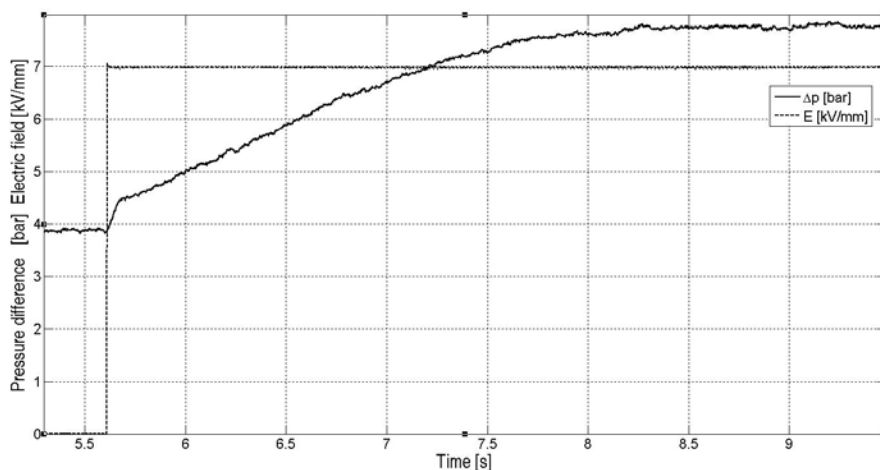
Figure 6. The results of measurement (Flow 1,5 l/min)

Fidure 6 shows the pressure drop at the ER valve while the electric field changes from 0 to 7 kV/mm. At this test the flow rate flowing through the ER valve is 1,5 l/min. In the figure we can see that the pressure increase can be divided into two parts. The primary one is fast pressure increase from 3,9 to 4,5 bar, then a secondary, slower pressure increase can be observed from 4,5 to 7,74 bar. The response time of the pressure increase is 3,01 s.
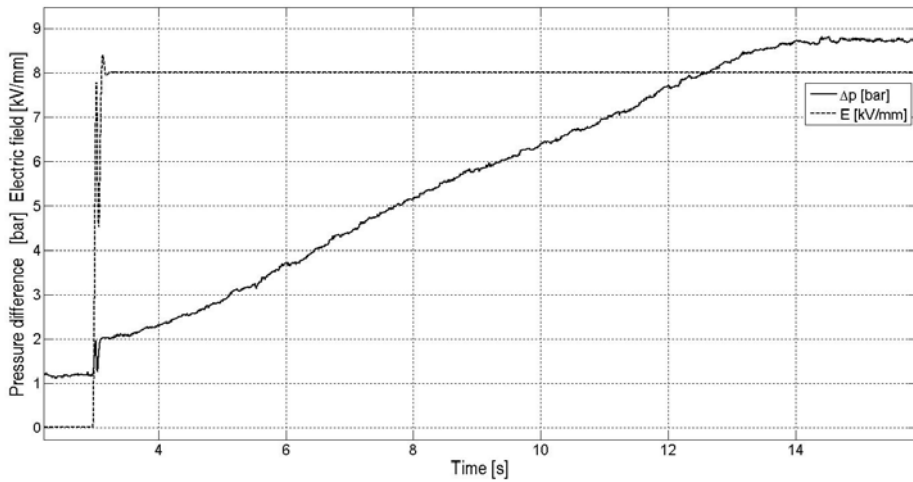
Figure 7. The results of measurement (Flow 0,4 l/min)

Figure 7 also shows the pressure drop in the function of time while the electric field changes from 0 to 8 kV/mm. At this test the flow rate at the ER valve is 0,4 l/min. The response time of the pressure increase is 11,38 s. The value of the pressure increase is 7,64 bar. The maximum pressure drop is 8,76 bar.
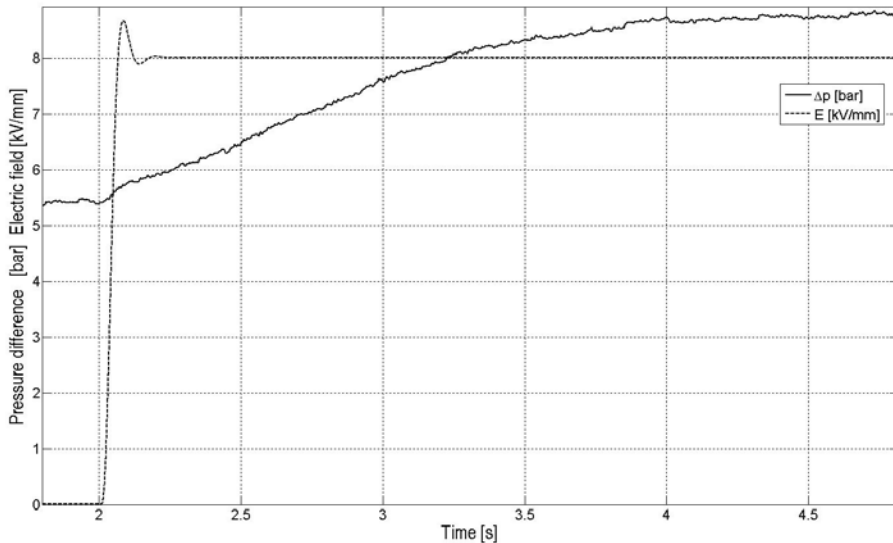
Figure 8. The results of measurement (Flow 2,2 l/min)

At the test that can be seen at figure 8 the flow rate crossing the ER valve is 2,2 l/min. The electric field changes from 0 to 8 kV/mm. The response time of

the pressure increase is 1,98 s. The value of the pressure increase is 3,32 bar. The maximum pressure drop is 8,76 bar.

These tests show that the flow rate has an impact to the response time of the evolving pressure drop. With the increase of the flow rate the response time of the pressure increase falls. The explanation of this phenomenon requires further experiments. The maximum value of the pressure increase depends on the rate of the applied electric field.

5. Conclusions

The test equipment developed is an experimental instrument being fitted into a hydraulic system what enables dynamic measurement of shearing stress of electro-rheological fluid as a function of electric field, oil temperature and particle mass fraction. The electric potential applied between the electrodes effects the change of shearing strengths of the fluid. The measure of changing can be determined unambiguously upon the pressure drop.

On the basis of test results the dynamic behavior model of ER fluid could be built up. On the other hand the instrument capable not only for testing the ER fluids but applying it as a fluid flow controller. As this kind of flow controller valve doesn't contain any moving part and can be controlled by electric field the probability of failure could be radically decreased.

References

1. Csizmadia B. – Nándori E. (szerk.): Modellalkotás, Nemzeti Tankönyvkiadó, Budapest, 2003.

2. Lee H.-G. – Choi S.-B.: Dynamic properties of an ER fluid shear and flow modes, In: Materials and Design, 2002., XXIII. Évf.

3. Monkman. G.J. – The Electro-rheological Effect under Compressive Stress – Journal of Physics D: Applied Physics – Vol. 28, pp 588-593 - Institute of Physics, 1995.

4. Zrínyi M.: Intelligens anyagok, Magyar Tudomány, 1999., 6. sz., 682.

Experimental procedure for evaluation of the structural integrity of threaded API line pipe couplings

Timothy GALLE, Wim DE WAELE,
Patrick DE BAETS, Jeroen VAN WITTENBERGHE

Department of Mechanical Construction and Production,
Laboratory Soete, Ghent University

Abstract

Threaded connections are used throughout the world during the completion of wells to extract oil and gas from distant reservoirs. Due to the extreme depths and working conditions of offshore supplies, the structural integrity of these components is of principal importance.

The standard ISO 13679:2002 describes the experimental procedure to determine the safe working conditions of the coupling. It defines three different kinds of tests required to qualify the coupling: a make-break test, a test load envelope and a failure test.

This paper illustrates the test load envelope procedure applied to a 1" regular API Line Pipe threaded coupling. A pressurized grade B connection is subjected to a cyclic sequence consisting of different internal pressure and axial tension/compression combinations with equal Von Mises Equivalent (VME) stresses within predefined boundaries of the expected working conditions of the coupling. During testing, axial and circumferential strains are measured at several locations on the specimen. Loss of structural integrity results in a reduction of pressure within the pipe. Leak detection is the considered failure criterion throughout the entire test and is an indication for the fitness for use of the coupling under the applied working loads.

Keywords

threaded coupling, test load envelope, structural integrity

1. Introduction

Threaded connections are often used when long strings have to be formed and regularly disassembled when drilling oil and gas wells.

In order to certify newly designed threaded couplings, they have to be subjected to a series of tests to guarantee their performance under service loads. The considered load cases comprise internal and/or external pressure and axial compression or tension. Methods to perform the required tests are described in

the ISO 13679 standard. These regulations specify three different types of tests: make-and-break (M&B), test load-envelope (TLE) and failure-tests. The second type of tests is discussed in this paper.

2. Background

The test specimens used in this work consist of two pins and one box as illustrated in Figure 1. Except for the minimal length of the pin to avoid interference of the clamping, given by equation 1 [1], no geometric restrictions are enforced.

$$L_{\min} = D_0 + 6\sqrt{D_0 t} \tag{1}$$

With D_0 the outer diameter [mm] and t the minimum wall thickness [mm] of the pin.
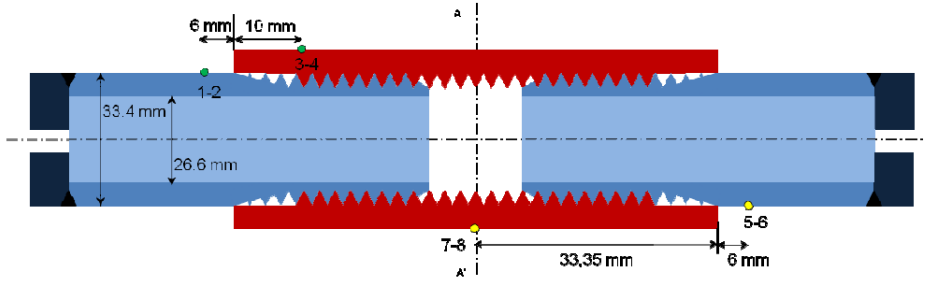
Figure 1. Example of a test specimen consisting of two pins and a box, with indication of the location of installed strain gauges

In addition to the required minimum length of both pins, the geometric tolerances of the threads are considered when assembling the testspecimen, resulting in different thread interferences. When the entire procedure is conducted, 8 different combinations of thread interference should be considered. Generally, the combination of loads to which the threaded connection can be subjected is illustrated by means of a Von Mises Equivalent (VME) diagram (see Figure 2). This diagram illustrates all possible combinations of pressure and axial load that cause a predefined percentage of yield stress in the material, according to the Von Mises yield criterion. When bending loads are not taken into account, the ellipse is calculated in accordance with equation 2.

$$(1-s)*\sigma_{YS} = \sqrt{\sigma_a^2 + \sigma_h^2 + \sigma_r^2 - \sigma_a\sigma_h - \sigma_h\sigma_r - \sigma_r\sigma_a} \tag{2}$$

Where s is a safety factor [%], σ_{YS} the yield strength of the material [MPa], σ_a the axial stresses [MPa], σ_h the hoop stresses [MPa] and σ_r the radial stresses [MPa].

Depending on the combination of the applied loads, the stresses can be calculated as follows:

$$\sigma_a = \frac{F}{A} \tag{3}$$

For internal pressure:

$$\sigma_h = p_i * k_i \tag{4}$$

$$\sigma_r = p_i \tag{5}$$

For external pressure:

$$\sigma_h = p_0 * k_0 \tag{6}$$

$$\sigma_r = 0 \tag{7}$$

The geometric dependent parameters k_0 and k_i are defined by:

$$k_0 = \frac{2D_0{}^2}{D_0{}^2 - \left(D_0 - 2t\right)^2} \tag{8}$$

$$k_i = \frac{D_0{}^2 + \left(D_0 - 2t\right)^2}{D_0{}^2 - \left(D_0 - 2t\right)^2} \tag{9}$$

When a TLE-cycle with a given safety factor (see equation 2) can be completed without failure, it is advisable to reduce this factor in order to determine the actual performance limits of the connection and pipe body. Due to the huge amount of different connection designs and resulting performance, the total amount of points to be tested during one test cannot be mandated. However, the result of a test is only accepted and considered to be reliable when at least 10 points per quadrant are evaluated [2].

Figure 2 gives an example of a VME ellipse for a regular 1" API Line Pipe threaded connection made of Grade B steel with a yield strength of 356 MPa. Using a 42% safety factor, 6 different load points are tested in the first and second quadrant.
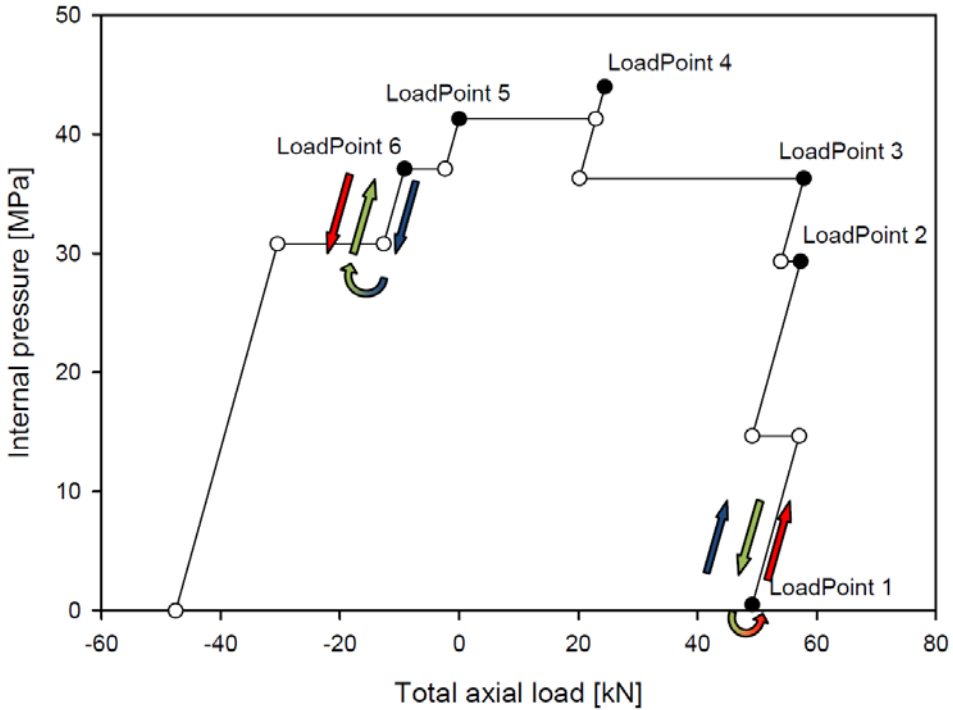
Figure 2. Example of a TLE ellipse for a Grade B steel, 1" API Line Pipe threaded connection with indication of the 6 points which were tested.
The arrows indicate the direction of the load cycles

3. Experimental setup

When internal pressure is applied, additional axial tension is created on the end caps of the specimen (see Figure 1). Due to this interaction, formula 10 is used to transform the theoretically calculated axial forces into the required axial force to be applied by the tensile machine. Herein, F_a is the applicable axial force [kN], F_t the theoretical force [kN], p_i the internal pressure [MPa] and D the inner diameter of the pin [mm].

$$F_a = F_t - \frac{p_i * D^2 \pi / 4}{1000} \tag{10}$$

Figure 2 shows the actual load path and the conditions which should be used as input for the force controlled tensile machine conducting the test in order to match the theoretical TLE from Figure 1.

Each load point is tested three times. To increase the reliability of the test, the load history is changed by following the cyclic path through the ellipse in

different directions. At first, in counterclockwise (CCW) direction, load points 1 through 6 are assessed as given in Figure 1. Secondly, the direction is reversed and when load point 1 is reached, a final reverse in CCW direction takes place and the test is stopped at point 6.

During the entire test, axial and hoop strains are recorded at 4 different locations (Figure 3) and are given in Figure 4 for each load point.

A remarkable behavior of the connection was observed during the beginning of the test, at load point 1. For symmetry reasons, strains 2 and 6 should be equal in magnitude and trend. However, from Figure 4 it is visible that at load point 1 the lower pin is in compression and the upper pin is in tension. After that, the trend of both strains is similar.

This behavior may have been caused by an initial misalignment of the coupling. Figure 5 indicates that during the first 200 seconds, the coupling is being aligned by introducing a bending moment in the vicinity of the box. This taken into account, strains 2 and 6 behave similar with exception of the initial offset caused by misalignment.
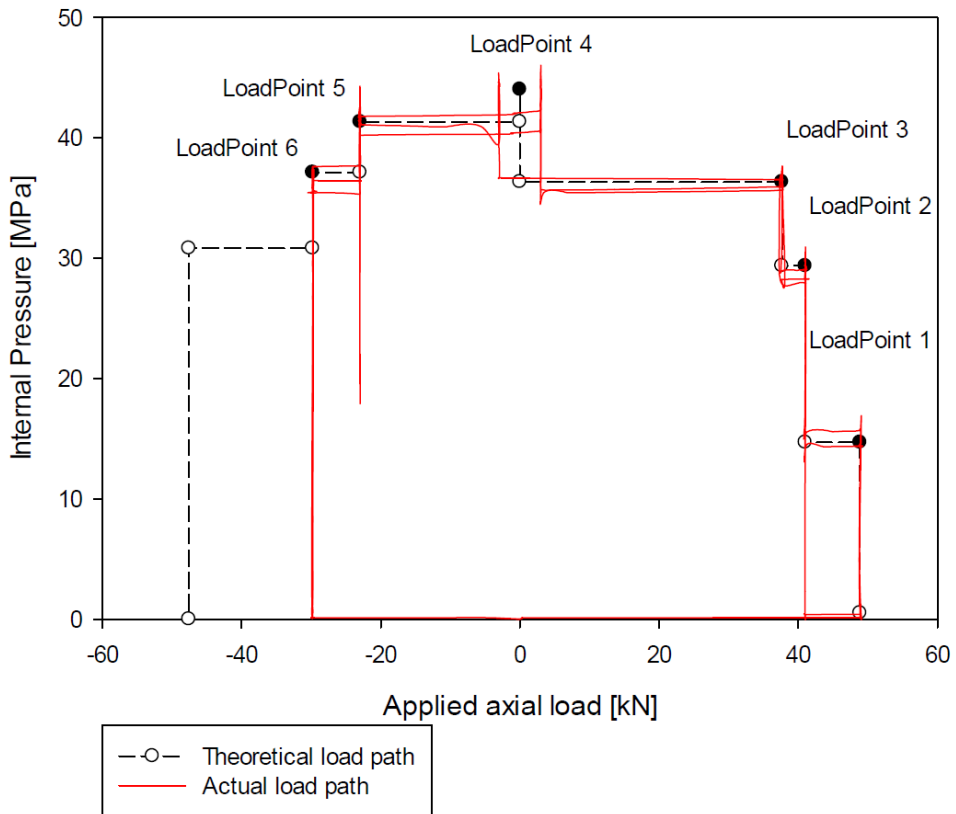
Figure 3. Example of the modified TLE ellipse together with
the actual load path applied during the test.
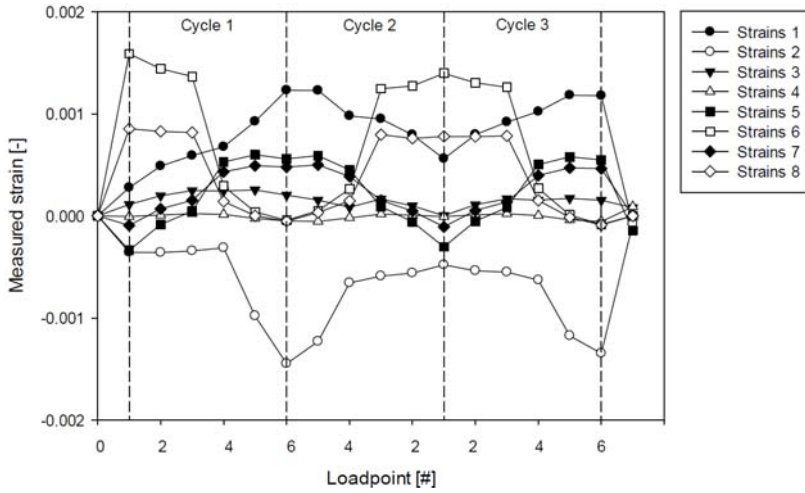
Figure 4. Overview of the measured strains during the TLE-test.
(Cycle 1: Point 1 through 6, cycle 2: point 6 through 1 and cycle 3: point 1 through 6)
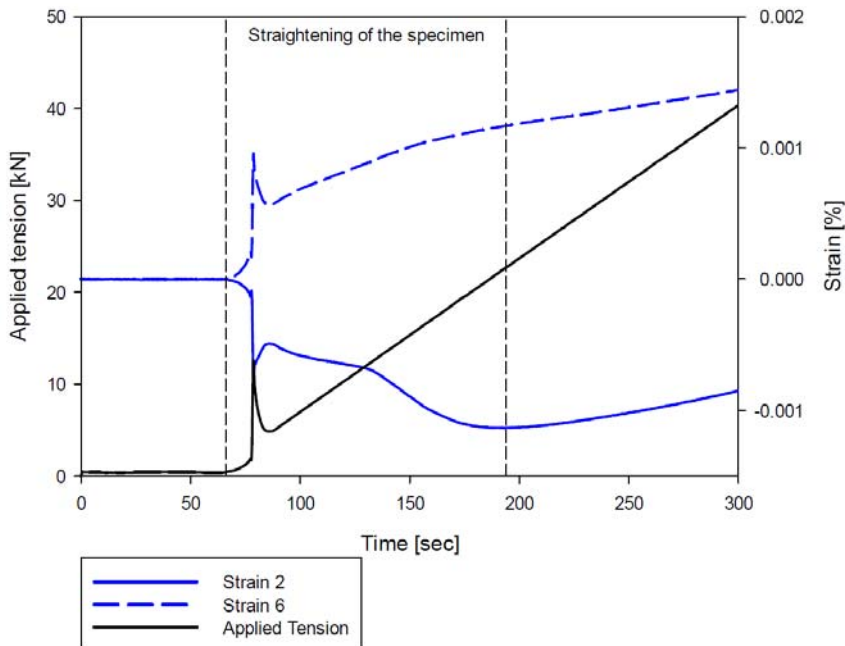
Figure 5. Measured strains 2 and 6, together with the applied tensile loads
during the first 5 minutes of the test.

Noteworthy is the abrupt change in applied force and measured strain when the specimen starts to elastically deform at 80 seconds. When tension is applied, shear stresses at the thread flanks can cause the coupling to move and adapt to the current loads. The overshoot in the applied tensile force by the machine can

be explained by the sudden movement of the coupling caused by initial play between the flanks of pin and box.

Furthermore, strain 4 appears to be less sensitive to any of the applied load combinations. This indicates that the used strain gauges are not on top of the last engaged thread but to the left of their intended position. The recess of the connection does not undergo any deformation caused by the axial tension or compression and due to the absence of the supporting pin; the hoop stresses are drastically reduced.

4. Conclusion

When conducting tests as described in standards such as the ISO 13679:2002 for testing threaded couplings, misalignment and initial play between the threads of the investigated connection must be considered to interpret the measured strains.

In order to better understand the initial bending behavior, it is advised to measure the misalignment before starting the test and to use multiple strain gauges at the same section, shifted with a 90 degree angle.

References

1. API RP 5C5, Recommended Practice for Evaluation Procedures for Casing and Tubing Connections, second edition, American Petroleum Institute, 1996

2. ISO 13679, Petroleum and natural gas industries – Procedures for testing casing and tubing connections, first edition, 2002

Management of spare pieces for worn out PG 80 using Pareto method

Nicolae UNGUREANU, Radu COTEȚIU, Otto EBERST

North University of Baia Mare Department of Industrial Systems
and Management of Technology, Baia Mare, Romania

Abstract

The paper's aim is to fix the priorities in supply activities with spare parts for drilling machine PG-80. For this we use the Pareto Method (ABC Diagram) applied to statistic registered in Ore Mining Baia Sprie.

Keyywords

spare part, failure, Pareto, drilling machine

1. Introduction

The supply activities with spare parts are one of essential activities in the maintenance of the equipments and machines. Without a systemic and prompt supply activity the entire production activity can be disturbed. Another aspect is the determination of the pieces with accelerate rate of failure. These for establish the order in bringing the spare parts and for study the causes of low reliability of these pieces.

Are many techniques for management of stocks, but the most used are the Pareto Method (ABC diagram) and the method based to apportionment on the calculus basis for the component pieces in three classes:

- pieces with fast speed of wear;
- pieces with medium speed of wear;
- pieces with low speed of wear.

The last case is used in manufacturing plant with specialists in wear calculus and with laboratories trained for these activities.

The first case is easy to apply, even by users, the requirements are: the know-how about the method and a data base concerning the equipment for witch the research is required.

2. The application of Pareto Method on the drilling machine PG-80

As part of the exploitation of useful mineral substances the operation of drilling occupy a particular place due to the great expenses (energy, time, and physical effort). Directly dependent on these are both the drilling equipment performances and the drilling tools performances.

The drilling machine PG-80 (fig. 1) is a mining equipment custom built for drilling the mining hole, parts of mining technology "drilling-explosion".
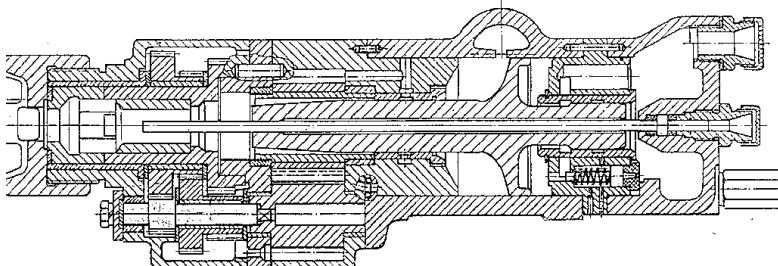
Figure 1. Drilling machine PG-80

The drilling machine PG-80 is a heavy roto-percussion type. Together with P-90W attaining 70-80% from the entire drilling equipment.

The Pareto method apportionment the spare pieces in three classes:
  A. low number of pieces (ca. 20%) with high influence to reliability (ca. 80%);
  B. medium number of pieces (ca. 30%) with medium influence to reliability (ca.15%);
  C. high number of pieces (ca. 50%) with low influence to reliability (ca. 5%).

Table 1.

Number order	Name of piece	Piece replace 1995	related to one 1996	air-feed drill total
1	Cylindric body	0	0	0
2	Pin I	10	12	22
3	Engine case	0	0	0
4	Bushing guide piston	3	1	4
5	Piston	1	1	2
6	Distribuitor	0	0	0
7	Pin II	0	0	0
8	Valve	0	1	1
9	Tightening washer I	1	1	2
10	Tightening washer II	0	0	0
11	Water charging pipe	18	14	32
12	Chuck collet	2	2	4
13	Joint air-water	2	0	2
14	Bushed bearing I	14	12	26
15	Engine pinion	2	1	3
16	Bushing bolster up	1	2	3
17	Bushed bearing II	2	1	3
18	Drive gear	2	1	3
19	Intermediate plate	11	14	25
20	Gear	2	2	4
21	Bushing cylindrical drill	12	13	25
22	Double gear	1	2	3
23	Bushed bearing III	1	3	4
24	Bushed bearing IV	1	1	2
25	Pinion	1	0	1
	SUM			171

The database is built for the case of Ore Mining Baia Sprie and covered two years (1995, 1996).

Table 2.

Number order	Name of piece	%	% additive
11	Water charging pipe	18,7134	18,7134
14	Bushed bearing I	15,2046	33,918
19	Intermediate plate	14,6198	48,5378
21	Bushing cylindrical drill	14,6198	63,1576
2	Pin I	12,8655	76,0231
4	Bushing guide piston	2,3391	78,3622
12	Chuck collet	2,3391	80,7013
20	Gear	2,3391	83,0404
23	Bushed bearing III	2,3391	85,3795
15	Engine pinion	1,7543	87,1338
16	Bushing bolster up	1,7543	88,8881
17	Bushed bearing II	1,7543	90,6424
18	Drive gear	1,7543	92,3967
20	Gear	1,7543	94,151
5	Piston	1,1695	95,3205
9	Tightening washer I	1,1695	96,49
13	Joint air-water	1,1695	97,6595
24	Bushed bearing IV	1,1695	98,829
8	Valve	0,5847	99,4137
25	Pinion	0,5847	99,9984
1	Cylindric body	0	99,9984
3	Engine case	0	99,9984
6	Distribuitor	0	99,9984
7	Pin II	0	99,9984
10	Tightening washer II	0	99,9984
	SUM	99,9984	

$$y = 7E{-}06x^6 - 0{,}0004x^5 + 0{,}0082x^4 + 0{,}0236x^3 - 2{,}3013x^2 + 25{,}691x - 6{,}4074$$
$$R^2 = 0{,}9958$$
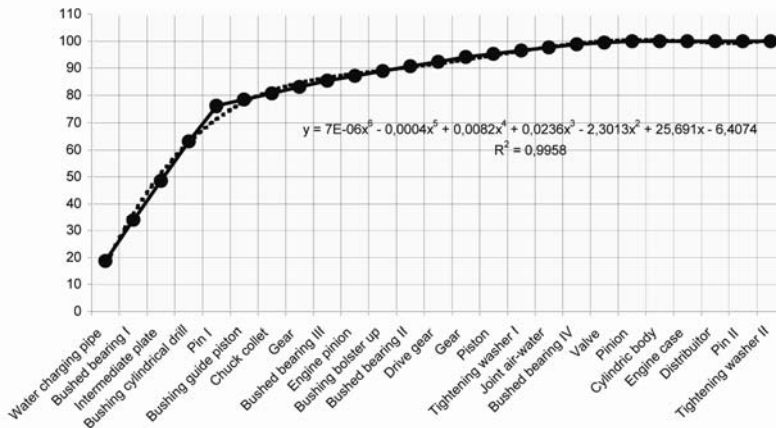
Figure 2. The Pareto curve

The table 1 presents the components elements of drilling machine PG-80 and the number of pieces replaced in 1995-1996. This number is average for 35 drilling machine PG-80 in function.

The results of calculus are represented in table 2. It's the presentation of the pieces ordered by the number of failure and implicit the percent.

3. Conclusion

The calculus and the graphic representation of database show the concordance between the theory and the practice:

Class	Number of pieces	Percent
A	5	76.023
B	8	16.373
C	12	7.604

The next step is to study each pieces from A class to eliminate the failure causes (from design work, from manufacturing of from bad utilization).

References

1. Ceauşu I. – Terotehnica şi terotehnologia, Editura Tehnică, Bucureşti, 1989

2. PG-80 – Technical book, UUMR- Baia Mare

The impacts of mechanical pre-treatment of metal armatures on the strength of the rubber-to-metal bonding

Tamás RENNER, Lajos PÉK, Róbert KERESZTES

Institute for Mechanical Engineering Technology,
Faculty of Mechanical Engineering, Szent István University

Abstract

During the course of our work we have been studying the conditions of establishing a rubber-to-metal bonding. To achieve this, we have carried out rheological tests to determine the feature curves of the mixtures that can be used to establish the bond, as well as the details of the mechanical metal pre-treatment. we have compared the impact of widely used materials and the resulting surface roughness on tear strength. we have planned and produced a test tool to create the samples using different methods.

Keywords

steel rubber bonding, surface, roughness, surface treatment

1. Introduction

Mechanical units used by contemporary mechanical and automotive industries require that they should operate at a high technical quality, without any faults for a rather long time. This can only be achieved if all items are produced according to best practice technical standards which are already in place at the planning stage. To combine the two physically rather different materials – steel and rubber – into a single mechanical element, it is necessary to establish a purposefully planned bonding system.

   Our research is about studying the conditions of establishing a rubber-to-metal bonding. First we compared the physical, mechanical and rheological features of the most important elastomers which are widely used in practice. Then we examined the possibilities of the pre-treatment of metal armatures and the effects of the differences. We also applied imaging analyses to understand processes taking place at the boundary. To describe the morphology, we used electronic-microscopic images, while to create the one and two dimensional lateral item map, we used characteristic X-ray emission images. We were looking for relation between inner tool pressure and the strength of the resulting bond when using compression technology. In the future we will also examine the same using molding technology; the results of this will be discussed in a later study.

2. Rubber-to-metal bonding

When industrially producing vibration absorbing rubber products and other rubber-metal parts, there is a chemically produced bonding material that realizes the bonding between the vulcanized rubber and the metal armatures. The process consists of degreasing the metal parts and then the mechanical pre-treatment which is dependant on the metal material – it can be done through spraying either corundium or steel grits. The bonding strength is influenced by not only processing the glue according to the technology, but also by the rubber mixture. Bonding of the mixture is highly dependant on its hardness and on the type of the elastomer as well. we have used a general rubber mixture from 55 Sh° natural rubber for my measurements.

3. Measurement results

During our research we first determined the rheological feature curves which make a specific mixture sufficient for establishing rubber-to-metal bonding.

Figure 1 represents the rheological figures of the NR-based mixtures studied. We have carried out the measurements with an S 100 Monsanto Rheometer. Chart 1 shows the curves produced by this equipment.

Colors used: blue: 43 Sh°; red: 57 Sh°; green: 72 Sh°, 170°C, 6 min

The approach for the evaluation is as follows: 0 is assigned to the moment curve minimum, maximum is assigned to its maximum. As the maximum point is difficult to define, it is a widely used practice that 90% from the moment curve minimum (t_{90}) is regarded as the vulcanization time of the material (according to measurements the same is the maximum of the tear strengths). The 20% increase from the minimum is represented as t_{02}. The significant values from the curves can be seen in Table 1, from which the vulcanization time and the ability for rubber-to-metal bonding can be determined.
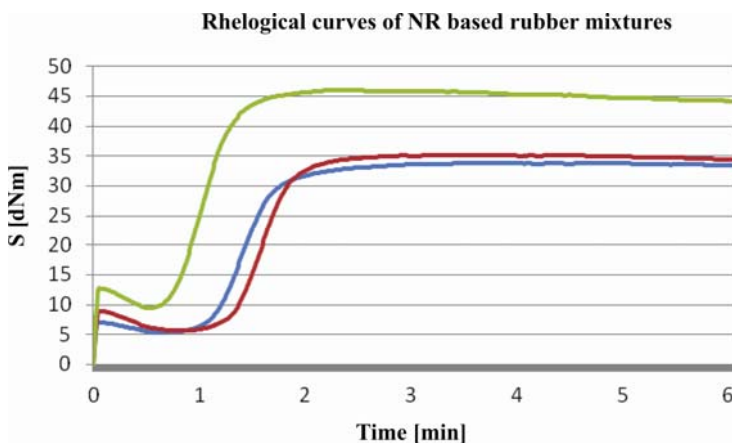
Figure 1. Rheological curves

Table 1. Significant values of the the rheological curves

Mixture	S_{min}	S_{max}	t_{02}	t_{90}
NR 43 Sh^0	5,98	33,7	0,95	1,96
NR 57 Sh^0	7,41	37,14	0,9	1,77
NR 72 Sh^0	8,63	41,36	0,81	1,62

The effects of the mechanical pre-treatment of the metal armatures were analyzed through spraying tests. We used the following specimen (Figure 2.) for the experiments applying a properly designed tool (Figure 3.).
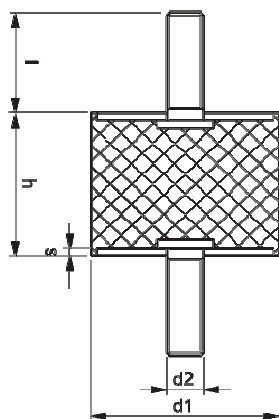
d_1=25mm
h=20mm
s=2mm
l=18mm
d_2=M6

Figure 2. Test specimen

Figure 3. Test specimen vulcanizing tool

The most important aspect of the experiment was to create different surface roughness values using different spraying materials and different spraying times; calculating an average surface rou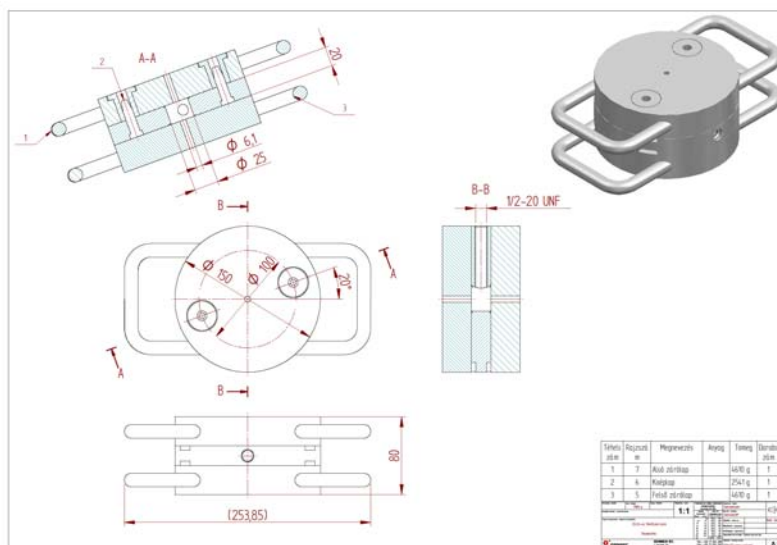ghness, and then treating the metal armatories with adhesives and vulcanizing the sheet specimens. The spraying material was S170 steel grits at first, and then corundium. Figure 4. shows the tensile results in the function of surface spraying time using steel grits, furthermore Figure 5. presents the same in case of corundium spraying. The micro-topography created by the spraying materials can be seen on Figures 6 and 7.

Table 2. Parameters of the test:

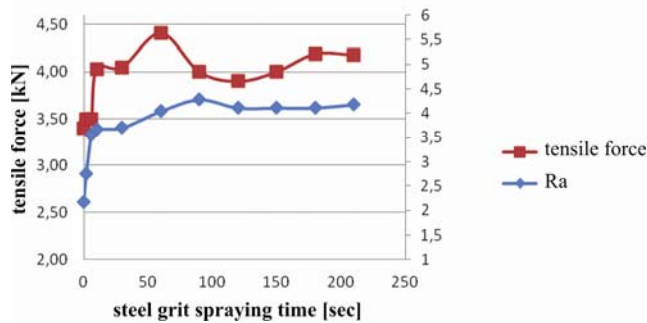| Type of the tensile test machine	LLOYD LR 300
Breaking Rate [mm/min]	500
Sheet Specimen [mm]	25/20-1 M6x18
Ambient Temperature [$^\circ$ C]	23
Relative humidity [%]	40

Figure 4. Tensile force and Ra Roughness in relation to spraying time using steel grits
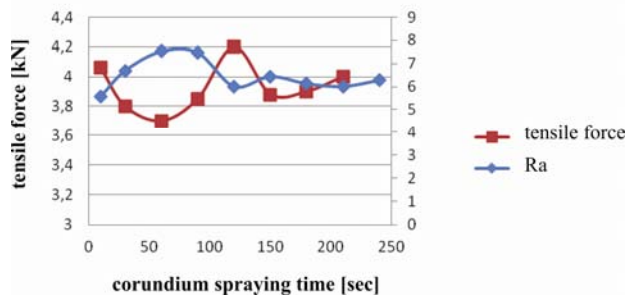
Figure 5. Tensile force and Ra roughness in relation to spraying time using corundium
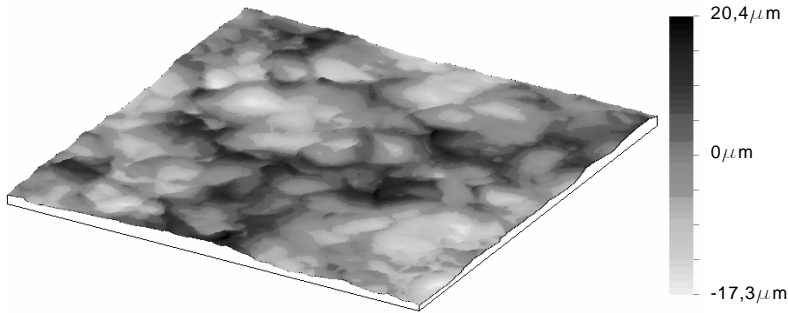
Figure 6. The impact of steel grits on the surface
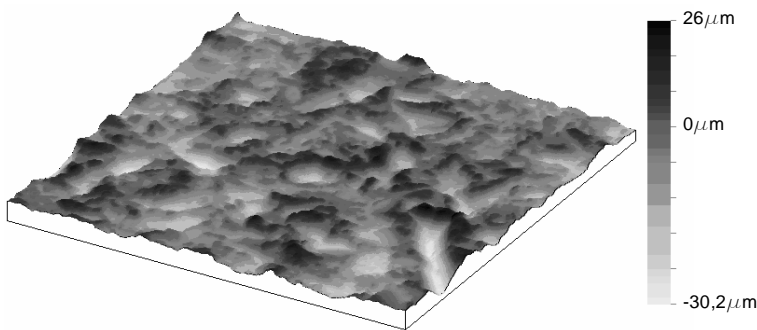
Figure 7. The impact of corundium on the surface

4. Conclusions

– After analyzing the Monsanto-curves, it can be seen that mixtures with a firm induction phase and a long, steady process are the most ideal for establishing the metal bonding. The value t_{02} has to be at least 0.8 min., otherwise the absorption ability of the bonding system significantly decreases due to the early vulcanization of the rubber which in turn weakens the strength of the bond.

– It can be seen from the results of the experiments regarding the pre-treatment of mechanical armature that the Ra average surface roughness is insufficient in determining the strength of the rubber-to-metal bond. This is because there is no clear connection between spreading time (thus dynamic surface roughness) and the adhesion strength of the bond.

References

1. Dr. Bartha Zoltán: Gumiipari kézikönyv. TAURUS-OMIKK, Budapest, 1988

2. Dr. Pék Lajos: Anyagszerkezettan és anyagismeret. Dinasztia Kiadó, Budapest, 2000

3. A. Springer: Gumi technológia. Műszaki Könyvkiadó, 1957.

4. www.gak.de

5. www.plastverarbeiter.de

6. Műanyag és Gumi. 44.évfolyam 6.szám 260p.

Development of new PA6 composites

[1]Mátyás ANDÓ, [2]Jacob SUKUMARAN,
[2]Vanessa RODRIGUEZ, [3]Patric NEIS, [1]Gábor KALÁCSKA,
[4]Tibor CZIGANY, [2]Patrick DE BEATS

[1]Institute for Mechanical Engineering Technology,
Faculty of Mechanical Engineering, Szent István University

[2]Department of Mechanical Construction and Production, Laboratory Soete, Ghent University

[3]Universidade Federal do Rio Grande do Sul, – UFRGS, Rua Sarmento Leite, Brazil

[4]PT, Budapest University of Technology and Economics, Hungary Budapest

Abstract

Among the large number of engineering polymers the cast polyamide 6 material has special attention in the field of semi-finished structural materials (rods, plates, tubes) due to good mechanical and tribological properties. According to the industrial needs the development of different special properties like greater abrasive resistance, ESD characteristics, better flame-proofing or increased toughness is vital. To identify these properties on different polymer composites (based on PA6), we have carried out more than 2800 standard tensile, flexural, Charpy-impact and Shore-D hardness test, we have produced SEM pictures and we have determined surface resistivity, abrasive tribological properties and carried out flammability tests. As a result of this the optimal quantities of additives: 3wt% graphite, 3wt% conductive graphite, 1wt% conductive carbon black, and 10wt% and 15w% softening material.

Keywords

polyamide 6, mechanical properties, tribological properties, electric behaviour, effect of different additives

1. Introduction

Plastics are used in more and more wide range since their appearance. Due to recent developments, they are not only used in inferior fields like packaging, but are also used as load carrying mechanical parts.

One of the most often used engineering plastic is the polyamide 6 (PA6) because of its quite good mechanical (strength, hardness, toughness, damping) and tribological (sliding, wearing resistance) characteristics [1]. Due to this, it is also used as bearing bushes, wearing laths, different pulleys, gears etc...

During a former Hungarian research, the industrial product technology of magnesium catalyzed cast PA6 semi-finished products (rods, plates) was worked out. This method has several benefits contrary to the commonly used natrium catalyzed product. The magnesium catalyzed PA6 has a more homogeneous structure with a higher crystallizing factor, and has less remaining monomer

content. The impact strength is higher and the abrasion wear resistance is better than the natrium (sodium) catalyzed PA6 [2, 3].

The use of tougher cast polyamide 6 materials is especially advisable on those areas where the working environment differs from usual. For example the agricultural machinery, where the agricultural works are often accompanied with extreme conditions, the impacts should be beared by the applied materials. Essential property is the abrasive wear resistance, where the possible improvement is typically responsible for increasing of part's lifetime (e.g. protecting cover, chute) [4-6]. The use of antistatic or fire-resistant plastics is crucial under danger of explosion (grain silos, transport system of fertilizers).

Using of improved polymer machine parts is important both from agrotechnical and environmental protection point of view. These parts play important role at the reduction of weight- fuel consumption- and the emission of harmful materials of agricultural machines, at the reduction of soil compression and for the ground water balance.

The aim of the research is the further improvement and examination of magnesium catalyzed cast PA6 composite semi-finished products, which enables the wider range of use in agricultural systems. The following improvement areas were determined accordingly:
  – improved toughness
  – improved abrasive wear resistance
  – antistatics characteristics
  – improved fire resistance.

The targeted features should be reached without significant change of the original mechanical properties of the natural base material. In that case the range of use can be increased (universality), which may cause a real market advantage.

The improved material characteristics can be reached with different additives, because of the below points are among the aims of the research:
  – determining which additives are efficient for influencing the characteristics
  – detailed examination on the effects with the selected additives depending on their quantity used in the base matrix
  – complex evaluation of the recipes and their qualifications on the basis of ambitions – material characteristics.

2. Material and Method

For material development the magnesium catalyzed cast polyamide 6 (PA6) was chosen. By using the pre-research results of composite production (where 39 additives were examined), a research plan was made. The aim was to get to know the exact effects of the selected additives. During the selection of the additives the mechanical and special characteristics, the easy adaptability to the industrial casting technology (the basis of practical use of the research) and the contradictions in the literature and the personal experiences were taken into consideration. The selected additives are shown in Table 1.

Table 1. Additives selected for research plan

Additives	Content [%]				
Softening material	10	15	20	25	
MoS$_2$	2	3			
Graphite	1.5	2	2.5	3	3.5
Montmorillonite	0.5	1	3	6	
Conductive graphite	0.5	1	2	3	4
Conductive carbon black	0.5	1	1.5	2	2.5

The following examinations were made on new, composite sample materials:
– Tensile-test (MSZ EN ISO 527)
– Flexural-test (MSZ EN ISO 178)
– Charpy impact-test (MSZ EN ISO 179)
– Hardness-test (MSZ EN ISO 868)
– SEM microscopic examination on broken surface of impact-test
– Abrasive tribological test (DIN 50322)
– Surface resistivity measurement (IEC 60093)
– Plastics flammability test (UL-94)

3. Results

In this chapter the measured results are summarised, and the effects of additives are evaluated.

Montmorillonite additive
The montmorillonite was selected, because several articles wrote about its use as fire resistant additive in case of polyamides. These articles did not take into consideration that the polyamide 6 under real flaming circumstances burns with dropping, therefore the montmorrilonite's decreasing effect for burn intensity does not predominate (Table 2).

Table 2. Burning characteristics of samples containing montmorillonite

Montmorillonite content [%]	Group sign	Comment
0	HB	Drops every 2 seconds
0.5	HB	Drops every 2 seconds
1	HB	Drops every 2 seconds, 16.4 mm/min
3	HB	Drops every 2 seconds, 16 mm/min
6	HB	Drops rarely, 14.8 mm/min

On the basis of the measured results, it is stated that the montmorrilonite content spoils the fire resistant characteristics of pure material, therefore the

additive did not achieve its aim. From the surface resistivity measurements it also can be determined that montmorrilonite results higher surface resistivity for the sample, so it does not help to reach better antistatic behavior. The only improvement was in the abrasion resistance of 6% sample, which results 33% lifetime increase compared to the base material. At this additive quantity, depending on the weighting, mechanical characteristics decrease with 3-9%. On the basis of reached results, the production of new market product containing montmorrilonite is rejected.

Softening material

The first aim of using softening materials is to change the mechanical characteristics, mainly to increase the impact strength of material. During casting, it became clear that the 25% additive content is more than what the base material can take up, therefore visible segregation arose. The mechanical characteristics of this sample (eg. Young's modulus, tensile strength…) significantly decreased, moreover, at burning test it showed weak characteristics. In case of 20% additive content the microscopic examinations proved (typical fracture surface) the assumption drawn from mechanical characteristics, that the two-phased system already appears at this additive content (Figure 1).
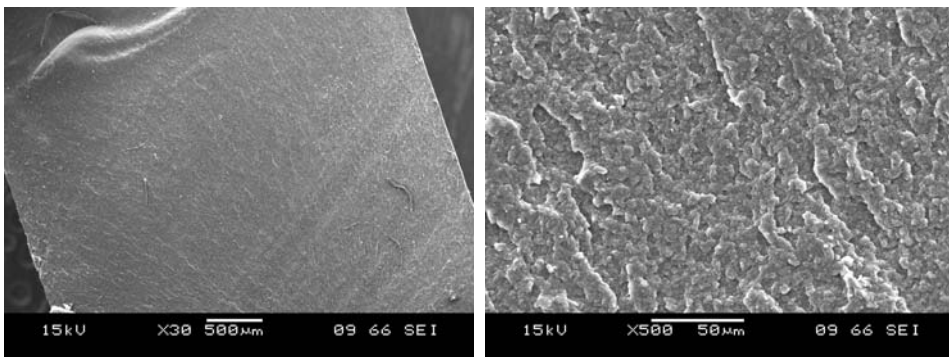
Figure 1. 30× and 500× enlarged SEM picture of 20% softening material

At 15% additive content, 3 times higher impact strength could be reached (Figure 2). Together with this the Young's modulus (with 40%) and the tensile strength (with 50%) decreased. It also could be noticed that the surface resistivity decreased to 10^{10} Ω, so a system with good antistatic characteristics was produced. Due to the decrease of Young's modulus, the abrasive wear intensity doubled. Its general use in abrasive tribological systems is not recommended, but due to its Shore-D hardness decrease (12%) it could be good in such tribological systems, where the particle embedding capability of the surface has a fundamental importance.

148

In case of 10% additive, the characteristics of sample change similar as in case of 15% additives, but these changes are smaller. In case of the 10% additive, the sample's characteristics are closer to the pure material characteristics. Its impact strength is 70% higher, but its tensile strength decreased with 13%. Antistatic characteristic was not improved by the 10% additive, and the abrasive wear intensity was also raised by 33%. The burning characteristics declined both in case of 10 and 15% additive.

On the basis of the result, the new market product containing softening material can be produced. In case of 10% additive, one should count with better impact strength but worse abrasive wear resistance and burn characteristics. In case of 15% additive, a much better impact strength and antistatic characteristics are obtained, but other mechanical, burn and abrasive tribological properties are worse.
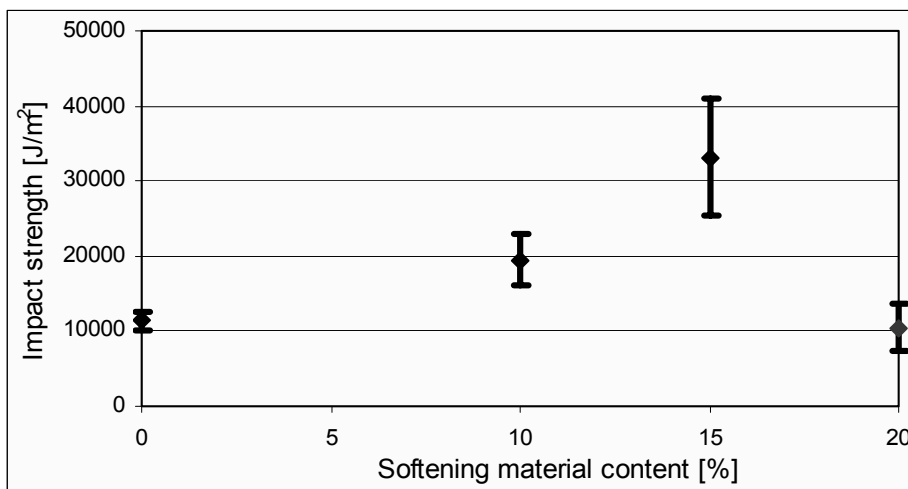

Figure 2. The specific impact strength of samples containing softening materials

Graphite additive

Graphite was chosen because it improves the tribological and electrical characteristics. According to this, the abrasive wear intensity decreases with 25%. (Figure 3). The electrical characteristics are improved by the increase of additive content. In case of 2.5% graphite content, a cast polyamide 6 was produced having good antistatic properties. By adding further additive the upper limit of ESD characteristic can be reached (surface resistivity with a order of magnitude more than 10^9 Ω). The tensile strength decreased with 10-15%, the impact strength decreases with 15-25%, but the Young's modulus of flexure increases with 5-15%. This means at the summarized mechanical characteristics a decrease of 5-8%. The graphite additive beyond the improvement of electric

and tribological characteristics, it improved the fire resistance as well, namely the originally HB rated cast polyamide 6, these materials obtained the V-2 rating, which is higher by one step.
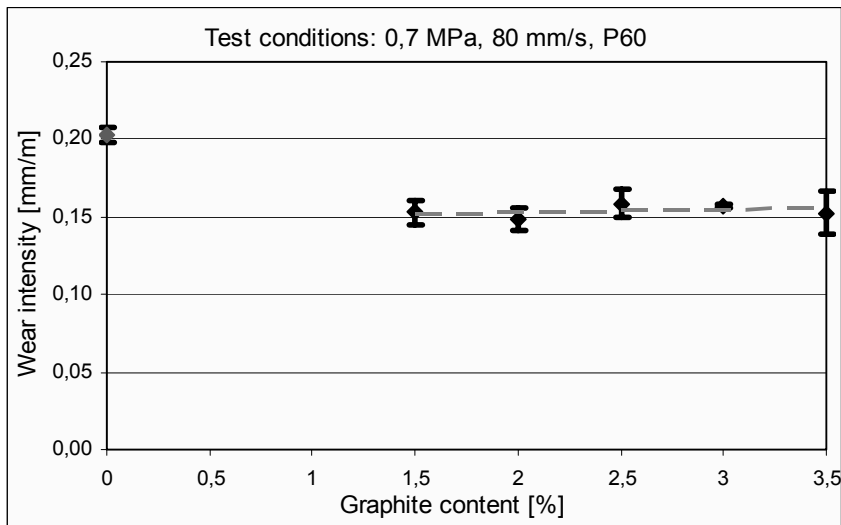

Figure 3. Abrasive wear intensity of samples containing graphite

On the basis of the examinations, in case of 3% adding, ESD characteristics, improved abrasive wear resistance and fire resistance is obtained, whilst the mechanical characteristics decrease is restrained. Due to the improved characteristics, this product is considered to be a successful development.

Conductive graphite additive
The conductive graphite was selected as it showed quite good electric characteristics during pre-tests. According to my examinations, the 3% and 4% sample in normal and wet state has a very low surface resistivity (10^7 Ω magnitude), therefore these materials belong to the ESD group. In dry condition their surface resistance a little bit bigger (10^9 Ω magnitude), so, in this case they also have ESD characteristics.

The conductive graphite does not change significantly the tribological characteristics, so in practical point of view it does not cause better abrasive wear resistance. According to the flammability test, in case of little additive content (0.5-1%) it improves, in case of bigger additive content it does not worsen the burning resistance characteristics. Comparing to the graphite, the tensile strength of the samples is reduced in a smaller volume (5-10%) and beside the Young's modulus of flexure, the Young's modulus of tensile also improves (5-10%) (Figure 4). Therefore in the summarized mechanical characteristics only 2-6% decrease occurs. Due to the outstanding electric

characteristics reached, the sample containing 3% conductive graphite is also considered to be a successful development.
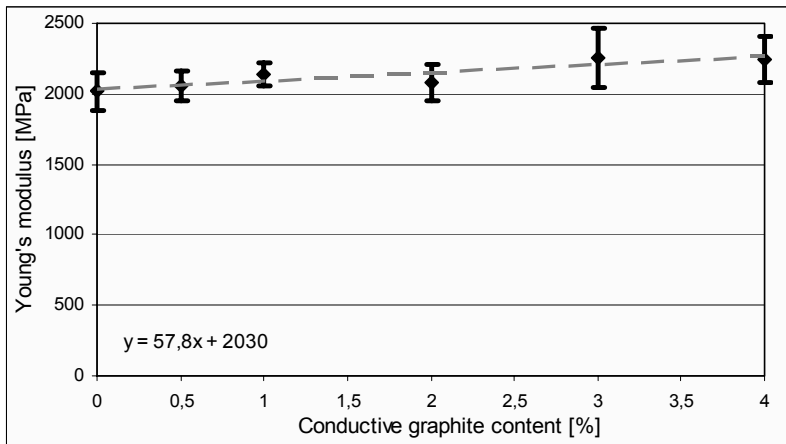
Figure 4. The Young's modulus of conductive graphite

Conductive carbon black additive
The conductive carbon black was selected also due to the improvement of electric characteristics. 1% additive is enough to receive a material with ESD characteristics in normal and wet state (Figure 5).
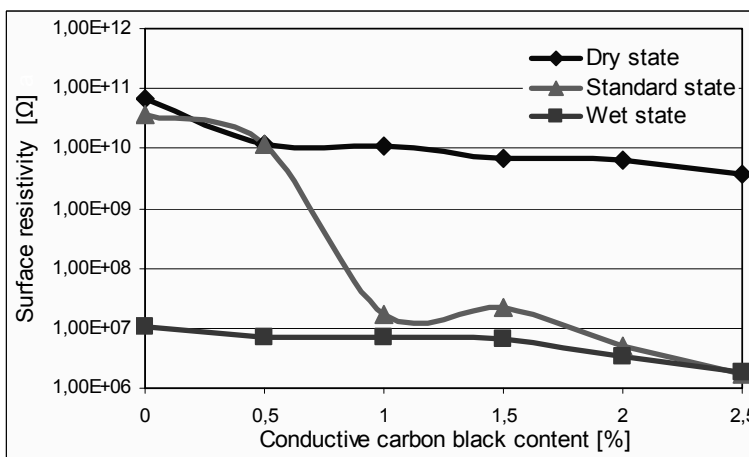
Figure 5. Surface resustance of samples containing conductive carbon.

This is advantageous also, because in case of 1% additive, the mechanical characteristics rarely change (0-1%). The Young's modulus of the sample

increased (6-7%), while its impact strength decreased (10%). The tribological characteristics were not modified significantly by this additive – just like as it at conductive graphite. The fire resistance however got worse within category HB, these samples do not burn out by themselves. On the basis of the excellent electric characteristics and the low proportion mechanical change of characteristics reached with a minimal additive, the development having 1% carbon is considered to be successful.

Molybdenum-disulfide additive

The molybdenum-disulfide was selected as it improves tribological characteristics by a little proportion of additive as well. However in abrasive environment, there was no sign of significantly improved wear resistance, therefore it do not fulfill its prime goal. According to the tests, it has no significant effect on electric characteristics as well. The Young's moduluses increased by 10-10%, but the impact strength decreased with 20%. On the basis of the flammability tests, the material can be ranked to the V-2 category. According to the test system set, the adding of molybdenum-disulfide is not practical as graphite makes better characteristics.

4. Conclusions

As a result of the successful material development process, we have chosen 5 receipts, which enables the magnesium catalyzed polyamide 6 for agricultural machinery use:
- 3% graphite,
- 3% conductive graphite,
- 1% conductive carbon black,
- 10% softening material,
- 15% softening material.

    Based on the results of the research, the production and sales of magnesium catalyzed polyamide 6 containing graphite and conductive carbon black started.

5. Summary

Based on the survey of technical literature we have identified 35 additives used at injection molding and at natrium (sodium) catalyzed cast polyamide 6 to change certain characteristic. These materials would be suitable to reach the following goals mainly characterizing agricultural engineering practice:
- better tribological properties – greater abrasive resistance,
- improved electrical properties – antistatic or ESD characteristics
- better flame-proofing,
- improved mechanical properties – increased toughness,

    The main task was to select the efficient additives and work out the procedure (for example dispersing) needed to carry out the preliminary tests together with the production-developing company with the additives selected. We have

selected from these those additives which are capable to produce suitable composites with magnesium catalyzed cast polyamide 6 base material. Based on preliminary tests We have identified six additives to be used efficiently (softening material, molybdenum-disulfide, graphite, montmorillonite, conductive graphite and carbon black).

We have worked out a complex material-testing and evaluation system according to as an aim set. Based on the system it can be determined whether an additive results suitable structural material for industrial requirements. We have set up an experimental plan being familiar with technical literature, the additives selected and the experimental system, which is suitable to determine the optical quantity of additives selected. We have machined out standard specimens from the cast composite box as a next step. Then we have carried out more than 2800 standard tensile, flexural, Charpy-impact and Shore-D hardness test, we have produced SEM pictures and we have determined surface resistivity, abrasive tribological properties and carried out flammability tests.

We have elaborated the measurement results by statistical methods then (for example: Young's tensile modulus, formation in the function of the softening material content) which were unknown previously in case of using magnesium catalyzed, cast polyamide 6. Parallel with this we have also discovered the causes of changes following the effects of additives.

We have evaluated the effects of certain additives taking into account more aspect based on the experimental system worked out. As a result of this we have determined the optimal quantities of additives in experimental circumstances given, which are the following: 3wt% graphite, 3 wt% conductive graphite, 1wt% conductive carbon black, and 10 wt% and 15w% softening material.

References

1. Bruyne D.: ERTA Engineering Plastics. 3P Engineering Workshop. Seminar booklet. Tielt, Belgium (1998).

2. DOCAMID (PA-Polyamide) properties
http://www.quattroplast.hu/files/file/B_kategoria.pdf

3. Kohan M.I: Nylon plastics handbook. Hanser Publishers, 1995

4. Zsidai L., De Baets P., Samyn P., Kalacska G., Van Peteghem A. P., Van Parys F.: The tribological behaviour of engineering plastics during sliding friction investigated with small-scale specimens. Wear, 253 (5-6), p. 673-688 (2002).

5. Van De Velde F., De Baets P.: The friction and wear behaviour of polyamide 6 sliding against steel at low velocity under very high contact pressures. Wear, 209 (1-2), p.106-114 (1997).

6. Mergler Y.J., Huis in 't Veld A.J.: Micro-abrasive wear of semi-crystalline polymers. Tribology and Interface Engineering Series, 41, p.165-173 (2003).

The effect of boundary conditions on vibration based damage detection in FRP composite beams

[2]Magd ABDEL WAHAB, [1]Wei XU, [1]Andrew CROCOMBE, [1]O. ADEDIRAN

[1]Department of Mechanical, Medical and Aerospace Engineering,
University of Surrey,
[2]Department of Mechanical Construction and Production,
Faculty of Engineering, Ghent University

Abstract

This paper presents an experimental analysis to understand the limitations and significance of using vibration data to examine Vibration Based Damage Detection (VBDD) methods. The effects of boundary conditions on damage detection in FRP composite beams are considered. The approach used herein evaluates the resonance frequency shift as a function of the level of introduced damage. The results showed that the sensitivity of modal parameters were dependent on the boundary conditions, highlighted by the presence of resonance shift, change in mode shapes and damping ratios between an intact and damaged beam structure. Four different boundary conditions are implemented; namely simply supported (SS), fixed-fixed (FF), fixed-simply supported (FS), and fixed-free (FFR) boundary conditions. The results showed that effect of boundary conditions had significant importance on the sensitivity of damage detection. Out of all considered boundary conditions simply supported (SS) boundary conditions proved to be most sensitive to damage.

1. Introduction

A number of damage detection techniques are proposed in the literature to detect cracks and fault in a structure in order to decide the structure remaining life. Their uses and reliability have consequently become an important factor in the evaluation of the safety of any structure. Various engineers and scientists have devoted their time and efforts towards developing new, more reliable, efficient, and less tedious detection techniques.

In general damage detection technique can be classified into two broad categories a) the vibration based damage detection methods, defined as global

methods (including direct and indirect methods), because they do not give sufficiently accurate information about the extent of the damage, but they can alert about its presence and define its precise location [Change et al., 2003]. (b) The local methods based on visual inspections and experimental tests of acoustic or ultrasonic methods, magnetic field methods, radiograph, and eddy-current methods were previously discussed [Doherty, 1987]. The local methods require access to the portion of structure to be inspected.

Observation has shown that vibration-based identification technique to monitor structural integrity is sensitive to physical parameters [Farrar et al., 1998], [Salawu, 1997], [Landrein et al., 2001]. A change in physical parameters of a structure results in change of its modal parameters; therefore, change in natural frequencies, damping ratios, mode shape vectors or related measures, i.e. mode shape curvatures or identified flexibility matrix, may indicate damage development in the structure, and the structural health condition.

This paper presents an experimental verification to evaluate the effect of boundary conditions on damage detection in FRP beams. Since, it is difficult to distinguish between changes in modal parameters due to environment, damage or boundary conditions; it is worth investigating the effect of boundary conditions. The dynamic tests were carried on intact, fully bonded and partially bonded (damaged) beam, where the modal parameters were recorded for each case.

2. Experimental Investigation

FRP Composite beam description. The dynamic test was conducted using an intact, fully bonded and damaged *FRP* composite beam with different boundary conditions. The test beams were supplied by *Strongwell Company* and the manual (contain both mechanical and physical properties) provided by the same company was used as a reference during the course of this research [Strongwell Design Manual, 2002].

The three sets of beams mentioned above were used for this experimental investigation. Each set consisted of four beams. The first set had fixed-fixed boundary conditions at both ends, and the second set was simply supported, third had fixed-free supported, and the last had fixed-simply supported as shown in Figures 1. Each beam was made of *FRP* (Fibreglass Reinforced Polymer) beam of a cross-sectional area 0.03 m by 0.03 m with a length of 1 m. The mass of the beam was calculated as $812.3\,\text{gm}$. The FRP beam has the following properties: Young modulus is $1.7926 \times 10^{10}\,\text{N}/\text{m}^2$, density equals to $1827\text{Kg}/\text{m}^3$, and poison ratio is 0.3 [Strongwell Design Manual, 2002].

The dynamic behaviour of each beam was investigated in this study. The experimental procedure was carried out carefully to guarantee a high degree of accuracy.
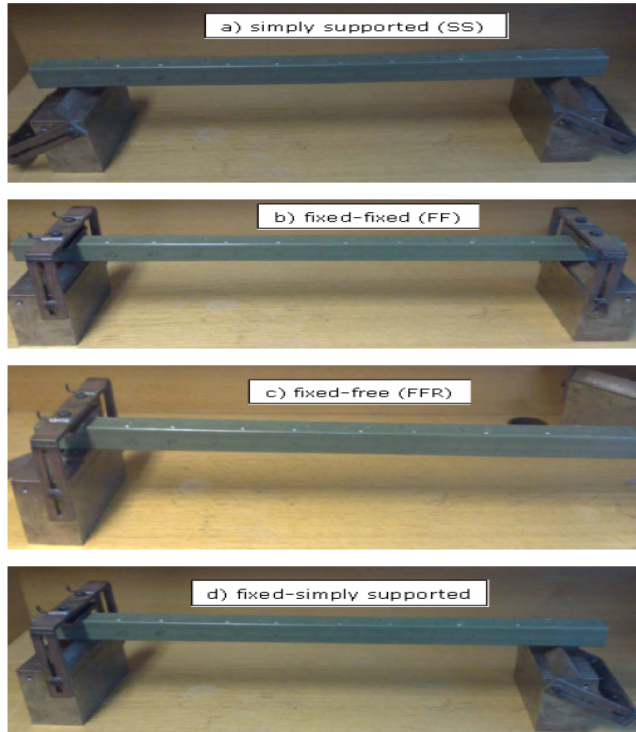
Figure 1. Experimental setup of boundary conditions

Damage Simulation with Adhesive Bonding. Most induced type of damage appears to be overload-crack damage and saw-cut damage. In this experimental work damage was simulated by bonding one side (out of four different sides) of the beam i.e. the beam with artificial crack at its mid-point. Several steps were taking to implement artificial damaged. The procedures and graphical views for artificial bonding are shown in figure 2.
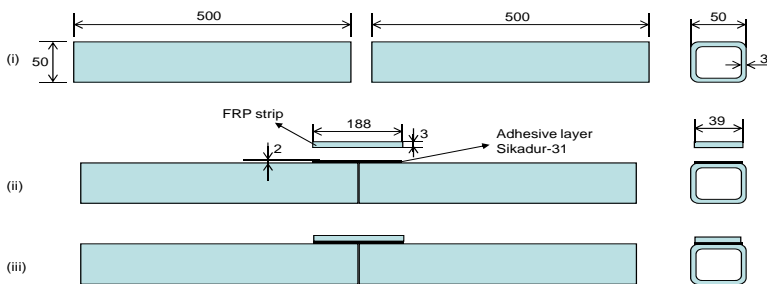

Figure 2: Bonding of test beams; (i) Two FRP beams before bonding (ii) bonding process (iii) partially bonded beams

Two-part thixotropic epoxy adhesives were used in this experiment. The epoxy adhesive has two parts, which are mixed together at the ratio of 3:1 for 3 minutes with mixing spindle until the material becomes smooth in consistency and has a uniform grey colour.

Fully bonded beam and damaged beam– In this case two sections of *FRP* composite beam are bonded together from all four sides of the beam using epoxy adhesive (Sikadur-31). While damaged beam, only one-side of the beam was bonded with FRP strip as shown in figure 3.
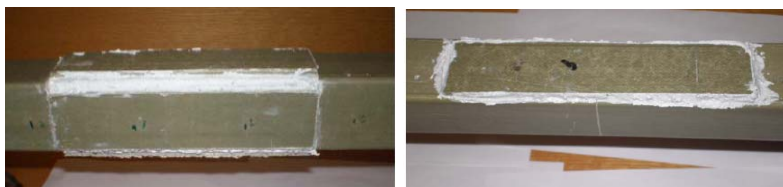

Figure 3. Fully-bonded and Partially-bonded beam specimen

Experimental Testing. To simulate the effect of boundary conditions on the dynamic behaviour of the beam, two rigid steel supports were designed. The steel support, with 0.25 m height, 0.12 m length and 0.09 m breadth. These rigid steel supports were used to simulate the different boundary conditions on the beam ends (steel frame for fixed boundary condition and steel triangular shape for simply supported). The two support sides have bolts and nuts at the screw thread area as indicated in figure 1. To implement the fixed boundary condition, specimens were mounted on the steel support clamped in two positions as shown in figure 1, through a torque wrench to achieve accurate torque. For the case of simply supported boundary condition, composite beam specimens were mounted on the steel supported with extra triangle shape steel without preventing rotation.

An impact hammer was used to excite the *FRP* composite beam. The clear length, i.e. the total length that remains after the beam attached to the steel support of the beam, is about $0.82\,\text{m}$ and is divided into 9 points. The distance between each point on the beam is equivalent to $1.025 \times 10^{-1}\,\text{m}$. Two different triaxial accelerometers were used during this experiment, one being used as a reference, while the other one as a moveable. Triaxial accelerometers are intended for simultaneous measurement of vibration in three perpendicular axes. Trixial accelerometer has average weight of $0.0367\,\text{kg}$. The connection cable pointed toward y (horizontal) & z (vertical) – directions of the signal analyzer to each accelerometer that is all response measurements were toward vertical direction of the beam. The moveable accelerometer positions were located at 1/8 intervals of the span starting from support of the composite beam.

For data acquisition the LDS-Dactron Phazer dynamic signal analyzer and the LDS-Dactron RT Pro [RT Pro Version 6.0, 2004] were used to record the dynamic response at 5000 Hz sampling frequency. All vibration data acquired

are imported to *SPICE* [Peeters and De Roeck, 1999] to process the acquired modal parameters such as frequencies, damping ratio and mode shapes.

3. Results

The results in terms of natural frequencies and damping ratios for intact and damage beam are presented in Table 1.

There was a clear indication of relative drop in natural frequency shift for damaged beams for each mode due to artificial damaged introduced as indicated in Table 1. It is clear from all indication that different boundary condition produced different changes in modal parameters which attribute an importance to damage indication.

Table 1. Comparison between Experimental Results of Intact and damaged beams for SS, FF, FFR and FS Boundary Conditions

Boundary Conditions		1st three modes [Hz]			Damping Ratio		
		Intact	Damaged	Diff %	Intact	Damaged	Changes
SS-	f1	144.63	20.36	85.74	3.7	4.1	9.7
	f2	534.45	525.87	1.6	3.7	4.7	21.28
	f3	1019.36	690.44	32.27	5.0	5.2	3.65
FF-	f1	308.26	232.68	24.52	3.1	3.7	8.8
	f2	765.75	680.56	11.13	4.4	4.5	2.22
	f3	1298.17	1230.01	5.25	4.7	5.9	20.55
FFR-	f1	53.004	19.98	62.30	1.9	2.3	15.79
	f2	315.00	127.35	59.57	2.3	3.3	30.30
	f3	784.68	609.46	22.33	2.6	3.9	33.33
FS-	f1	220.66	140.85	37.17	5.7	6.7	17.91
	f2	650.59	568.98	12.5	6.9	6.9	0
	f3	1301.83	1408.01	8.16	7.2	7.4	2.7

For example, the case of fixed-fixed boundary conditions – the natural frequencies for composite *FRP* beam decreased from 308.26 Hz for mode 1 to 232.68 Hz. For mode 3 it was seen a slight decreased in the natural frequency compared to mode 1. The relative decrease in natural frequency compared to the intact condition for the beam ranges 24.54% for mode 1 to 5.25% for mode 3. These are also the case for every other boundary condition investigated experimentally. There are changes in value of frequency response due to damage since natural frequencies are determined by the boundary conditions of a system. It was observed from the results that changes in boundary conditions will have effect on the structural damage scenarios examined.

The existing study has presented that changes in the modal parameters (damaged effect) may not be the same for each mode and each boundary conditions. For example, in the case of damping, FF boundary conditions, it can

be seen that for mode 1 the change is 8.8% and mode 2 is 2.22% but mode 3 demonstrated a bigger difference of 20.55%. The SS boundary condition at mode 3 dropped in percentage changes to 3.65%. The frequency shifts in the case of SS boundary conditions are also very significant from other boundary conditions, which seems that, the SS boundary more sensitive to damage out of all the boundary conditions. There is a reduction in percentage different in damping ratios at SS boundary condition for the case of mode 3 which can be considered to be less accurate result.

4. Conclusion

The effect of boundary conditions on vibration based damage detection in *FRP* composite beam is studied. The boundary conditions considered are simply supported, fixed-fixed, fixed-free and fixed-simply supported. Particular damage scenarios were applied to the beam model by bonding a side of the beam and leave the other parts unbonded to induce artificial damage. The dynamic identification tests were performed with the aim of using the modal parameters to assess damage in beam structure. The evaluation of the variation in the modal parameter due to the effect of boundary conditions was carried out. The results show that the influence of simply supported boundary conditions on measurements or vibration data have great impact on modal parameters. In other words the result from this work indicated that simply supported boundary is more sensitive to damage in comparison to other three boundary conditions: fixed-fixed, fixed-free and fixed-simply. Boundary condition effect is one of the factors of change in dynamic properties, therefore boundary condition effects should be considered, when using VBDD technique.

References

1. Chang, P.C., Flatau, A., and Liu, S.C. (2003): "Review Paper: Health Monitoring of Civil Infrastructure", Structural Health Monitoring, Vol. 2 (3), pp. 257-267.

2. Doebling, S.W., Farrar, C.R., and Cornwell, P.J. (1997) "A Computer Toolbox for Damage Identification Based on Changes in Vibration Characteristics," Structural Health Monitoring, Current Status and Perspectives, Stanford University, Palo Alto, California, pp. 241–254.

3. Doherty, J.E. (1987). "Nondestructive Evaluation," In: Handbook on Experimental Mechanics, Kobayashi, A.S. (ed.), Society for Experimental Mechanics, Inc., Chapter 12, Bethel, CT.

4. Farrar, C.R. and Doebling, S.W. (1998) "Damage Detection and Evaluation II Field Applications to Large Structures, Modal Analysis and Testing", Kluwer Academic Publishers, London, pp 345-378.

5. Landrein, P., Lorriot, T., and Guillaumat, L., (2001). "Influence of some test parameters in specimen loading determination methods instrumented Charpy impact tests". Eng. Fracture Mech., 68(15): 1631-1645.

6. Peeters, B., and De Roeck, G., (1999) "Reference-Based Stochastic Subspace Identification for Output-Only Modal Analysis". Mechanical Systems and Signal Processing, 13(6), pp. 855-878.

7. RT Pro Version 6.0 (2004) Release Extends LDS-Dactron Dynamic Signal Analyzer Capabilities.

8. Salawu, O.S. (1997). Detection of structural damage through changes in frequency: a review. Engineering structures, 19(9): 718-723.

9. Strongwell Corporation. Strongwell Design manual. Bristol, Virginia, US; 2002.

Three dimensional fourier analysis of the surface microtopography

[1]István BARÁNYI, [1]Gábor KALÁCSKA, [2]Árpád CZIFRA
[1]Institute for Mechanical Engineering Technology, Szent István University
[2]Institute of Machine Design and Safety Engineering, Óbuda University

Abstract

Tribological behaviour – friction, wear and lubrication – of machine elements highly depend on the operating state and also the original topography of working pair. Nowadays – beyond the parameter based technique – two dominant research trends can be observed in surface roughness characterisation. One is the technique when the local features of topographies are characterized based on the identification of asperities and scratches, while the other is the "global" surface characterisation method using complex mathematical tools.

   In our study surface roughness measurements were performed. The roughness and waviness of the surface microtopographies can be filtered and differentiated by three dimensional Fourier analysis.

   The aim of this study was to define the dominant and specific wavelengths of microtopographies in two main directions.

Keywords

Fourier, filtering method, roughness characterization, wavelength

1. Introduction

In the past decades researchers provided experts involved in surface microtopography research with a number of tools and methods to characterize the machined surface. At the same time, this knowledge is utilized only a small degree in the engineering practices [1]. Nowadays engineers use only a filtered data for the characterisation of the surface microtopography. The most applied filtering methods has prepared the roughness profile from the measured profile by traditional mathematical background. These methods – e.g. 2RC or Gauss filter - made by electronic or statistic models with transfer function depend on cut off wavelength [Varga et. al., 2011, Horváth 2008].

   In the present study Fourier analysis were performed to examine specific and dominant wavelength of the profiles of the measured microtopography.

Investigated topographies
The first pert of investigation was the turned and short blasted surfaces. The turning surface microtopography has been an orientation by feeding of the

manufacture. The other surface has no orientation. In all cases 1 by 1 mm surface topography was measured with 2 μm sampling in both directions. Measurements were performed in Mahr Perthometer Concept stylus instrument. Table 1. summarize the roughness parameters of the surfaces and Fig.1 shows the microtpographies:

Table 1. Roughness parameters of the investigated topographies

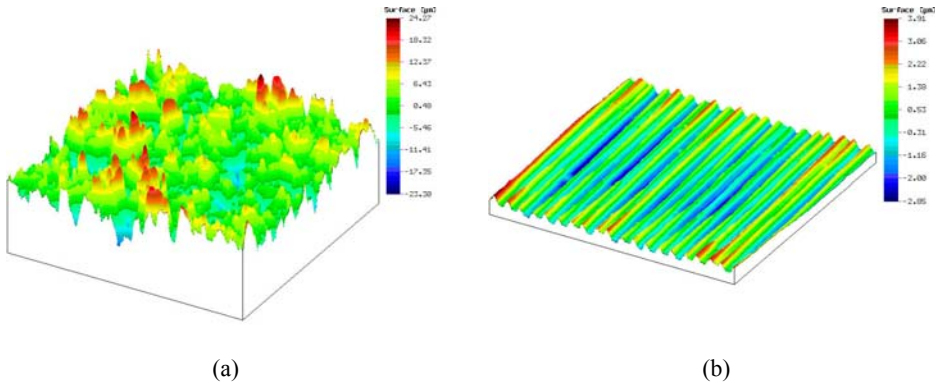| Machining technique	Sa	Sq	Sz
turning	0.98 μm	1.18 μm	6.75 μm
Short blasting	4.86 μm	6.18 μm	47.56 μm

(a)   (b)

Figure 1.a,b The short blasted and turned microtopography

Mathematical method of the characterisation of special wavelength

The wavelength based characterization method developed by Fourier transformation. The discrete transformation made as follows:

$$F(q_p) = \Delta x_i \sum_{i=1}^{M} z(x_i) e^{-j2\pi q_p x_i} \tag{1}$$

And the PSD amplitude made as follows (Persson et. al. 2005):

$$A(q_p) = \frac{F(q_p)F^*(q_p)}{M\Delta x} \tag{2}$$

There are two possibilities of showing results. One is to represent the amplitude of PSD in the function of wavelength. The other prevalent method is logarithmic scale frequency-PSD amplitude visualization. The practical gain of

the first method is that dominant wavelength components appear as a maximum point of the PSD curve. In the second method the height frequency range of the curve can be approximated by a line. The slope of the line is in correlation with the fractal dimension of surface. In the latter case, wavelengths smaller than the highest dominant wavelength plays a considerable role. PSD amplitude becomes constant – the self-affinity character of the profil disappears – in a lower wavelength range. The slope of fitted line to PSD curve has correlation with fractal dimension (Stout et. al.,1993).

Results

The (1) and (2) equation was accepted all of the measured profiles of the surface microtopography. The results of analysis is the short blasted case are summarised in Figure 2.a,b and the turning case are summarised in Figure 3.a,b.
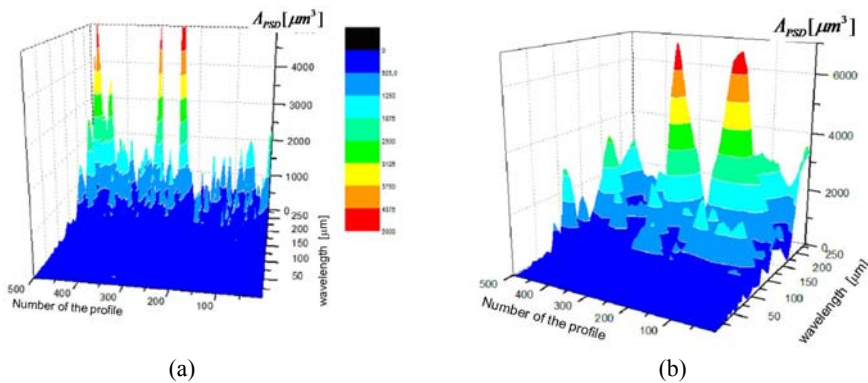

(a)   (b)

Figure 2. a,b The wavelength distribution in two direction

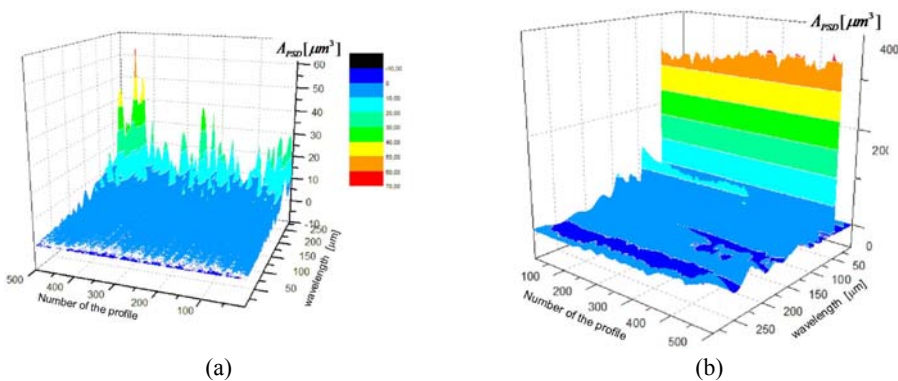(a)   (b)

Figure 3. The wavelength distribution a., in parallel on and b., in perpendicular of machining direction

As the Figure 1.a.,b. and Figure 2.a.,b. shows, the PSD amplitude is different the two perpendicular directions. In the case of surface microtopography with no direction the bigger PSD amplitude belongs to different wavelength in both of the direction of analysis (Barányi, 2009). The short blasted surface has not a characteristic main wavelength which determines a turnting wavelength of the filtering method. The usable filtering wavelength can lost some information for the roughness profile or the waviness profile.

In the case of orientated surfaces the PSD amplitude is different in the two main directions. In the perpendicular of machining direction the maximum of the PSD amplitude can be found in same wavelength and this value is equal with the feed of the turning (Fig. 4.). In the parallel direction the values of the Fig.3.a. diagram are smaller than the Fig 3.b. In this direction can be found main waviness for all of the profiles.
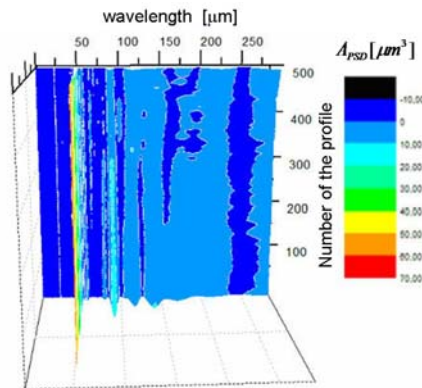

Figure 4. The wavelength distribution in perpendicular of machining direction

2. Conclusions

In the measurement practice the roughness measuring proposes only a few directive for the three dimension filtering methods. The most procedures apply traditional mathematical methods for filtering and these methods have a special characterisation. The Fourier method gives information for the waves of the profile and the researcher can decide the value of the cutting wavelength. With this model can be filtering the special parts of the microtopography. For this mathematical method researchers can be use the special characteristic of the Fourier based filtering.

Nomenclature

Sa	average roughness	μm
Sq	root mean square roughness	μm

Sz	max height of surface	μm
q_x	frequencies in x and y directions	kHz
$z(x_i)$	height coordinate located in x_i	μm
M	number of points in profile	--
Δx	sampling distances	μm

References

1. Barányi I, Czifra Á. (2009), Különböző megmunkálású felületek vizsgálata amplitúdó sűrűség spektrum (PSD) analízissel. GÉP 2009/10 XI. pp. 7-10.

2. Horváth S. (2005), A felületi hullámosság jelentősége, a hullámosság 3D-s értelmezése. GÉP 2005/9-10, p. 82-85, 2005

3. Horváth, S., Czifra, Á. (2009), Új módszerek a felületi érdesség és hullámosság vizsgálatában, OGÉT XVII. Nemzetközi Gépész Találkozó, Gyergyószentmiklós, pp. 169-173.

4. Persson BNJ, Albohr O, Trataglino U, Volokitin AI, Tosatti E. (2005), On the nature of surface roughness with application to contact mechanics, sealing, rubber friction and adhesion. J. Phys, Condens. Matter17:R1-R62

5. Stout KJ, Sullivan PJ, Dong WP, Mainsah E, Luo N, Mathia T, Zahouni H. (1993), The development of methods for characterisation of roughness in three dimensions. University of Birmingham Edgbuston

6. Varga Péter, Barányi István, Dr. Kalácska Gábor (2011), Felületi Érdesség mérésekor alkalmazott szűréstechnika gyakorlati kérdései, XVI. Fiatal Műszakiak Tudományos Ülésszaka, Kolozsvár, Románia, March 24.-25., pp. 365-368.

Theoretical and experimental analysis of rolling worm gears efficiency

Radu COTEȚIU, Adriana COTEȚIU

North University of Baia Mare, Romania

Abstract

Taking in account the lower values of classical wormgear efficiency, the study of wormgears with rolling elements is important. The paper presents theoretical and experimental results regarding the efficiency values in various functional conditions.

Keywords

special worm gears, rolling friction, efficiency

1. Introduction

Increasing the efficiency of worm gears has been a long time preoccupation of specialists in gears. Over time, innovations were found, such as the Buckingham-Ryfel solution, Litvin-Niemann solution or constructive solutions for ameliorating of the friction conditions.

One of these solutions is using rolling elements between active surfaces of the worm gear. It is possible to change sliding friction with rolling friction, which is more favorable.

This paper presents the experimental results obtained by the authors testing the efficiency of a worm gear with rolling elements.

2. Theoretical aspects of worm gear efficiency

The theoretical study of rolling and sliding worm gears was made taking in account the real and specific conditions in the experimental work (load, speed, dimensions range, materials and lubrication).

For the both of variants (sliding worm gear and rolling worm gear) we considered mineral grease RUL 100 Ca3 STAS 1608. For the rolling worm gear we had following dates:

- the balls' surface roughness was R_z 0.4μm,
- the worm's rolling way roughness - R_z 1.6μm,
- the wheel's rolling way roughness - R_z 1.6μm,
- the balls' diameter 9.525mm,

- the helix angle's variation is in the experimental determined range – 4°…6°,
- the contact angle between balls and rolling ways - 40°,
- the same active balls number,
- the rolling circle in the strangulation section - d_{01}=40mm,
- the wheel's rolling circle - d_{02}=96mm,
- elastic modulus of the rolling ways and balls - $E=2,3 \times 10^5 MPa$.

The calculus of efficiency was made with formula (1):

$$\eta = \frac{P_2}{P_1} = \frac{\left(\cos\gamma_0 - \dfrac{\mu}{\cos\alpha_n} \cdot \sin\gamma_0 \right) \cdot d_2}{\left(\sin\gamma_0 + \dfrac{\mu}{\cos\alpha_n} \cdot \cos\gamma_0 \right) \cdot d_1 i_{12}} \tag{1}$$

The theoretical calculus of the efficiency with (1) must take the friction coefficient for the real conditions in which the experimental work passed and contact type in the two situations: rolling contact and sliding contact. Calculus for these conditions was made pursuant to [7], [8], [9] in MathCAD.

The calculated efficiency for the rolling solution, for three revolutions, is presented in figure 1, in concordance with the experimental loaded range.

The friction coefficient's variation is presented in figure 2. We can observe that we have a continuous decreasing curve.

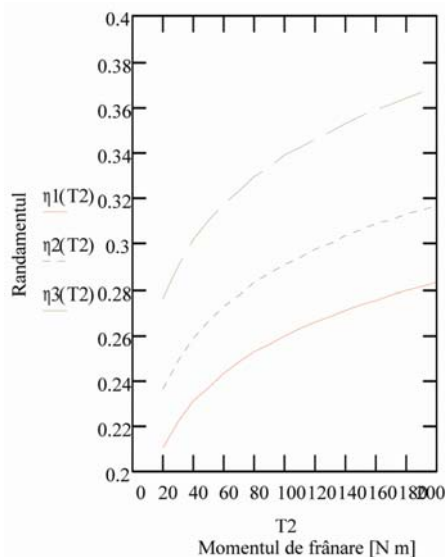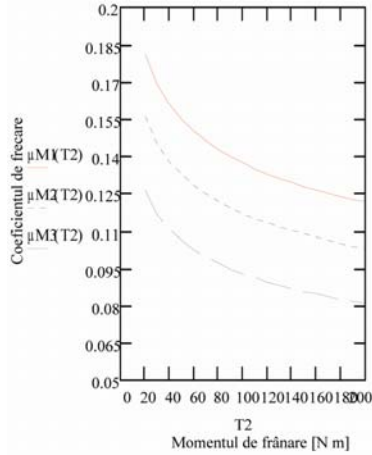## 3. Experimental results and conclusion

Figure 1.

Figure 2.

The experimental results are synthesized in figure 3. Figure 3b presents the variation of the rolling worm gear with load and the worm gear's revolution variation.

We can observe the correspondence between the experimental curve and the theoretical curves, which show efficiency variation for applied load domain. In the experimental case we also obtain the increasing of the efficiency value.

If we analyze figure 3a and figure 3b, it's evident that the efficiency values for rolling worm gear is greater. Also, it's possible to see that we obtained different variations in the efficiency curves for rolling and sliding gears.

(a)   (b)
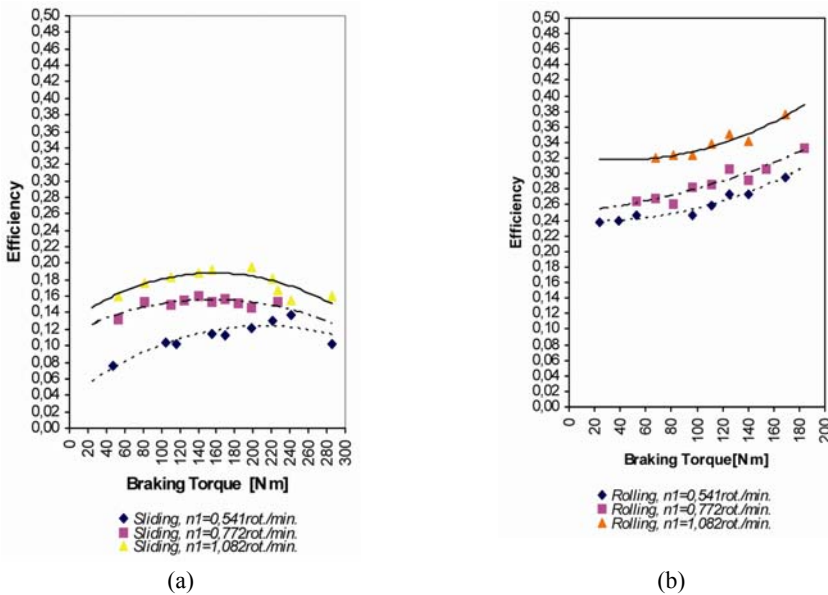
Figure 3.

If we compare figure 3 and figure 1, we have the confirmation of the obtained experimental curve's tendency. Both situations have the same tendency for efficiency increasing in correlation with entrance revolution. The tendency is explicable due to better lubrication conditions at greater rev.

The low values for efficiency are explicable by a little helix angle and low sliding speeds. For such values, we have some examples in [5], [6], [7]. Therewith we have a decrease in efficiency with the decreasing of revolution.

References

1. Buzdugan, Gh. Rezistenţa materialelor. Editura tehnică, Bucureşti, 1980.

2. Coteţiu, R. Teza de doctorat. Universitatea Tehnică din Cluj Napoca.1998

3. Chişiu, Al., ş. a Organe de maşini. Editura Didactică şi Pedagogică, 1980.

4. Gafiţanu, M., ş. a. Organe de maşini, vol. II, Editura Tehnică, Bucureşti, 1983.

5. Halteman, M., ş. a. Un model general pentru determinarea globală a momentelor de frecare în rulmenţii radiali - axiali cu bile. Construcţia de maşini nr. 10/ 1990.

6. Manea, Gh., ş. a. Organe de maşini, vol. II, Editura Tehnicã, Bucureşti, 1958.

7. Maros, D., ş.a. Csigahajtások. Műszaki Könyvkiadó, Budapest, 1970.

8. Maroş, D., ş. a. Angrenaje melcate. Editura Tehnică, Bucureşti, 1966.

9. Olaru, N. D. Tribologie. Elemente de bază asupra frecării, uzării şi ungerii. Universitatea Tehnică Gh. Asachi Iaşi, 1992.

10. Tudor, A., ş.a. Durabilitatea şi fiabilitatea sistemelor mecanice. Editura tehnică. Bucureşti, 1988.

11. Zak, P.S. Globoidnaia peredacia, Maşghiz. Moskva. 1962.